IEKP–KA/97–5

Observation of the B^* Dalitz Decay with the DELPHI Detector at the LEP Collider

Wulf Oberschulte gen. Beckmann

Institut für Experimentelle Kernphysik
Universität Karlsruhe (TH)
D–76128 Karlsruhe

E–mail: wulf@mail.cern.ch

Abstract

A first experimental observation of the second order electromagnetic decay of the B^* meson was done with the DELPHI data of the year 1994. The copious Z^0 production of the LEP–Collider and the decay $Z^0 \to b\bar{b}$ allow the study of B mesons. The B meson (J=0) has a hyperfine splitting to the B^* (J=1) of 46 MeV/c^2. Additionally to the usual decay $B^* \to B\gamma$ a second order decay in Quantum Electrodynamics is possible with a virtual photon in the final state $B^* \to Be^+e^-$. The extremely low energy electron and positron tracks are usually not reconstructed by the conventional track reconstruction methods. Using the DELPHI silicon microvertex detector of the year 1994 very low energy electron tracks can be reconstructed. Additionally the dE/dx in the silicon detector can be measured. Together with an inclusive B reconstruction method, the second order electromagnetic decay $B^* \to Be^+e^-$ has been observed for the first time. The inclusive cross section of the production is measured to be:

$$\frac{\sigma(B^* \to B\ e^+e^-)}{\sigma_{b-quark}} = (3.21 \pm 0.62(\text{stat.}) \pm 0.59(\text{syst.})) \times 10^{-3}.$$

The ratio of the production rate to the usual B^* decay $B^* \to B\gamma$ results in the following ratio :

$$\frac{\Gamma(B^* \to B\ e^+e^-)}{\Gamma(B^* \to B\gamma)} = (4.79 \pm 0.93(\text{stat.}) \pm 0.91(\text{syst.})) \times 10^{-3},$$

in agreement with a QED prediction of 4.7×10^{-3}.

Contents

List of Figures viii

List of Tables ix

1 Introduction 1

2 Production and Decay of the B* Meson 4

2.1 Bound Quark States 4

2.1.1 Static Quark Picture 4

2.1.2 Quantum Chromodynamics 6

2.1.3 $q\overline{q}$-Potential Approaches 8

2.1.4 Heavy Quark Effective Theory 9

2.2 B-meson Production on the Z^0 Resonance 11

2.2.1 Electroweak e^+e^- Annihilation 12

2.2.2 Perturbative QCD Phase 14

2.2.3 Fragmentation of Quarks 15

2.3 The B* Meson 18

2.3.1 Predictions for the B*–B Splitting 19

2.3.2 Decay of the B* 20

2.3.3 The π^0 Dalitz Decay 23

2.3.4 The B* Dalitz Decay 23

3 The Apparatus 27

3.1 The LEP Storage Ring 27

3.2 DELPHI Detector 30
3.3 DELPHI Track Chambers 32
3.3.1 Microvertex Detector (VD) 32
3.3.2 Further Track Chambers 35
3.4 Online System 39
3.5 Offline System 40

4 Vertex Detector Tracking **43**
4.1 Track Reconstruction in general 43
4.1.1 Track Definition 43
4.1.2 Usual Tracking Procedure 45
4.1.3 Offline Treatment of the Vertex Detector 46
4.2 Vertex Detector Tracks 48
4.2.1 Association of R-Φ Hits 50
4.2.2 Association of z-Hits 51
4.2.3 Properties of the VD tracks 54
4.2.4 Applications of VD Tracks 58
4.3 dE/dx Measurement with the Vertex Detector 60
4.3.1 Module Calibration 62
4.3.2 dE/dx Resolution 64

5 Reconstruction Tools **68**
5.1 Reconstruction of Dalitz Pairs 68
5.1.1 Simulation Test 71
5.2 Inclusive Reconstruction of B Mesons 78
5.2.1 b-Quark Tagging 78
5.2.2 Rapidity Algorithm 82
5.2.3 Energy Correction of the B Mesons 84

6 Analysis of the Decay $B^* \to Be^+e^-$ **87**

6.1 Event and Track Selection 87
6.2 B* Reconstruction 88
6.3 Signal Determination 89
6.4 Calculation of Efficiency 92
6.4.1 Calculation of the Cross Section 93
6.5 Results 94

7 Summary **96**

Bibliography **98**

Acknowledgements **101**

List of Figures

2.1 SU(4) 16–plets of mesons 6

2.2 Particle production in e^+e^-annihilation 11

2.3 cross section of u- and d-quarks to Z^0 13

2.4 Fragmentation of a colour string into hadrons. 15

2.5 Fragmentation functions for light and heavy quarks 17

2.6 Photon energy of B^* decay at LEP 21

2.7 Decay of B^* into on shell and virtual photon 24

2.8 Transition form factors and q^2 spectrum for B^* Dalitz decay 25

3.1 The pre-accelerator machines for the LEP ring. 28

3.2 The DELPHI detector open with one visible end cap. 31

3.3 Layout of vertex detector 34

3.4 Cross section of double sided detector 34

3.5 spatial resolution of the vertex detector 35

3.6 TPC geometry 36

3.7 dE/dx of TPC 37

3.8 offline data flow 41

4.1 Definition of perigee parameters 44

4.2 Vertex Detector $R\Phi$-z transformation 47

4.3 Event with missing tracks in the vertex detector 48

4.4 Vertex Detector in R-z plane 52

4.5 ΔZ_{ext} for VD tracks z-hit assoc. 53

4.6 Θ and ϕ distr. of VD tracks 55
4.7 Angular and energy resolution of VD tracks 56
4.8 VD tracks track parameters 57
4.9 invariant masses of kink candidates 59
4.10 Normalised Landau function 60
4.11 Geometry of path length correction 62
4.12 Module specific pulse height 63
4.13 Vertex Detector dE/dx 66
4.14 VD dE/dx resolution 67

5.1 dE/dx of code=–27 pairs 70
5.2 q^2 spectrum of –27 pairs 72
5.3 q^2 spectrum of –26 pairs 72
5.4 q^2 spectrum of –25 pairs 73
5.5 Parameter difference contributions for photon matching 75
5.6 Energy dependence of purities and efficiencies 75
5.7 Observation of π^0 Dalitz decay 77
5.8 Impact parameter of b-tagging. 79
5.9 Track significances 80
5.10 Event probabilities 81
5.11 Rapidity distributions 83
5.12 Event hemispheres 84
5.13 Energy correction of inclusive B 86
5.14 Angular resolution of inclusive B 86

6.1 Energy and mass distribution of inclusive B meson 88
6.2 Mass difference of B*–B 90
6.3 Dalitz pair energy spectrum 91
6.4 Signal simulation sample 93

List of Tables

2.1 Additive quantum numbers of the quarks. 5

2.2 $q\overline{q}$ quark model assignments 5

2.3 Meson masses and constituent quarks 9

2.4 partial widths of the Z^0 boson 13

2.5 Known b-hadrons from e^+e^-data 18

2.6 LEP B^* results in comparison 22

3.1 LEP machine parameter 29

4.1 VD tracks statistic z-hit assoc. 54

4.2 VD tracks statistic 58

4.3 dE/dx resolution 65

5.1 Cuts on Dalitz pairs 74

5.2 B-tagging efficiency 80

6.1 Signal model variation 92

6.2 The systematic contribution to the relative cross section. 95

1

Introduction

The main goals of elementary particle physics are the understanding of the simplest structure of matter and the forces acting between the basic constituents. We know that ordinary matter is built of atoms and the forces between atoms stem from electromagnetism. The challenging question arises in dimensions smaller than the nuclei of atoms. These nuclei consist of protons and neutrons. From our todays knowledge the constituents of proton and neutron are quarks. Further elementary particles are the leptons. Both quarks and leptons are spin 1/2 particles, also called fermions. The quarks carry only thirds of the elementary charge. Today the up (u), down (d), charm (c), strange (s), top (t) and bottom (b) quark are known. The leptons are electron (e^-), muon (μ^-) and tau (τ^-) together with the corresponding neutrino species (ν_e, ν_μ, ν_τ). The forces acting between these particles can be divided into the strong and electroweak interaction. The forces are transmitted by boson particles with integer spin. These are the gluons (g) for the strong and the photon γ, Z^0- and $W^\pm$–bosons for the electroweak interaction, following the Standard Model [1] of particle physics. While the quarks participate in all interactions, the leptons are effected only by the electroweak forces.

The quarks are known to exist in bound states only, forming hadrons. The hadrons built of three quarks (qqq) are called baryons, for example the proton or neutron. Bound states of quark and antiquark ($q\overline{q}$) are called mesons, e.g. the π meson. The static quark picture using these constituents can explain the existence of all established hadrons. Beside some candidates assumed to be bound states of gluons, called glueballs, every hadron can be interpreted as a $q\overline{q}$ or qqq ground state or an excitation of this.

This thesis deals with meson states of the b-quark. The b-quark was discovered 1977 by the group of L. Lederman (CFS Collaboration) at the Fermi National Accelerator Centre Chicago (USA). In the process $p + N \rightarrow \mu^+\mu^- + X$ the muon pair showed an excess in the invariant mass spectrum around 10 GeV/c^2. This resonance was interpreted as the decay of a $b\overline{b}$ bound state into $\mu^+\mu^-$. The meson was later called $\Upsilon(1S)$, since it was understood as a $N^{2S+1}L_J = 1^3S_1$ excitation of the ground state η_b with 1^1S_0. Beside the Υ further b-quark mesons have been seen. In 1983 it was confirmed by CESR (Cornell USA) and later at DORIS (Hamburg Germany) that the $\Upsilon(4S)$ decays into

$B\overline{B}$ mesons. The known B mesons are bound states of a b-quark and a $\bar{u}$-,$\bar{d}$- or $\bar{s}$-quark. As for atomic physics, there is also a hyperfine $J = 0, 1$ splitting for mesons, since a spin-spin interaction leads to different energy states. For the B meson with $J^P = 0^-$ the hyperfine excitation is the B^* meson with $J^P = 1^-$. The energy difference of 46 MeV between B and B^* is analogous to the 21 cm wavelength splitting in the spectrum of the hydrogen atom, caused by the interaction of the electron and nuclear spin. The B^* is known to decay as $B^* \to B\gamma$.

The copious production of Z^0 bosons at the LEP collider[1] allows further studies in this field. About 15% of the Z^0 bosons produced by e^+e^-collisions decay into $b\overline{b}$ pairs. The produced $b\overline{b}$ pairs hadronise to b-quark mesons and baryons, weakly decaying after $\sim$ 1.5ps into c-quark hadrons. The production of $J^P = 1^-$ B^* mesons was seen to be 0.67 per $b\overline{b}$ event and the decay $B^* \to B\gamma$ was measured by all four LEP experiments, ALEPH, DELPHI, L3, and OPAL.

In addition to the dominant decay of $B^* \to B\gamma$, a second order electromagnetic decay $B^* \to Be^+e^-$ is expected. Similar to the decay $\pi^0 \to \gamma e^+e^-$, first predicted by R. H. Dalitz [2], this decay is called B^* Dalitz decay. This thesis deals with the first experimental observation of this process. The decay into B γ takes place right after the production of the B^* meson at the primary vertex. The B meson decays later after an average distance of $\sim$ 1.6 mm, following the long lifetime of 1.5 ps and the boost of $\gamma \approx 3.6$. This signature of displaced tracks is used to enrich a sample of $b\overline{b}$ events.

Because of the small energy splitting of 46 MeV the photon has low momentum. Even in the LEP laboratory frame, where the B mesons get about 35 GeV/c momentum, the energy of the photon is below 800 MeV. The energies of electron and positron are much smaller, the average momentum is less than 300 MeV/c. Both are not well measured with the track chambers of the DELPHI detector. Because of their curvature in the magnetic field, these particles do not reach the usual track chambers and are confined to the vertex detector.

The DELPHI vertex detector in the configuration of the year 1994, allowed tracks to be reconstructed in three dimensions. Using a new algorithm, it was possible to reconstruct the low momentum tracks of electron and positron, from points in the vertex detector alone. The B meson four momentum was estimated from the momentum sum of the decay particles of the B meson. With this inclusive technique the mass difference distribution of $\Delta M = M(Be^+e^-) - M(B)$ was measured to look for the B^* Dalitz decay. The result can be compared with a precise prediction of Quantum Electrodynamics.

The static quark model, the understanding of mesons and the production of hadrons in e^+e^-collision is explained in chapter 2. This part also includes predictions of the hyperfine splitting and the decay rate for $B^* \to Be^+e^-$. In chapter 3 the experimental setup is introduced. The main emphasis is on the DELPHI detector and the subdetectors used. The special track finding procedure to reconstruct the low energy electron positron pair is described in chapter 4. This and the dE/dx measurement with the ver-

[1] Large Electron Positron Collider at CERN Geneva, Switzerland

tex detector are the tools necessary for the analysis presented later. The reconstruction of the final state B e^+e^-can be divided into the Dalitz photon reconstruction and the B meson reconstruction. Both parts are described in chapter 5. The analysis of the decay $B^* \to Be^+e^-$ is explained in chapter 6.

2

Production and Decay of the B* Meson

This chapter explains the definitions of a meson as a state built of two quarks. The static quark model and the binding forces between these quarks are briefly introduced. Next an approximation of the two quark problem in the limit of one heavy quark is described. Then the present understanding of the production of B mesons in e^+e^-annihilation is explained. Finally the B* meson and predictions for mass splitting of B* to B and the possible decay modes are discussed. The chapter ends with a prediction for the B* decay rate into the final state B e^+e^-.

2.1 Bound Quark States

Hadrons are bound states of two ($q\overline{q}$) or three (qqq) quarks. They are called mesons ($q\overline{q}$) and baryons (qqq) and can be assigned to the known flavours u, d, c, s, t and b of the static quark model. The multiplet structure of the B mesons ($b\bar{q}$ states) can be explained by the Heavy Quark Effective Theory (HQET), which is later used to give predictions for the B*–B mass splitting.

2.1.1 Static Quark Picture

The **static quark model** was developed by Gell-Mann and Ne'emen [3] in the 1960's to explain the multitude of hadrons known at that time. They divided the particles into octets and singlets. From the symmetry of these groups Gell-Mann and Zweig [4] derived the irreducible representations, the quarks, as the basic constituents of matter. This theory was experimentally confirmed when Taylor and Kendall [5] discovered the substructure of the proton in 1972, which can be explained by particles with electric charge $\pm$e/3 or $\pm$e2/3. At this time three quarks where used : up(u), down(d) and

Table 2.1: *Additive quantum numbers of the quarks.*

	u	d	c	s	t	b
Q electric charge	+2/3	-1/3	+2/3	-1/3	+2/3	-1/3
$\mathbf{I_3}$ isospin (3rd comp.)	+1/2	-1/2	0	0	0	0
S strangeness	0	0	0	-1	0	0
C charm	0	0	+1	0	0	0
B bottomness	0	0	0	0	0	-1
T topness	0	0	0	0	+1	0
b baryon number	+1/3	+1/3	+1/3	+1/3	+1/3	+1/3
Y Hypercharge $Y = b + S$	+1/3	+1/3	+1/3	-2/3	+1/3	+1/3

Table 2.2: *$q\overline{q}$ quark model assignments for some known mesons, η_b has not been observed so far, but the excited Υ states establish it existence.*

		$(d\bar{u}, u\bar{u}, d\bar{d})$	$(u\bar{u}, d\bar{d}, s\bar{s})$	$(c\bar{d}, c\bar{u})$	$b\bar{b}$	$(b\bar{u}, b\bar{d})$
$N^{2S+1}L_J$	J^{PC}	I=1	I=0	I=1/2	I=0	I=1/2
1^1S_0	0^{-+}	π^+, π^-, π^0	η, η'	D^+, D^0	(η_b)	$B^-, \bar{B}^0$
1^3S_1	1^{--}	ρ^+, ρ^-, ρ^0	ω, ϕ	D^{*+}, D^{*0}	$\Upsilon(1S)$	$B^{*-}, \bar{B}^{*0}$

strange(s). Today also the existence of charm(c), bottom(b) and top(t) is established. All quarks have spin 1/2 and baryon number 1/3. The additive quantum numbers isospin($\mathbf{I_3}$), strangeness(**S**), charm(**C**), bottomness(**B**) and topness(**T**) are shown in table 2.1. As a common convention the flavour has the same sign as the charge. This also means that a charged meson has the same sign as its charge: K^+ has strangeness +1, B^+ has bottomness +1, D_s^- has charm -1 and strangeness -1. The bound states of $q\overline{q}$ are called mesons, states of (qqq) are called baryons (the flavours of the quarks may be different). For a given angular momentum L of a $q\overline{q}$-state the parity is $P = (-1)^{L+1}$, the charge conjugation is $C = (-1)^{L+S}$ with the spin being $S = 0, 1$. A state of a quark and its own antiquark ($q\overline{q}$) is also an eigenstate of charge conjugation. From the $q\overline{q}$ $L = 0$ state the pseudoscalar $J^P = 0^-$ and vectors $J^P = 1^-$ can be formed with $J = L + S$. Assignments for some known mesons in this $q\overline{q}$ picture are shown in table 2.2.

Even in the absence of knowledge about the potential which binds the quarks to anti-quarks, the model is very predictive. All modes of $q\overline{q}$ excitation, rotations and vibrations correspond to discrete energy levels.

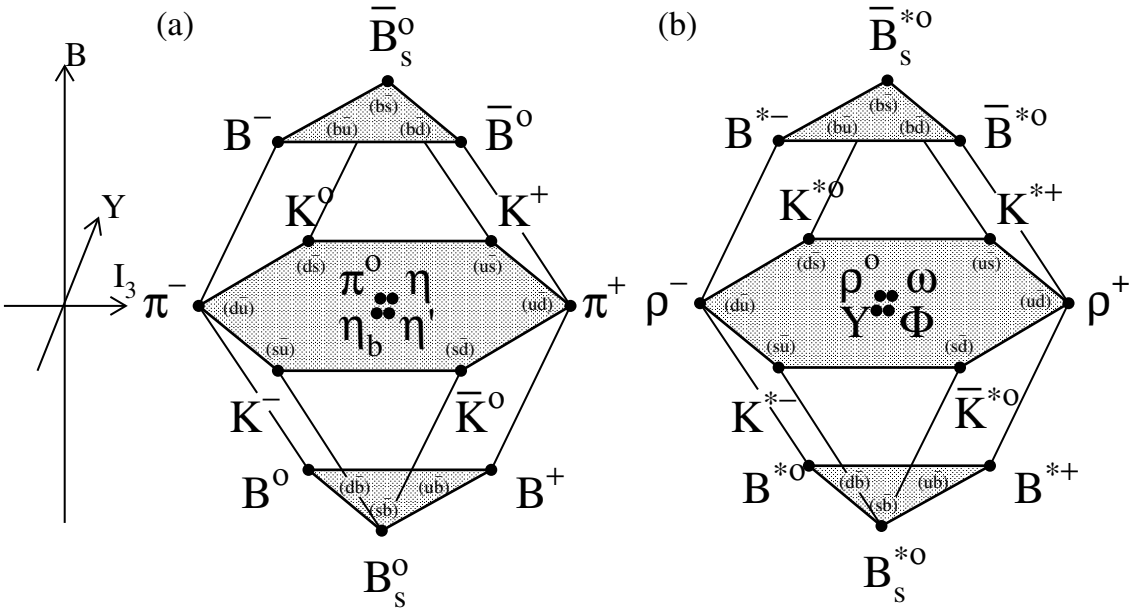

Figure 2.1: *SU(4) 16-plets for a) pseudoscalar and b) vector mesons. The axes of bottomness(***B***), isospin (***I***) and hypercharge (***Y***) are shown for orientation. States involving c quarks are not shown.*

Starting with u,d and s quarks $\mathbf{3} \otimes \mathbf{3} = \mathbf{8} \oplus \mathbf{1}$ possible states can be found (fig. 2.1 in the middle plane). States from this octet and singlet with the same IJ^{PC} and additive quantum numbers can mix. For example the $I = 0$ member of the ground state pseudoscalars mixes with the pseudoscalars singlet to the η and η'. The possible states with u,d,s and b-quarks are shown in fig. 2.1(a) the pseudoscalar solutions and the vector particles are shown in 2.1(b). Because the full multiplet of the SU(5) symmetry group requires four dimensions only the basic mesons (π and K) and the interesting bottom-mesons are shown.

2.1.2 Quantum Chromodynamics

The static quark picture has been able to explain the many different mesons as $q\overline{q}$ states, but cannot describe the binding forces between quarks. For this purpose a dynamical model for the strong interaction, **Quantum Chromodynamics** (QCD), is used. In addition to the quantum number shown, **colour** is needed for quarks, to save the Pauli exclusion principle. For example for the Δ^{++} baryon, where all 3 u-quarks (all with spin 1/2) exist in the same state, an additional quantum number had to be introduced, for the quarks to be different in some respect.

QCD is a $SU(3)_C$ gauge field theory which describes the interaction of coloured quarks and gluons. A quark has one of three basic colour charges, called red(r), green(g) and blue(b). The gluons derive from the 8 $SU(3)_C$ generators and transmit the force from

quark to quark:

$$\begin{array}{c} r\overline{g}, r\overline{b}, g\overline{r}, g\overline{b}, b\overline{r}, b\overline{g} \\ (r\overline{r} - g\overline{g})/\sqrt{2}, (r\overline{r} + g\overline{g} - 2b\overline{b})/\sqrt{6} \end{array} \tag{2.1}$$

All seen hadrons are colour singlet combinations of quarks, antiquarks and gluons, i.e. the total colour charge is zero. The three colour states form a Dirac spinor:

$$\psi_q^i = \begin{pmatrix} q_r \\ q_g \\ q_b \end{pmatrix} , \tag{2.2}$$

Invariance of the Lagrangian under local transformation in colour space is required:

$$\psi_q^i \rightarrow e^{i\alpha_a(x)\frac{\lambda_a}{2}}\psi_q^i; a = 1, ..., 8. \tag{2.3}$$

Where the rotation angle $\alpha(x)$ depends explicitly on x and λ_a are the eight Gell-Mann matrices, which are the generators of the $SU(3)_C$. After the introduction of the covariant derivative:

$$(D_\mu)_{ij} = \delta_{ij}\partial_\mu - ig_s \sum_a \frac{\lambda_{ij}^a}{2} A_\mu^a \tag{2.4}$$

and the necessary transformation of the gauge fields A_μ^a, $SU_C(3)$ invariance is achieved. The QCD Lagrangian reads:

$$\mathcal{L}_{QCD} = i\sum_q \bar{\psi}_q^i \gamma^\mu (D_\mu)_{ij} \psi_q^j - \frac{1}{4} F_{\mu\nu}^a F^{\mu\nu a} - \sum_q m_q \bar{\psi}_q^i \psi_{qi} , \tag{2.5}$$

with the field strength:

$$F_{\mu\nu}^a = \partial_\mu A_\nu^a - \partial_\nu A_\mu^a + g_s f_{abc} A_\mu^b A_\nu^c . \tag{2.6}$$

In eq. (2.5) the first term is the kinetic term of the quark fields ψ_q, the second term represents the self energy of the field and the quark masses are found in the last expression. From this Lagrangian three fundamental interactions can be derived:

- quark-gluon (from the kinetic term through the covariant derivative)
- triple gluon vertex (from the gluon field energy)
- quadro gluon vertex (from the gluon field energy)

After substituting expression (2.4) in equation (2.5), the coupling constant of the strong interactions $\alpha_s = \frac{g_s^2}{4\pi}$ is introduced. Similar to Quantum Electrodynamics the coupling constant of QCD depends on the specific momentum transfer Q^2. While the fine structure constant α_{QED} due to polarisation effects is decreasing with decreasing Q^2, the gluon self coupling causes an increase of α_s with decreasing Q^2. In first order perturbation theory this yields :

$$\alpha_s(Q^2) = \frac{4\pi}{(\frac{11}{3}N_C - \frac{2}{3}N_f)\ln(Q^2/\Lambda^2_{QCD})} \tag{2.7}$$

(N_C = number of colours = 3; N_f=number of quark flavours; Λ_{QCD} = scale parameter). For a momentum transfer of 1 GeV^2, which corresponds to a distance of 1 fm, the coupling is becoming too strong for usual perturbation calculations. Here QCD-lattice techniques or symmetry relations must be used. For large Q^2 the coupling constant α_s and therefore the binding forces between quarks become weaker. At large Q^2 quarks behave almost like free particles. This behaviour is called **asymptotic freedom** and characterises QCD at short distances, i.e. at high energies.

2.1.3 q$\overline{\text{q}}$-Potential Approaches

Because the coupling constant is too large for a perturbative solution, a potential ansatz is needed to compute the spectra of meson states. The ansatz assumes non relativistic conditions, and can be written in analogy with Quantum Electrodynamics, the quantised theory for the bound states of atomic physics:

$$H = \frac{\vec{p}^2}{2\mu} + V + H_{LS} + H_{SS} + H_T \ . \tag{2.8}$$

This is called the Breit-Fermi Hamilton function [6] for the reduced mass $\mu = (m_1 m_2)/(m_1 + m_2)$ in the non relativistic case. The kinetic expression is given in the first term and the specific potential can be expressed in V, while the other remaining terms describe the spin-orbit and spin-spin interactions. According to atomic physics the spin-spin interaction is assumed to be inversely proportional to the masses.

The direct development of a one gluon exchange between quark and antiquark, leads to a term in the potential proportional to α_s/r for small distances r [6]. This is similar to the Coulomb potential in Quantum Electrodynamics. Knowing that no coloured particles have been observed **(confinement)**, an increase of the potential for large distances can be assumed ($\sim ar$) motivating a potential term as:

$$V = -\frac{4}{3}\frac{\alpha_s}{r} + ar \ . \tag{2.9}$$

This treatment works well for bound states with two heavy quarks, since the assumption of non relativistic conditions is satisfied by the comparison of the meson mass and the

Table 2.3: *Meson masses and the masses of the constituent quarks in comparison. The ratio of binding energy to quark mass is much higher for light mesons than for heavy bound states.*

Meson	(quarks)	mass	$N^{2S+1}L_J$	quark masses
π^0	(u,d)	0.134 GeV/c^2	1^1S_0	$m_u = 0.300$ GeV/c^2
ρ^0	(u,d)	0.770 GeV/c^2	1^3S_1	$m_d = 0.300$ GeV/c^2
a_0	(u,d)	0.980 GeV/c^2	1^3P_0	
$\Upsilon(1S)$	(b)	9.46 GeV/c^2	1^3S_1	$m_b = 5$ GeV/c^2
$\chi_{b0}(1P)$	(b)	9.86 GeV/c^c	1^3P_0	

quark constituent masses (see table 2.3). The meaning of quark masses is not easy to treat in QCD. Because of confinement quarks are never expected to be isolated and have always been observed in bound states. The quark mass which fits in the potential ansatz is called '**constituent mass**'. In the Lagrangian of QCD (2.5) the '**current-mass**' of quarks is used and depends on the specific renormalisation scheme. The numerical values for constituent and current masses differ by orders of magnitude. The differences vanish if the heavy quarks c and b are treated. Bound states are not expected for the top quark, which has an extremely large mass $m_{top} = 175 \pm 9$GeV/c^2 [7]. Due to phase space, the top quark decays too rapidly to form bound states. If not mentioned otherwise, the quark masses in this thesis are the constituent masses.

For mesons containing one or two light quarks, the non–relativistic conditions are not fulfilled and the spin spin interaction cannot be neglected any more. Therefore no general potential for light mesons exists, because all models depend on specific free parameters which have to be fitted from experimental data.

2.1.4 Heavy Quark Effective Theory

For systems with one heavy quark where the limit $\Lambda_{QCD}/m_Q \to 0$ or $m_Q \to \infty$ is nearly reached, simplifications for their interactions can be made. Several studies in recent years, based on these assumptions [8],[9],[10], have led to a theory which is now commonly known as the **Heavy Quark Effective Theory** (HQET).

In a system with one extremely heavy particle, its dynamics can be kept constant compared to its light partner. Any new motion or energy level of the light partner will not change the situation of the heavy one. Following this picture a heavy quark in a bound state can be considered as a static source of colour which is stable, whatever the light quark is doing. Any change of the spin or radial state will be dominated by the light quark. The equations of QCD in the neighbourhood of such an isolated heavy quark are those of the light quark and the gluonic degrees of freedom are dominated

by the boundary condition of a static triplet source with the colour-electric field at the origin. This leads to the expectation that the meson and baryon excitation spectra built on any heavy quark will be nearly the same.

Since the spin also decouples in the heavy quark limit from the gluon field, all quarks look like scalar heavy quarks to the light partners. When flavour and spin of the heavy quark are irrelevant, the static heavy quark symmetry would lead to a $SU(2N_h)$, with N_h the number of heavy quarks. At the spectroscopic level this additional symmetry means that each spectral level built on a heavy quark will be degenerate.

The characteristics of HQET can be summarized in two pictures:

1. A system with **heavy flavour symmetry** is analogous to the chemistry of two isotopes with different numbers of neutrons. The electronic structure is equal, since they still have the same nuclear charge.

2. The meaning of **heavy spin symmetry** in this picture is an atom with degeneracy of the hyperfine levels. The resulting hyperfine splitting can be ignored, since the nuclear magnetic moments are small compared to the energy levels of the field interaction.

With a heavy quark of minimal velocity v the Feynman rules can be simplified and result in the above mentioned simplifications of flavour and spin symmetry. The results are briefly introduced in the following. The heavy quark momentum can be written as:

$$p_Q = m_Q v + k \ , \tag{2.10}$$

where v is the four velocity, $v^2 = 1$ and k is called the 'residual momentum'. If k is neglected compared to m_Q, one obtains for the propagator:

$$\frac{i(\gamma_\mu p^\mu + m_Q)}{(p_Q^2 - m_Q^2 + i\epsilon)} \ . \tag{2.11}$$

In the limit $m_Q \to \infty$ even a simpler expression can be obtained:

$$\frac{i}{v \cdot k + i\epsilon} \ , \tag{2.12}$$

which is independent of the quark mass. Also the former gluon quark interaction vertex: $-ig_s T^A \gamma_\mu$ is reduced to:

$$-ig_s T^A v_\mu \tag{2.13}$$

and is not dependent on the spin any more. In this derivation several simplifications have been applied which are described in [8]. Also the Lagrangian of QCD (2.5) becomes

different and can be expanded in powers of $\mathcal{O}(m_Q^{-1})$ [8][11]:

$$\mathcal{L} = \bar{h}^{(Q)} iv D h^{(Q)} + \frac{1}{2m_Q}\bar{h}^{(Q)}(iD)^2 h^{(Q)} - \tag{2.14}$$
$$a_2(\mu)\frac{1}{4m_Q}\bar{h}^{(Q)} g_s \sigma^{\mu\nu} G^A_{\mu\nu} T^A h^{(Q)} + \mathcal{O}(m_Q^{-2}) \ ,$$

where $h^{(Q)}$ is the heavy quark wave function, D is the covariant derivative, $G^A_{\mu\nu}$ is the gluon field and T^A the colour index matrix. The second term in equation (2.14) is the kinetic energy of the heavy quark with respect to the light degrees of freedom and the third term is the energy splitting from the interaction of the heavy quark chromomagnetic moment with the magnetic field produced by the light degrees of freedom. The renormalization factor can be written in leading order as:

$$a_2(\mu) = \left[\frac{\alpha_s(m_Q)}{\alpha_s(\mu)}\right]^{9/(33-2N_f)} \ . \tag{2.15}$$

2.2 B-meson Production on the Z^0 Resonance

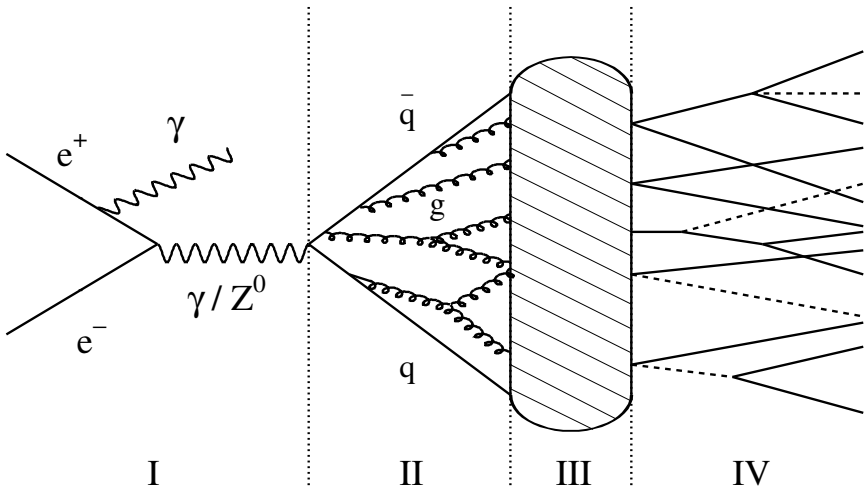

Figure 2.2: *Particle production in e^+e^- annihilation. The process is divided into four phases according to the theoretical understanding: The production (I) of the $q\bar{q}$ pair, the perturbative QCD phase of gluon emission (II), the fragmentation of coloured partons to colourless hadrons (III) and the decays of hadrons (IV).*

The abstract picture of fig. 2.2 represents B meson production in an e^+e^-annihilation. In the first phase the process is described well by the electroweak standard model [1]. The e^+e^-pair annihilates to a virtual γ or Z^0 resonance, which produces a primary $q\bar{q}$

pair. An initial bremsstrahlung-photon might smear the centre of mass energy. In the second phase the quark and antiquark radiate gluons, which again may radiate and so on. Then the coloured partons (quarks and gluons) fragment to colourless hadrons. Because the coupling constant becomes too large at low energy for perturbation theory, this transition cannot be calculated in the picture of perturbative QCD. Phenomenological models like 'string' or 'cluster' fragmentation are used to give predictions. In phase four the unstable hadrons decay into particles which can be observed by the experimental apparatus.

2.2.1 Electroweak e^+e^-Annihilation

The production cross section for massless quarks on the Born level is described by the formula:

$$\begin{aligned}\sigma(e^+e^- \to \mathrm{q\overline{q}}) &= N_C \frac{4\pi\alpha^2}{3s} \cdot Q_e^2 Q_f^2 \\ &+ \frac{12\pi\Gamma_{e^+e^-}\Gamma_{q\bar{q}}}{M_Z^2} \cdot \frac{s}{(s-M_Z^2)^2 + M_Z^2\Gamma_Z^2} \\ &+ \frac{2N_C\alpha^2\pi}{3} \cdot \frac{Q_e Q_q V_e V_q}{\sin^2\theta_w \cos^2\theta_w} \cdot \frac{(s-M_Z^2)}{(s-M_Z^2)^2 + M_Z^2\Gamma_Z^2} \cdot\end{aligned} \tag{2.16}$$

$\Gamma_{e^+e^-}$and $\Gamma_{q\bar{q}}$ are the partial decay widths of the Z^0-boson from the initial $e^+e^-$and the final $\mathrm{q\overline{q}}$ pair, $V_f = I_3 - 2Q_f \sin^2\theta_w$ and $A_f = I_3$ are the vector and axial coupling constants. The cross section decreases with increasing energy but gives a huge resonance when the centre of mass energy is near the Z^0-mass $\sqrt{s} \approx 91.2$ GeV, as can be seen in fig. 2.3. In expression (2.16) three parts representing the nature of the production process are included. First the photon exchange term, which decreases with increasing energy, secondly the Z^0-exchange and finally the interference of Z^0 and the photon. In the region of the Z^0 mass the whole expression is dominated by the Z^0 exchange term, while the interference and photon production can be neglected. The partial decay widths of the Z^0-boson to $\mathrm{f\bar{f}}$ are given by the following expression:

$$\Gamma(\mathrm{Z^0} \to \mathrm{f\bar{f}}) = N_c \frac{G_F M_Z^3}{6\sqrt{2}\pi} \beta \left(\frac{3-\beta^2}{2} V_f^2 + \beta^2 A_f^2\right) , \tag{2.17}$$

where $\beta = \sqrt{1 - \frac{4m_f^2}{M_Z^2}}$ is the velocity of the fermion. Table 2.4 shows the computed values for the partial decay widths. The total width of the Z^0-boson, which is given by adding all partial widths, is about 2.5 GeV. The hadronic width is defined by:

$$\Gamma_{had} = \Gamma_{u\overline{u}} + \Gamma_{d\overline{d}} + \Gamma_{c\overline{c}} + \Gamma_{s\overline{s}} + \Gamma_{b\overline{b}} .$$

To get an impression of the relative fraction of the partial widths to the total and

Table 2.4: *The partial widths of the* Z^0 *boson decays to all possible fermions at LEP energies. The quarks are sorted in up- and down-type.*

fermion	$\Gamma(Z^0 \to f\bar{f})$	$\Gamma(Z^0 \to f\bar{f})/\Gamma_{had}$	$\Gamma(Z^0 \to f\bar{f})/\Gamma_{tot}$
u,c	0.288 GeV	17%	12%
d,s,b	0.370 GeV	22%	15%
ν_e, ν_μ, ν_τ	0.166 GeV	-	7%
$e^\pm, \mu^\pm, \tau^\pm$	0.084 GeV	-	3.5%

hadronic widths, the ratios of $\Gamma_{f\bar{f}}/\Gamma_{tot}$ and $\Gamma_{f\bar{f}}/\Gamma_{had}$ are shown in table 2.4. According to the different coupling of u-type and d-type quarks to the Z^0, 22% of all hadronic Z^0 decays go into $b\bar{b}$-pairs. The up and down-type cross sections are compared in fig. 2.3.

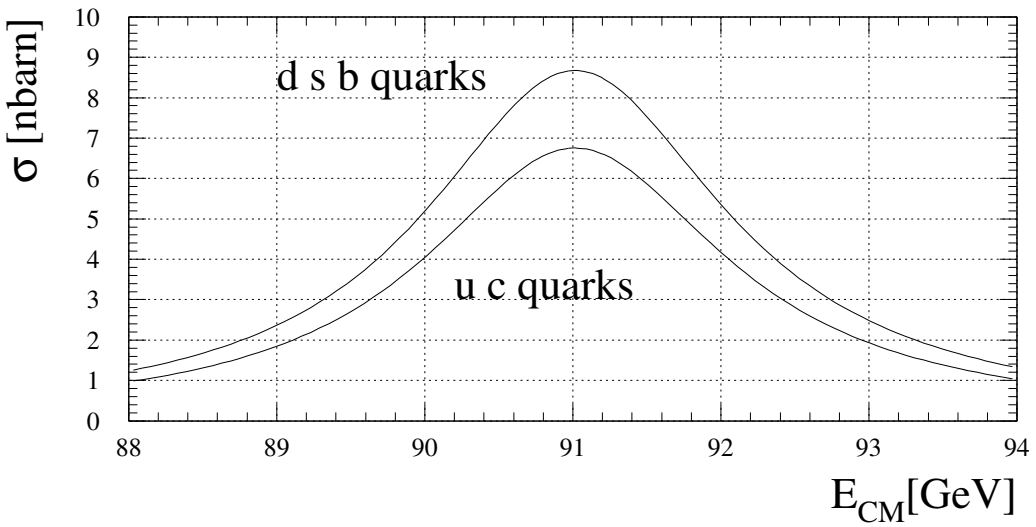

Figure 2.3: *The different cross sections of up and down type quarks are shown in nbarn, calculated from eq.(2.16) at the Born level. The up-type cross section has to be multiplied by two (u and c) and the down-type by a factor of three (d, s and b). The sum of both gives the total hadronic cross section.*

The b-quarks produced from the Z^0 resonance are expected to have a longitudinal polarisation, given by [12]:

$$P_L^b = \frac{2V_bA_b\beta(1+\cos^2\theta) + 2r_E(V_b^2 + A_b^2\beta^2)\cos\theta}{(V_b^2 + A_b^2)\beta^2(1+\cos\theta) + 2V_b^2(1-\beta^2) + 4r_EV_bA_b\beta\cos\theta} \ , \tag{2.18}$$

where $r_E = (4\sin^2\theta_w - 1)/(8\sin^4\theta_w - 4\sin^2\theta_w + 1)$, $\beta^2 = 1 - 4m_b^2/M_Z^2$ and θ the scattering angle in the centre of mass sytem relative to e^- axis. This value is expected

to be:

$$\langle P \rangle = -0.94 \ ,$$

with very little angular dependence. Whether this polarisation can be measured depends on the subsequent processes, since it is not known if the b-quark polarisation is transferred to the b-hadrons.

2.2.2 Perturbative QCD Phase

Two major approaches of perturbative QCD have been developed, for the second phase which describes the radiation of gluons from the produced $q\overline{q}$ pair. In the **matrix element** method Feynman diagrams are calculated up to a certain order. Within this calculation all kinematics and the full helicity and interference structure is taken into account. For example the cross section in first order QCD for the process ($e^+e^- \to q\overline{q}g$) can be written as:

$$\frac{1}{\sigma_0}\frac{d\sigma}{dx_1 dx_2} = \frac{\alpha_s}{\pi} C_F \frac{x_1^2 + x_2^2}{(1-x_1)(1-x_2)} \ , \tag{2.19}$$

where σ_0 is the total $q\overline{q}$ cross section of eq. (2.16) and $C_F = 4/3$ the colour factor of QCD. The variables $x_1 = 2E_q/E_{CM}, x_2 = 2E_q/E_{CM}$ are the energy fractions of the participating quarks and gluons. The obvious divergences from infrared or collinear gluon radiation ($x_1 \to 1$ or $x_2 \to 1$) cancel if all propagator and vertex corrections are taken into account. In second order QCD, the processes $e^+e^- \to q\overline{q}$ gg and $e^+e^- \to q\overline{q}q'\overline{q}'$ with four partons in the final state are also possible. Using this model two, three and four jet structures can be well described. Since only calculations up to $\mathcal{O}(\alpha_s^2)$ exist, the approach can describe final states with up to four partons. More detailed substructure of the measured jets cannot be created with this model.

A better prediction is given by the **parton shower** models. Here a shower of gluon emission and other splittings is derived within the framework of the Leading Logarithm Approximation (LLA). Only those terms which have the same power of α_s as the divergent logarithmic terms are used in the perturbative expansion. The basic branchings $q \to qg, g \to q\bar{q}$ and $g \to gg$ are used iteratively in a cascade to develop the shower evolution. For these splittings the probability $\mathcal{P}$ of the branching $a \to bc$ for a given momentum fraction z is :

$$\frac{\mathcal{P}_{a\to bc}}{dt} = \int dz \frac{\alpha_s(Q^2)}{2\pi} P_{a\to bc}(z) \ , \tag{2.20}$$

with $t = \ln(Q^2/\Lambda^2)$ and the $P_{a\to bc}(z)$ being the Altarelli–Parisi [13] splitting functions. The variable z specifies the sharing of four-momentum between the daughter b taking fraction z and c taking $1-z$ of the primary parton a. With this technique the parton shower model is able to produce multigluon final states, while the matrix element is

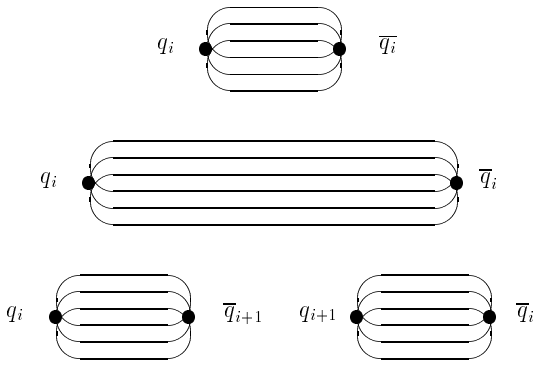

Figure 2.4: *Fragmentation of a colour string into hadrons.*

only able to make four partons in the final state. Since the angular distributions in the parton shower are put in by hand to first order, the angular distributions are uncertain compared to the matrix element method.

2.2.3 Fragmentation of Quarks

The development of quarks and gluons into a bunch of hadrons is generally known as fragmentation. In QCD this process can only be described with phenomenological models. Although these models only follow simple physical ideas of what may happen in this phase, the experimental results have confirmed these models in many aspects. They have led to a better understanding, but the final best model is still missing. None of the models describe all details observed in multihadronic final states. One of the most favoured models is the Lund string fragmentation [14] which follows an abstract picture. The main ideas are best illustrated for the production of a back to back $q\overline{q}$ pair. As the quarks move apart a colour flux tube is formed between their colour charges. The easiest way is to use a one dimensional string for this tube. According to hadron mass spectroscopy the amount of stored energy in the string with increases linearly with the distance by $\kappa \approx 1\text{GeV/fm}$. After the potential energy in the string is above the energy for the creation of a new $q\overline{q}$ pair, the string can break as shown in fig. 2.4. The flavour of the quarks depend on the mass and can be expressed by the probability of:

$$P \sim \exp(-\pi \frac{m^2 + p_T^2}{\kappa}) \; . \tag{2.21}$$

This probability implies the suppression of heavy quark production in the ratio of u : d : s : c : b with $1 : 1 : 0.3 : 10^{-11} : 10^{-100}$. This means that no heavy flavours like c or b are expected from string fragmentation. This procedure is repeated until the remaining energy is below the energy needed for the lightest $q\overline{q}$ pair. The observed hadrons, i.e. bound states of $(q\overline{q})$ and (qqq), are distributed around the primary $q\overline{q}$ momenta. Every

produced hadron carries a fraction of the initial quark energy:

$$z = \frac{(E + p_L)_{hadron}}{(E + p_L)_q} \ . \tag{2.22}$$

This reduces the available energy for every new $q\overline{q}$ creation to $(1 - z_i)$. The distribution of the transferred energy is described by the longitudinal fragmentation function. From comparison with measured momentum spectra two fragmentation functions have been established for different types of quarks: for light flavours u,d and s the Lund symmetric function is used [15]

$$f(z) \sim \frac{1}{z}(1 - z)^a e^{-\frac{bm_T^2}{z}} \quad , \tag{2.23}$$

while the heavy flavours c and b are better described by the Peterson-Zerwas ansatz [16]:

$$f(z) \sim \frac{1}{z[1 - 1/z - \epsilon_Q/(1 - z)]^2} \ . \tag{2.24}$$

Here a, b and $\epsilon_{c,b}$ are free parameters to be determined from measured momentum spectra. It is obvious that the momentum of the heavy quarks are less influenced by the fragmentation due to their greater inertia of their higher masses. Both functions are shown in fig. 2.5. The value $m_T^2 = m^2 + p_T^2$ is given by the transverse momentum distribution of the created hadrons, which can be described by a Gaussian distribution

$$f(p_T) = \frac{1}{\sigma_q \sqrt{2\pi}} e^{-\frac{1}{2}p_T^2 \sigma_q^2} \quad , \tag{2.25}$$

where σ_q is the variance of the resulting meson momentum transverse to the direction of the quark. It is determined by comparison to measured transverse momentum spectra.

If additionally gluons are introduced to the $q\overline{q}$ pair, the string becomes a bit more complicated. Because the gluons carry charge and anti-charge of different colours they attach two string pieces. The situation with hard gluons leads to the so called 'string effect' [17]. The mechanism of string breaking and $q\overline{q}$ production works as in the $q\overline{q}$ back to back case.

b-Quark Fragmentation

Figure 2.5 and eq.(2.24) demonstrate the expectation of a hard fragmentation of the b-quark. In fact the hadrons formed with beauty have an average momentum of about 70% of the beam energy, corresponding to 34 GeV for Z^0 decays (see [18][19]). Since

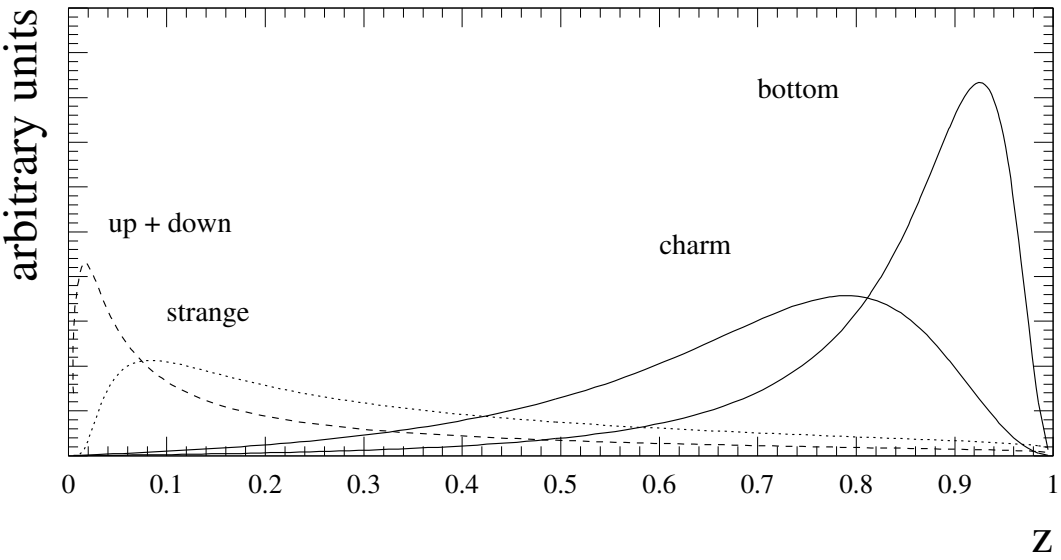

Figure 2.5: *Longitudinal fragmentation functions of heavy and light quarks. For the light quarks the Lund symmetric function with a=0.18 and b=0.23 was chosen. The heavy quarks are described by the Peterson Zerwas function with* $\epsilon_b = 0.006$ *and* $\epsilon_c = 0.06$*. For the transverse mass of the light flavours the masses of* π *and K have been used.*

fragmentation forms the hadrons, the b-flavoured hadrons are only related to each other by their bottomness (b and $\overline{\text{b}}$). All other quantum numbers might differ, since they are not produced in phase as on a $\Upsilon(4S)$-resonance where a $\text{b}\overline{\text{b}}$-meson decays into two b-flavoured mesons and further hadrons cannot be kinematically produced at that energy. At LEP nearly all possible b-hadrons can be produced since the available energy is much higher than the m_b threshold. Hadrons with two b-quarks or $b\overline{c}$ mesons are strongly suppressed according the probability of (2.21). The available energy can lead to excited B-meson and baryon states which decay right after their production, due to the short lifetimes of strong interactions. A summary of observed b-hadrons in e^+e^--annihilations is given in table 2.5.

From the high momentum and energy the B mesons produced in Z^0 decays are boosted and their observable decay length is enlarged. The Lorentz transformation of $x' = (\vec{x}', ct')$ with :

$$\begin{pmatrix} ct' \\ \vec{x}' \end{pmatrix} = \begin{pmatrix} \gamma & \gamma\beta \\ \gamma\beta & \gamma \end{pmatrix} \begin{pmatrix} ct \\ \vec{x} \end{pmatrix}, \tag{2.26}$$

leads to a decay length $(\Delta t \cdot \beta c)$ of $l_B = \beta\gamma c\tau_B$. The b quarks have at LEP a velocity of $\beta \approx 0.96$ and a resulting $\gamma \approx 3.57$. Together with a lifetime of $\tau_B \approx 1.5$ ps this results in the boosted decay length:

$$\langle l_B \rangle = \langle \beta\gamma c\tau_B \rangle = 1.6 \text{ mm} .$$

Table 2.5: *Known b-hadrons from [20], which have been observed in e^+e^- experiments. Masses and flavour compositions are shown.*

b-hadron	mass	constituents
$B^{\pm}$	5.279 GeV/c^2	bu
B^0	5.279 GeV/c^2	bd
B^0_s	5.370 GeV/c^2	bs
B^*	5.324 GeV/c^2	bu bd
B^*_s	5.416 GeV/c^2	bs
B^{**}	5.700 GeV/c^2	bu bd
B^{**}_s	5.853 GeV/c^2	bs
Λ^0_b	5.640 GeV/c^2	udb
$\Xi^{0,\pm}_b$	–	usb,dsb

2.3 The B* Meson

For a meson made of a heavy quark and a light quark, the heavy quark's role is similar to that of the nucleon and the light quark's role to that of the electron in atomic physics. Hyperfine splitting in atomic systems is due to the interaction of the nuclear magnetic moment with the magnetic moment of the electron. Similarly in the B meson this splitting occurs because of the orientation of the b quark spin. In the Dirac notation the possible meson states M (B and B*) with their third spin component S^z and the third spin components of heavy and light quark S^z_Q and s^z_l are :

$$\begin{aligned} |M, S^z\rangle &= |S^z_Q, s^z_l\rangle \\ |\mathrm{B}^*, +1\rangle &= |+1/2, +1/2\rangle \\ |\mathrm{B}^*, 0\rangle &= \tfrac{1}{\sqrt{2}}(|+1/2, -1/2\rangle + |-1/2, +1/2\rangle) \\ |\mathrm{B}^*, -1\rangle &= |-1/2, -1/2\rangle \\ |\mathrm{B}, 0\rangle &= \tfrac{1}{\sqrt{2}}(|+1/2, -1/2\rangle - |-1/2, +1/2\rangle) \end{aligned} \tag{2.27}$$

The B* meson is a vector particle and has three possible spin orientations while the B meson is a pseudoscalar or spin singlet. Based on simple spin counting, one would expect a production ratio of primary B* mesons to B to be 3:1. The results of LEP measurements in this respect will be presented later on.

2.3.1 Predictions for the B*–B Splitting

The hyperfine splitting can be approximated as being independent of flavour and spatial wave function. Taking the energy difference of a $J = 1$ to a $J = 0$ state to be inversely proportional to the heavy quark mass, one can derive an estimate from the D*–D splitting. Since in both mesons the light partner will be in a similar situation, this approach is reasonable. One gets:

$$\Delta M(\mathrm{B}^* - \mathrm{B}) = \frac{m_c}{m_b}\Delta M(\mathrm{D}^* - \mathrm{D}) \ . \tag{2.28}$$

Using the measured D and D* masses the splitting is expected to be:

$$\Delta M(\mathrm{B}^* - \mathrm{B}) = (42 \pm 6)\mathrm{MeV}/c^2 \ , \tag{2.29}$$

(with the values $m_{D^\pm} = 1870$ MeV/c^2, $m_{D^{\pm *}} = 2010$ MeV/c^2, $m_c = 1.5 \pm 0.2$ GeV/c^2 and $m_b = 5 \pm 0.3$ GeV/c^2. The error contains the uncertainties from the quark masses added in quadrature.)

The hyperfine splitting can be calculated in the HQET [8]. Based on equation (2.14) for a hadronic state $|H^{(Q)}\rangle$ normalised to unity one can define the dimensionless matrix elements $K_Q(H^{(Q)})$ and $G_Q(H^{(Q)})$:

$$K_Q(H^{(Q)}) = \frac{1}{m_Q^2}\langle H^{(Q)}|\frac{1}{2}\bar{h}^{(Q)}D^2 h_v^{(Q)}|H^{(Q)}\rangle \tag{2.30}$$

$$G_Q(H^{(Q)}) = \frac{a_2}{m_Q^2}\langle H^{(Q)}|\frac{1}{4}\bar{h}^{(Q)}g_s\sigma^{\mu\nu}G^A_{\mu\nu}T^A h_v^{(Q)}|H^{(Q)}\rangle \ , \tag{2.31}$$

which take the mass terms in (2.14) into account. The matrix elements in (2.30) have been evaluated in the $m_Q \to \infty$ limit, the m_Q behaviour is expressed in the coefficients $1/m_Q^2$ and a_2/m_Q^2. Up to terms of order $(\Lambda_{QCD}/m_Q)^2$ the masses of the mesons P and P*, which differ only the in hyperfine interaction, can be expressed as :

$$\begin{aligned} M(\mathrm{P}) &= m_Q + \bar{\Lambda}(\mathrm{P}) + m_Q K_Q(\mathrm{P}) + m_Q G_Q(\mathrm{P}) \\ M(\mathrm{P}^*) &= m_Q + \bar{\Lambda}(\mathrm{P}^*) + m_Q K_Q(\mathrm{P}^*) - \frac{1}{3}m_Q G_Q(\mathrm{P}^*) \ . \end{aligned} \tag{2.32}$$

In this expression the parameter $\bar{\Lambda}(\mathrm{P})$ is the positive contribution to the heavy meson mass that is independent of m_Q and comes from the part of the QCD Hamiltonian for the light quark. For the mass difference from the hyperfine splitting in the B meson one gets:

$$M(\mathrm{B}^*) - M(\mathrm{B}) = -\frac{4}{3}m_b G(\mathrm{B}) \ . \tag{2.33}$$

An equivalent expression can be written for the hyperfine splitting of the D/D* system. Since the function $G(\mathrm{P})$ is independent of the mass of the heavy quark, the $G(\mathrm{B})$ expression can be substituted with the D/D* mass difference and for the B system

$$M(\mathrm{B}^*) - M(\mathrm{B}) = \left(\frac{m_c}{m_b}\right)\left[\frac{\alpha_s(m_b)}{\alpha_s(m_c)}\right]^{9/25}(M(\mathrm{D}^*) - M(\mathrm{D}))\ , \tag{2.34}$$

can be derived. Taking the values $m_{D^\pm} = 1870$ MeV/c^2, $m_{D^{\pm *}} = 2010$ MeV/c^2, $m_c = 1.5 \pm 0.2$ GeV/c^2 and $m_b = 5 \pm 0.3$ GeV/c^2 together with $\alpha_s(m_b) = 0.2 \pm 0.02$ and $\alpha_s(m_c) = 0.3 \pm 0.03$ gives a splitting of

$$\Delta M(\mathrm{B}^* - \mathrm{B})_{HQET} = (36.3 \pm 5.7)\ \mathrm{MeV/c^2}, \tag{2.35}$$

with all uncertainties for the inputs added quadratically. The result is close to the measured value and shows that HQET can lead to predictions which are in agreement with experimental results at the level of two standard deviations.

2.3.2 Decay of the B*

These results (2.29) and (2.35) show that the transition energy of B* to B is too low for any hadronic decay. Therefore an electromagnetic decay by photon emission will dominate. The transition of a $J^{PC} = 1^{--}$ state to 0^{-+} restricts the parity of the photon emission $P_i = P_f \cdot P_\gamma$ to be $P_\gamma = 1$. The parity of a photon emission with an angular momentum J can be odd or even which is called:

$$\begin{aligned} \text{electric radiation E}J &: P_\gamma = (-1)^J \\ \text{magnetic radiation M}J &: P_\gamma = -(-1)^J\ . \end{aligned} \tag{2.36}$$

For the case of $J = 1$ and $P_\gamma = 1$ a M1 photon emission is expected. The first observation of B mesons used e^+e^-machines with centre of mass energy slightly above the $\Upsilon(4S)$ resonance [21][22][23]. A low energy photon of $\approx 50\mathrm{MeV}/c^2$ was seen together in events with a $\mathrm{B\bar{B}}$ pair. The B mesons were produced nearly at rest so that the photon energy gave the mass splitting directly. In e^+e^-annihilations at LEP the situation of the produced B mesons is very different. As explained in section 2.2.3 the B mesons have a mean velocity of $\beta \approx 0.96$ and get the energy distribution from the fragmentation function. The B* meson receives a significant boost, since the B meson takes a large fraction of the beam energy (see fig. 2.5). Additionally the emission angle relative to the B momentum has to be taken into account. The kinematical limit for a maximum B energy of 45 GeV, a photon energy of 46 MeV and a B* mass of 5.3 GeV/c^2, following the Lorentz transformations in eq.(2.26), would be 800 MeV. The photon energy spectrum of a Jetset74 [15] simulation is shown in fig. 2.6.

All photon energies are below 800 MeV. Photons in this kinematical region are difficult to detect, since a lot of material will cause conversions of these photons and the energy resolution of most calorimeters is not good enough to separate such photons from background. Only the L3 collaboration detected a signal of direct measured photons in $b\overline{b}$-events which was in agreement with a B* production [24]. The L3 detector is equipped with a calorimeter built of bismuth germanate (BGO) crystals, giving a resolution of 5% for the energy of the photons of interest. The absolute value of B momentum was set constant to 37 GeV/c and the direction measured with jet and muon momentum.

Another method for detecting the low energy photons is the reconstruction of converted photons. From the material in front of the main tracking chambers (see detector description in chapter 2 for the DELPHI experiment) it is possible that a low energy photon converts. The resulting e^+e^-pair is seen as two curved tracks in the tracking detectors with a zero opening angle originating from a common vertex inside the detector material. Using this method an energy resolution of 1% for the photons was reached, and the B momentum was estimated with an inclusive algorithm described later in chapter 5. The spitting was measured from the mass difference of the B and B* four-momentum [25]. Similar analyses have been performed by ALEPH [26] and OPAL [27]. The measured mass splittings are listed in table(2.6).

The primary b-quarks are expected to be polarised due to the specific V and A couplings of the Z^0, see section 2.2.1. It depends on the subsequent decay chain whether this information is conserved. The electromagnetic decay B* $\rightarrow$ Bγ is followed by the

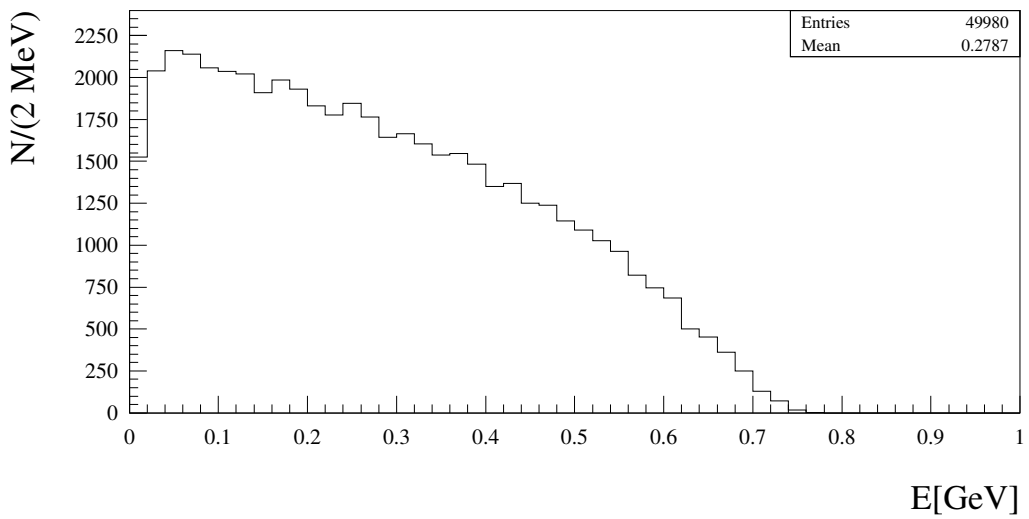

Figure 2.6: *The photon energy of the B* decay in the LEP laboratory frame. From the boost the energy goes up but is strictly below 800 MeV. The spectrum presents the pure theoretical expectation, no requirements concerning the geometry or quality have been made.*

Table 2.6: *LEP B* results in comparison. The mass splitting was computed from LEP data and from the PDG96 [20] value. All averages are weighted means.*

	Experiment	Measurement
$\Delta M(\mathrm{B}^* - \mathrm{B})[MeV/c^2]$	L3 [24]	46.3 ± 1.9
	DELPHI [25]	$45.5 \pm 0.3 \pm 0.8$
	ALEPH [26]	$45.3 \pm 0.4 \pm 0.9$
	OPAL [27]	$46.2 \pm 0.3 \pm 0.8$
	LEP average	45.5 ± 0.5
	PDG96	45.7 ± 0.4
$N_{B*}/(N_{B^*} + N_B)$ production rate	L3 [24]	$0.76 \pm 0.08 \pm 0.06$
	L3 update [28]	$0.76 \pm 0.04 \pm 0.06$
	DELPHI [25]	$0.72 \pm 0.03 \pm 0.06$
	ALEPH [26]	$0.77 \pm 0.03 \pm 0.07$
	OPAL [27]	$0.75 \pm 0.02 \pm 0.09$
	LEP average	0.75 ± 0.04
$\sigma(\mathrm{B}^*)/\sigma(b - quarks)$ production rate	L3 [24]	0.69 ± 0.09
	L3 update [28]	0.67 ± 0.06
	DELPHI [25]	0.65 ± 0.06
	ALEPH [26]	0.68 ± 0.08
	OPAL [27]	0.65 ± 0.09
	LEP average	0.67 ± 0.03

weak decay of the B meson. Since parity is conserved in electromagnetic decays a B* polarisation can only be measured from the knowledge of the photon polarisation. The final spin zero B meson carries no polarisation information.

Following a simple spin counting argument one would expect in e^+e^-collisions a production ratio of B* to B mesons of 3:1. Since the mass difference of less than 50 MeV can be neglected compared to the B meson mass, no phase space effects are expected. This assumes that the hadronisation process, from which the mesons emerge, does not selectively fill the different helicity states of the B* meson. From the preceding analyses [24], [25], [26] and [27] it was found that the naive expectation of 3:1 for this ratio is confirmed. The weighted mean of these measurements is $N_{\mathrm{B}^*}/(N_{\mathrm{B}^*} + N_{\mathrm{B}}) = 0.75 \pm 0.04$. A secon order electromagnetic decay of mesons as well the decay into an on-shell photon is possible. The photon can be emitted off shell with a q^2 value greater than zero and decay into an e^+e^-pair. As an example the π^0 decay is discussed below.

2.3.3 The π^0 Dalitz Decay

The π^0 can decay like $\pi^0 \to \gamma e^+e^-$, as first predicted by R. H. Dalitz [2] and observed by J. J. Lord et al. and R. A. Daniel et al. [29]. The effective mass spectrum can be expressed as [30]:

$$\frac{\mathrm{d}\Gamma(\pi^0 \to \gamma e^+e^-)}{\mathrm{d}q^2 \cdot \Gamma(\pi^0 \to \gamma\gamma)} = \frac{2\alpha}{3\pi}\left[1 - \frac{4m_e^2}{q^2}\right]^{1/2}\left[1 + \frac{2m_e^2}{q^2}\right]\frac{1}{q^2}\left[1 - \frac{q^2}{m_{\pi^0}^2}\right]^3 F_{\pi^0}^2(q^2). \quad (2.37)$$

Here $F_{\pi^0}(q^2)$ is the ratio of transition form factors for the transition $\pi^0 - \gamma$, which describes the hadronic corrections. The final computation gives a result of $\approx 1\%$. Further computations with Quantum Electrodynamics lead to the result [31]:

$$\Gamma(\pi^0 \to \gamma e^+e^-)/\Gamma(\pi^0 \to \gamma\gamma) = 1.196 \times 10^{-2}.$$

Today's experimental world average of the π^0 Dalitz decay is [20], (e.g. [32]):

$$\frac{\Gamma(\pi^0 \to \gamma e^+e^-)}{\Gamma(\pi^0 \to \gamma\gamma)} = (1.213 \pm 0.033) \times 10^{-2} \ . \quad (2.38)$$

2.3.4 The B* Dalitz Decay

Analogous to the π^0 meson the B* meson can decay into B e^+e^-. The photon could with a small probability be emitted off shell with a finite q^2 value and decay into an e^+e^-pair, as shown in fig. 2.7. This internal conversion decay is governed by the amplitude [30] :

$$\mathcal{M} = 4\pi\alpha i[f_{B^*B}(q^2)\varepsilon^{\alpha\beta\gamma\delta}p_\alpha q_\beta \epsilon_\gamma] \cdot \frac{1}{q^2} \cdot [\bar{u}\gamma_\delta u] \ , \quad (2.39)$$

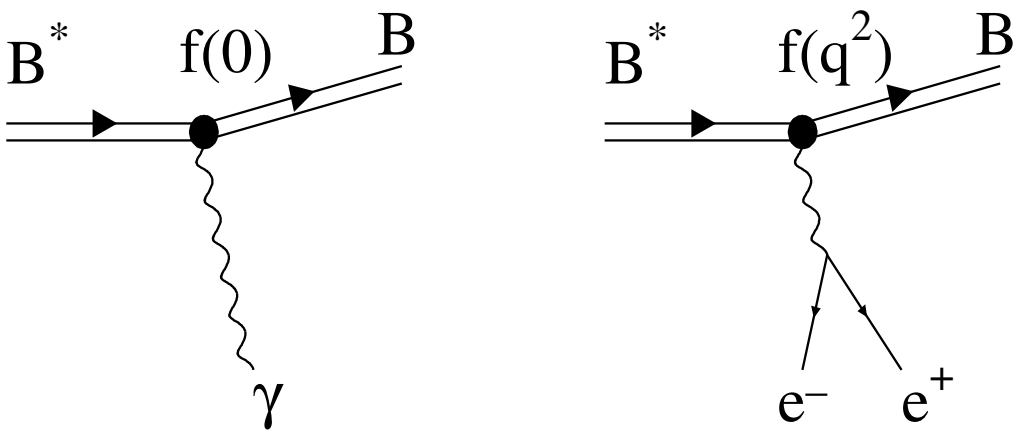

Figure 2.7: *Decay of the B^* into photon and the internal conversion decay. The form factors $f(0)$ and $f(q^2)$ describe the hadron photon coupling.*

with p_α and q_β being the four-momenta of the B and the virtual photon in the B* centre–of–mass system, ϵ_γ the B* polarisation vector, u and $\bar{u}$ the electron and positron's spinors, $1/q^2$ the virtual photon propagator and $f_{B^*B}(q^2)$ the B*–B transition form factor. The effective mass spectrum derived from this amplitude is:

$$\begin{aligned}\frac{\mathrm{d}\Gamma(B^* \to Be^+e^-)}{\mathrm{d}q^2 \cdot \Gamma(B^* \to B\gamma)} &= \frac{\alpha}{3\pi}\left[1-\frac{4m_e^2}{q^2}\right]^{1/2}\left[1+\frac{2m_e^2}{q^2}\right]\frac{1}{q^2} \\ &\cdot\left[\left(1+\frac{q^2}{m_{B^*}^2-m_B^2}\right)^2-\frac{4m_{B^*}^2q^2}{(m_{B^*}^2-m_B^2)^2}\right]^{3/2} F_{B^*B}^2(q^2)\ .\end{aligned} \tag{2.40}$$

$F_{B^*B}(q^2) = f_{B^*B}(q^2)/f_{B^*B}(0)$ is the normalised transition form factor with $F_{B^*B}(0) = 1$, describing hadronic corrections. Taking the mass of the B meson as zero leads to half of the expression for the π^0 Dalitz decay (2.37). This difference is simply caused by the two possibilities in the choice of the photon for a π^0 decay compared to the B* decay. The function used for the form factor depends on particular dynamical models. A typical ansatz is linear :

$$F(q^2) = 1 + 1/6 \cdot \langle r_{B^*B}^2\rangle q^2, \tag{2.41}$$

where $\langle r_{B^*B}^2\rangle$ is interpreted as mean square size of the interaction region. As can be found in [33], a value of :

$$\langle r_{B^*B}\rangle = 0.6 \text{ fm} \tag{2.42}$$

is reasonable for a meson. Another model uses the pole form :

$$F(q^2) = \frac{1}{1-q^2/\Lambda^2}\ . \tag{2.43}$$

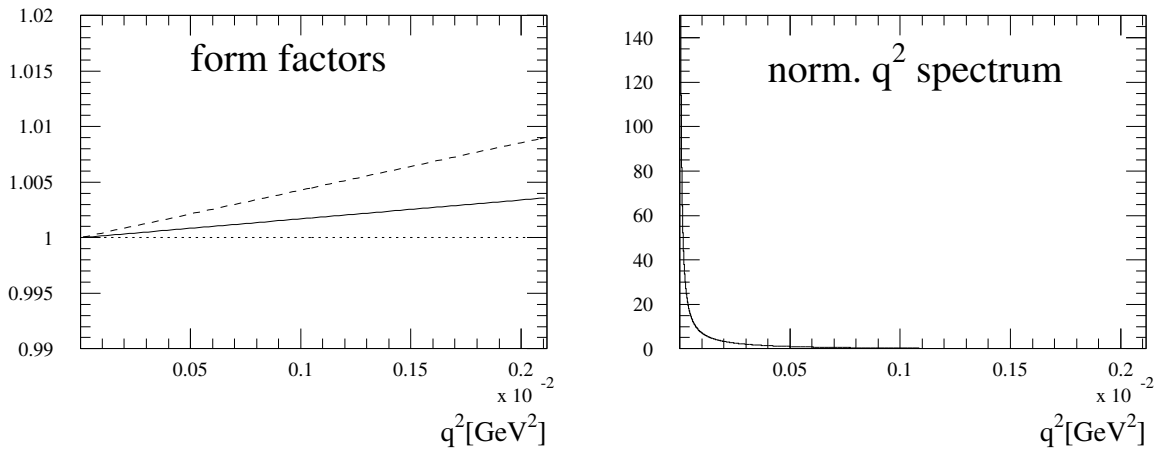

Figure 2.8: *The transition form factors for the B* Dalitz decay are shown on the left plot. The solid line illustrates the values for the ρ-VDM, the broken line the finite size model with $\langle r \rangle$=1fm, the dotted line for Υ-VDM. On the right the normalised q^2 spectrum of eq.(2.40) is presented using the ρ-VDM.*

In the Vector Meson Dominance model the pole mass Λ is related to virtual vector meson masses (m_ρ, m_ω etc.), depending on the flavour wave function of initial and final mesons (see [33]). For the transition B*–B a resonance of Υ could be possible, but more suppressed, compared to lighter mesons. All approaches should not differ too much since the maximum q-value of the B*–B splitting is quite low. In fact only a maximum deviation of 10^{-2} from unity is observed in this q^2 region, see fig. 2.8. The integral is clearly dominated from the decrease in the first part of the spectrum eq.(2.40). The integration boundaries are:

$$2m_e \leq q \leq \Delta m(\mathrm{B}^* - \mathrm{B}) \; . \tag{2.44}$$

Using $m_B = 5278.9 \pm 1.8$ MeV/c^2 [20] and $\Delta m(\mathrm{B}^* - \mathrm{B}) = 45.7 \pm 0.4$ MeV/c^2 from table 2.6 the integration of formula (2.40) gives:

$$\frac{\Gamma(\mathrm{B}^* \to \mathrm{B}e^+e^-)}{\Gamma(\mathrm{B}^* \to \mathrm{B}\gamma)} = (4.657 \pm 0.013) \times 10^{-3} \tag{2.45}$$

in point-like QED, i.e. a constant transition form factor equal to 1.
Other models give:

finite size model		
with $\langle r_{B^*B} \rangle = 1$ fm	:	$(4.659 \pm 0.013) \times 10^{-3}$
ρ–VDM, $m_\rho = 0.767\mathrm{GeV}/c^2$	:	$(4.658 \pm 0.013) \times 10^{-3}$
Υ–VDM, $m_\Upsilon = 9.460\mathrm{GeV}/c^2$	:	$(4.656 \pm 0.013) \times 10^{-3}$

As a consequence of the small available q^2 range in the B* decay, different values for $\langle r^2 \rangle$ or Λ^2 have only a very minor effect on the q^2 spectrum and the integrated branching ratio. The error is dominated by the experimental uncertainty on the B*–B mass difference. Thus there is a very precise theoretical prediction to test with the B* Dalitz decays.

3

The Apparatus

The experimental environment of the LEP ring for the e^+e^-annihilations is briefly introduced. To understand the track reconstruction the DELPHI detector, including the necessary subdetectors is described. Next the principles of the online and offline system, including the data processing, are explained.

3.1 The LEP Storage Ring

The e^+e^-collisions take place at the Large Electron Positron storage ring (LEP) of the European Laboratory for Particle Physics (CERN) [1] in Geneva, Switzerland. The storage ring has a circumference of 26.7 km and is 56–174 m under ground in the French region Pay de Gex and the Swiss canton Geneva. The ring contains the accelerating and focusing devices of the electron positron beam system and the four LEP experiments: ALEPH, DELPHI, OPAL and L3. For accelerating purposes there are several high frequency cavities installed, which allow an energy transfer of 400MV per revolution. Inside of these cavities an electromagnetic wave is built, which runs synchronous to the particle bunches. Dipole magnets are used int the ring to bend the beams. In bending the electrons and positrons loose energy due to synchrotron radiation. This loss is proportional to the fourth power of the beam energy [34]:

$$\Delta E = \frac{e^2}{3\varepsilon_0 (m_0 c^2)^4} \frac{E^4}{R} \ , \tag{3.1}$$

written in well known dimensions this reads:

$$\Delta E[keV] = 88.5 \frac{E^4[GeV^4]}{R[m]} \ . \tag{3.2}$$

[1] 'Conseil Europeen pour la Recherche Nucleaire' was the former french name

This formula gives an energy loss of 121 MeV for a beam energy of 45 GeV. Quadropoles, sextopoles and correction magnets are used to focus the beam. Since electron and positron have the same mass, but opposite charge, they run in opposite directions in the same beam pipe. To control the collisions of the opposite bunches electrostatic separators are used. They work with a transverse electric field of 2.5 MV/m. These separators can also be used to optimise the collision points, if the orbits of the beams do not match well enough. Before entering the ring the particle bunches are accelerated in other pre-accelerators as shown in fig. 3.1.

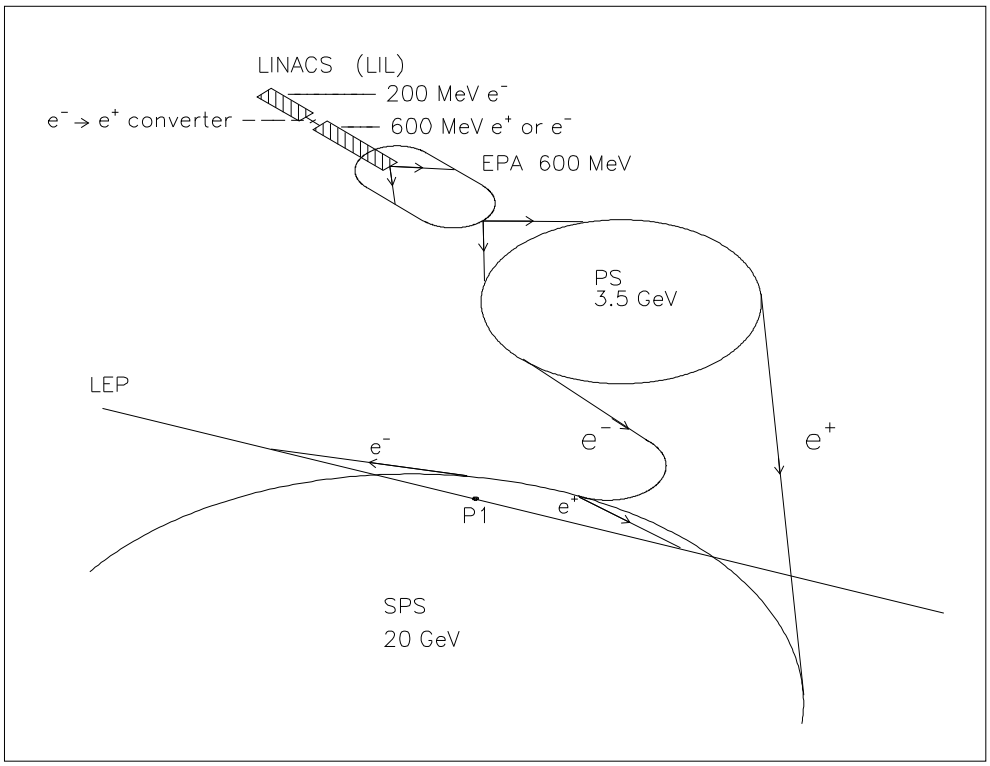

Figure 3.1: *The pre-accelerator machines for the LEP ring.*

In the first stage of the LEP Injector Linac (LIL) electrons of 200 MeV energy hit a target and produce positrons, which are filtered out with an average energy of 10 MeV and brought back to the second stage of the LIL. The electron beam comes from the Electron Gun machine and is also brought into the second stage of the LIL. After the LIL the beams are accelerated up to 200 MeV. Now the Electron–Positron Accumulator (EPA) follows, accelerating up to 600 MeV, together with collecting and focusing of the particles into bunches. The bunches are injected from the EPA to the CERN Proton Synchrotron (PS) operating as a 3.5 GeV e^+e^-synchrotron. The PS injects into the CERN Super Proton Synchrotron (SPS), which operates as a 20 GeV injector for LEP. The LEP ring accelerates the beams from 20 to 45 GeV.

The characteristic properties of an accelerator are the effective centre of mass energy and the luminosity. At LEP the centre of mass energy is simply the sum of the beam energies. A higher luminosity allows a proportional higher event rate dN/dt for the interesting processes.

$$\frac{dN}{dt} = \sigma \mathcal{L}, \tag{3.3}$$

where σ stands for the cross section of the process. From the current of particles divided by the diameter of the beam the luminosity reads:

$$\mathcal{L} = \frac{N^+ N^- k_N f}{4\pi \sigma_x \sigma_y} \cdot \tag{3.4}$$

In the following table some characteristic values from the years 1994-95 for the LEP performance are given.

Table 3.1: *Characteristic parameter of the LEP machine for the years 1994-95.*

circumference		26.7	km
radius		3.03	km
vacuum		$< 10^{-10}$	Torr
bunches in beam	k_N	4 or 8	
particles per bunch	$N^{\pm}$	4.2×10^{11}	
bunch length in z		≈ 10	mm
radius in x	σ_x	≈ 200	μm
radius in y	σ_y	≈ 10	μm
luminosity	$\mathcal{L}$	10×10^{30}	$\mathrm{cm}^{-2}\mathrm{s}^{-1}$
beam energy	E_{beam}	45-55	GeV
HF cavities		128	
frequencies	f_{HF}	352.2	MHz
wave length	λ_{HF}	0.851	m
circulation time of a bunch	t_{rev}	88.9	μs
circulation frequency	f_{rev}	11.25	kHz
distance of bunches (k_b=4)	t_b	22.2	μs

3.2 DELPHI Detector

DELPHI is the abbreviation for 'Detector with Electron, Lepton, Photon and Hadron Identification'. It is one of the four big particle detectors at the LEP storage ring. It consist of both conventional and more advanced subdetectors, which are used for the purposes of measuring and identifying the particles produced after e^+e^-annihilations. The DELPHI detector is a cylinder 10 m long and 9 m in diameter. It lies along the beam axis, which goes through the middle of the cylinder and is divided in a central region called 'barrel' and the 'forward' region, as can be seen in fig. 3.2. The barrel is closed at both ends by the endcaps, through which the electron and positron beams enter the central region where they collide. The following coordinate system is used: the origin is near the collision zone of the beams, while the z axis matches with the e^+ beam axis. The y axis goes up to the top and the x axis perpendicular to the z axis in the horizontal direction. The x–y plane forms the R-Φ plane, where Φ is the azimuth angle $\Phi = \tan y/x$ and R the radius of the origin to the point (x, y) : $R^2 = x^2 + y^2$. The angle θ is the polar angle and lies in the R–z plane.

The detector subcomponents are used to measure the tracks of the particles or to determine their energy or mass. In the barrel region the following subdetectors have been installed starting from the beam pipe:

- Microvertex Detector (VD) : R=5–11 cm, $25° \leq \theta \leq 155°$, three layer Silicon strip detector, for the reconstruction of charged particles tracks close to the interaction point and for measuring secondary vertices.
- Inner Detector (ID) : R=13–23 cm, $23° \leq \theta \leq 157°$, jet drift chamber and proportional chamber for the reconstruction of tracks in R-Φ and for the event trigger.
- Time Projection Chamber (TPC): R=28–112 cm,$|z| \leq 134$, $20° \leq \theta \leq 160°$, gas filled time projection chamber, which allows a reconstruction of charged tracks in three dimensions.
- Barrel Ring Cherenkov Detector (BRICH): R=120–190 cm, Cherenkov detector with gas and fluid as media for the identification of particles.
- Outer Detector (OD): R=198–206 cm, $43° \leq \theta \leq 137°$, gas drift chamber with good R-Φ resolution for the reconstruction of high energy tracks.
- High Density Projection Chamber (HPC) : R=208–260 cm, $43° \leq \theta \leq 137°$, electromagnetic calorimeter for measuring showers of electrons and pions.
- superconducting coil : R=265–310 cm, solenoid made of a Nb-Ti alloy , which is cooled with liquid helium down to 4.5° Kelvin. A 5000 Amp current gives a 1.2 Tesla magnetic field.
- Time Of Flight Counter (TOF): R=315 cm, layer of plastic scintillator with photo multiplier readout, for fast event trigger and cosmic veto.

- Hadron Calorimeter (HAC): R=320–479 cm, $10° \leq \theta \leq 170°$, apparatus to measure hadronic interacting particles, made from alternating layers of iron and wire chambers.
- Muon Barrel (MUB) : R=445, 480, 532 cm, $40° \leq \theta \leq 140°$, muon chambers in the barrel region, consisting of gas filled wire chambers, surrounded by thick layers of iron. They are used to identify muons in e^+e^-events and to reject cosmic rays.

In the region of the end caps the following components and subdetectors are installed.

- Small Angle Tile Calorimeter (STIC): Lead layers together with scintillator strips, to measure photons and electrons in regions of low ($10 \geq \theta \geq 2.5°$) angles.
- Forward Chamber A (FCA): $|z|$=155–165 cm, $11° \leq \theta \leq 33°$, three layer gas filled wire chamber, measuring three coordinates.
- Forward Rich (FRICH): $|z|$=166–266 cm, $10° \leq \theta \leq 40°$, as BRICH
- Forward Chamber B (FCB): $|z|$=267–283 cm, $11° \leq \theta \leq 35°$, four layers of gas chambers.

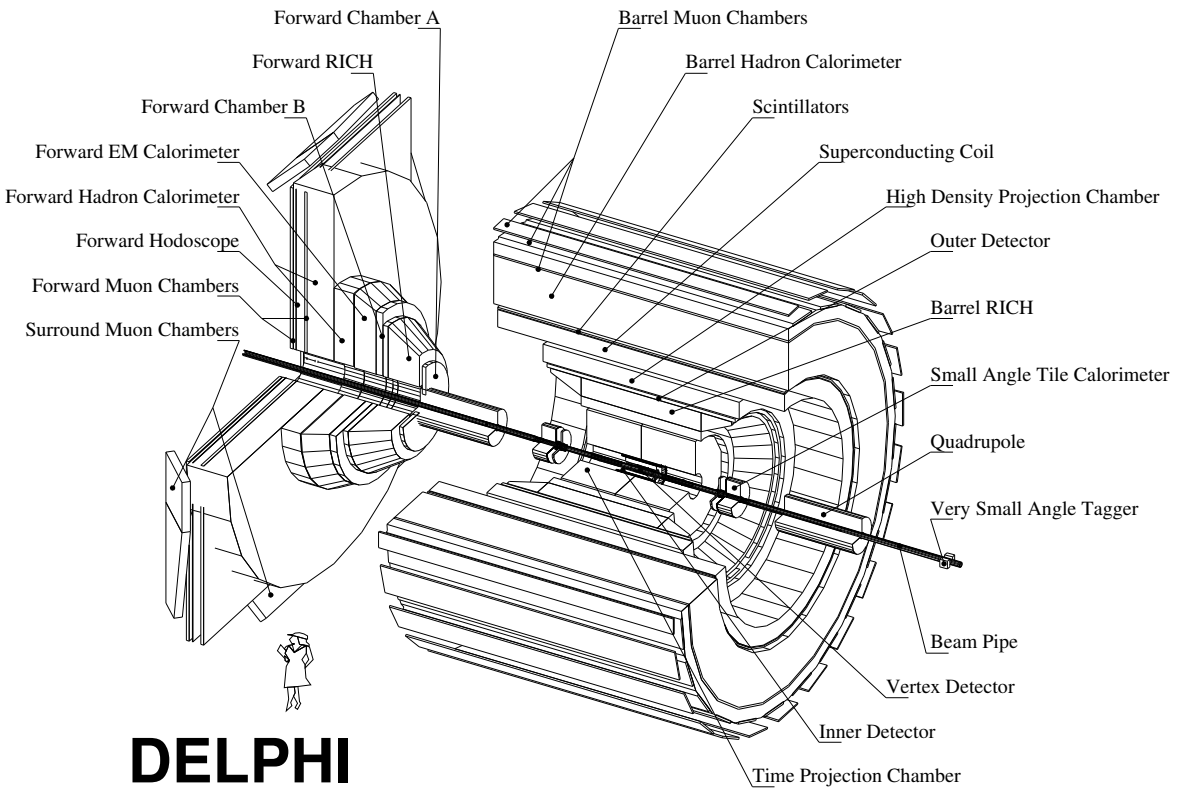

Figure 3.2: *The* DELPHI *detector open with one visible end cap.*

- Forward Electromagnetic Calorimeter (FEMC): $|z|$=284–340 cm, $10° \leq \theta \leq 30°$, lead glass calorimeter with photo triodes in the end read out.
- Forward Hadron Calorimeter (FHAC): $|z|$=340–489 cm, $11° \leq \theta \leq 42°$, as Barrel HAC
- Forward Muon Chambers (MUF): $|z|$=463 cm, $11° \leq \theta \leq 33°$ as MUB
- Surround Muon Chambers (MUS): Muon chambers, which complete the muon detection system outside DELPHI.

Additional details and numerical values can be found in the references [35] and [36]. The components used in the analysis are explained next.

3.3 DELPHI Track Chambers

A strong magnetic field is needed, to reconstruct the momentum of charged particles. A charged particle moving in a magnetic field followes a circular trajectory, defined by the Lorentz force. This allows one to compute the transverse momentum of the particle from the radius R of the circle:

$$\begin{aligned} \vec{F}_{Lorentz} &= \vec{v} \times \vec{B}q & (3.5) \\ &= \frac{v^2}{R}m \quad \text{(radial force)} & (3.6) \\ \rightarrow p_T &= qR \cdot B \end{aligned}$$

With the DELPHI magnetic field of 1.2 Tesla this gives a curvature radius R of 2.78 m for 1 GeV/c transverse momentum.

$$R = \frac{2.78\text{m}}{\text{GeV}/c} \cdot p_T \tag{3.7}$$

The following components are used to reconstruct track points and elements of charged particles in the detector. The complete path is reconstructed from these elements.

3.3.1 Microvertex Detector (VD)

The microvertex detector in DELPHI is next to the beam pipe. A detailed description can be found in [37]. It consists of three concentric layers of silicon microstrip detectors at an average radii of 6.3, 9.0 and 10.9 cm within the central region of the DELPHI detector. The layers at average radii 6.3 and 10.9 cm, are called the Closer and Outer layers. The Closer layer covers the region from –14 to +14 cm along the z axis, the

Outer layer a region from –11.5 to +11.5 cm. Both layers consist of double sided silicon strip detectors, meaning that a double readout allows the determination of two variables. The layer between the Outer and the Closer layer at 9.0 cm radius is called the Inner layer and has single sided readout. It covers the region of –11.8 to +11.8 cm in z. Each layer consists of 24 modules, each module built with four silicon detectors along z. The four Detector modules are wire bounded in series and read out at both ends of each module. From the geometry which is shown in fig. 3.3 it can be seen that neighbouring modules overlap as 10% of their surface. This feature is later (see section 4.1.3) used in the offline treatment to align the vertex detector.

The principles of a track measurement with a silicon wafer is explained in the following. Technical details can be found in [38][39]. A passing track creates about 20000 electron hole pairs in the silicon material. This is not sufficient enough, since many free carriers destroy such a signal. To measure signals of passing tracks a mechanism is needed to lower the number of free carriers. This can be done by cooling the semiconductor or using a reverse biased p-n junction. In a p-n junction one region is an n-type, the other a p-type semiconductor. Because of the difference in the concentration of electrons and holes between the two materials, there is an initial diffusion of holes towards the n-region and a similar diffusion of electrons towards the p-region. The diffusing electrons fill up holes and the holes capture electrons. The remaining charged atoms create an electric field gradient across the junction. Because of the electric field, there is a potential difference across the junction. The region of changing potential is known as depletion zone and has the special property of being devoid of all mobile charge carriers. Any charge deposited within its volume can be collected. Contacts placed on either end of the junction device detect a current signal proportional to the ionization. In Particle Physics a planar technology of the silicon is used. An n-type silicon is used as the base material onto which p^+ diode strips with aluminium contacts are implanted. An n^+ electrode is similarly implanted on the opposite face which yields a depleted medium of the n-type bulk material in between. The thickness of the detector is about 300 μm. The good precision of the p-type strips provides a spatial information. For the usual single sided module, e.g. the Inner layer, the n^+ back is a plane. For the double sided layout the p and n side diodes are orthogonal to each other, formed in strips. To reduce the amount of expensive electronics, the readout lines of several geometrical distant of the n side are joined up, leading to a multiplexing of the z-hits. Multiplexing means an electric channel can corresponds to two or three z positions separated by more than 1.9 cm. A novel feature of the double sided detector is the so called 'flipped module' design. This implies that the p and n sides of the detectors can be read out as distinct positive and negative signals at the end of the detector. Thus one layer can be separated in four subcomponents and the z-edges of these modules are precisely known.

For the R-Φ hit measurement the tracks originating from the centre of DELPHI cross the silicon at similar angles, whereas for the z-hits the angle varies from 90° in the centre down to 25° at the edge of the Closer layer modules. For large angle tracks, the charge is spread over several z-strips. It is therefore clearly advantageous to vary the pitch for tracks in the forward region, i.e. the distance between two readout strips.

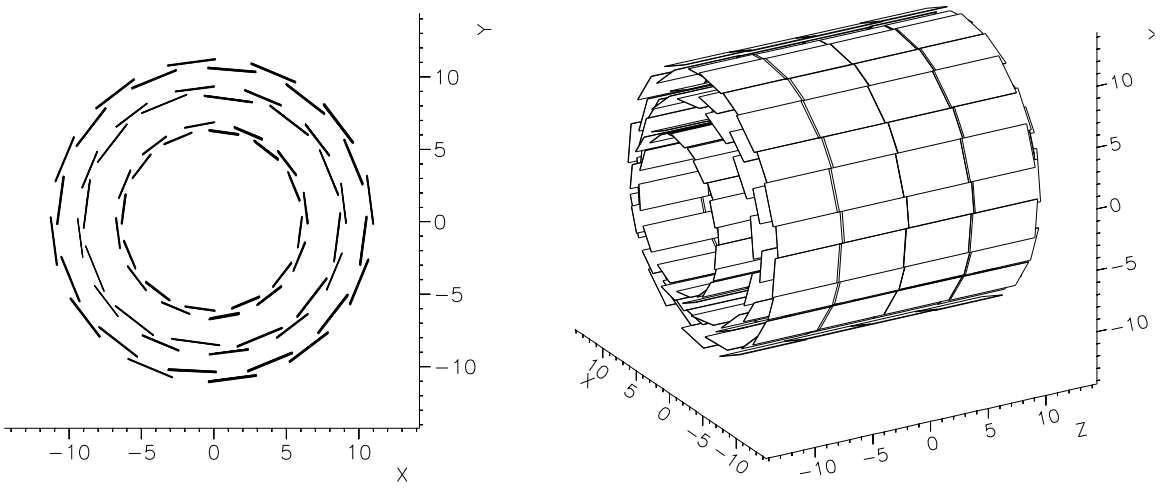

Figure 3.3: *Schematic layout of the microvertex detector in cm. Left hand side shows the projection transverse to the beam, on the right hand a perspective view is given.*

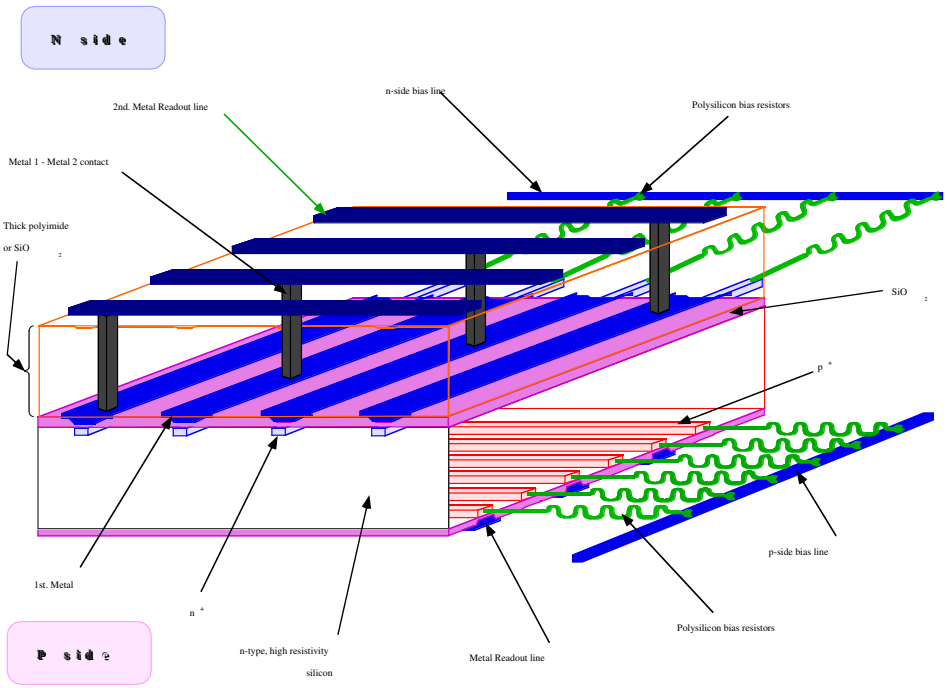

Figure 3.4: *Cross section of a double sided detector; p and n side readout strips allow the measurement of two coordinates.*

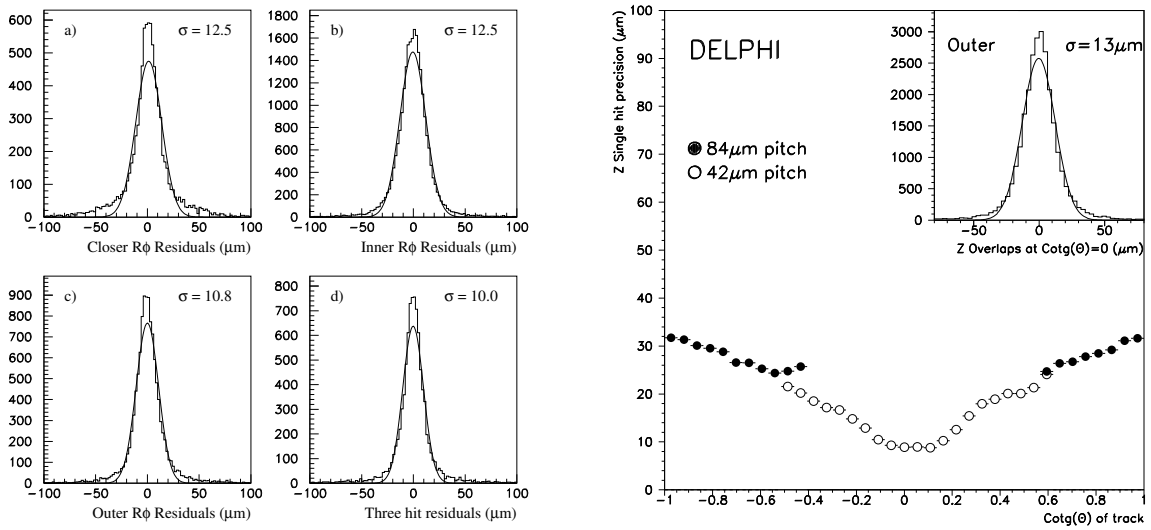

Figure 3.5: *Left: spatial resolution of R-Φ hits, for a) Closer overlap tracks, b) Inner overlap tracks and c) Outer overlap tracks. The width of the distributions has to be divided by $\sqrt{2}$ to get the single hit precision of the layer. d) shows the Inner layer residuals for track with hits in three layers. This width has to be divided by $\sqrt{1.5}$; Right: the spatial resolution in z for several θ values and at 90° for the Outer layer.*

This is done by changing from 50 to 100 to 150 μm for the Closer layer and from 42 to 84 μm for the Outer layer. The p-strips for the R-Φ hits have a fixed pitch of 50 μm over the whole detector. The spatial resolution for the R-Φ hits is about 7μm. The precision in z varies with θ due to enlarged clusters in the modules from 8–20 μm, as shown in fig. (3.5). The precisely measured spatial information near the primary vertex allows a separation of b-quark events, as described later in chapter 5.

3.3.2 Further Track Chambers

Inner Detector (ID)

The Inner Detector is constructed as a jet drift chamber, divided in 24 Φ sectors. In every of these sectors the field wires build an electric field parallel to the R-Φ plane. The produced free charges of a passing particle in the gas (CO_2:C_4H_{10}:C_3H_7OH/94.8%:4.5%:0.7%) are measured in the middle of a sector by the signal wires. This allows a reconstruction of points in the R-Φ plane. For the resolution of the mirror images a five layer Multi Wire Proportional Chamber (MWPC) is constructed around the jet chamber. Each layer consists of 192 signal wires for the R-Φ measurement and concentric cathode strips for the z measurement. The acceptance in the polar angle for the jet chamber is $23° \leq \theta \leq 157°$ and for the MWPC $30° \leq \theta \leq 150°$. The ID reaches a resolution of $\sigma(R\text{-}\Phi) = 50\mu$m and $\sigma(\Phi) = 1.5$ mrad. Two tracks can be separated if they are more than 1 mm apart. The ID is the most

important event trigger in DELPHI with a fast readout of 3 μs.

Time Projection Chamber (TPC)

The TPC is the biggest and most useful apparatus for the measurement and reconstruction of charged tracks. It starts at R=28 cm, covers about 3 m in z (with a sensitive length of $\pm$134cm) and ends at R=120 cm. As shown in fig. 3.6 the TPC is divided in two halves, which lie right and left of the interaction point. The electrostatic field of 187 V/cm in each half is directed to the end caps parallel to the beam axis and the magnetic field of the superconducting coil. The volume of the TPC is filled with an argon/methane (80:20%) mixture. The ions produced by a passing particle are drifted by the electric field parallel to the z axis and are read out at the end plates. Here 16 concentric pad rows and 192 anode wires are installed. In each of the 2×6 sectors are 1680 pads which form the cathode rows. This allows in total 16 space points per track to be measured. Because of the relatively long drift distance the diffusion, particularly in the lateral direction may become a problem. This is reduced by the parallel magnetic field which confines the electrons to helical trajectories about the drift direction. The R-Φ coordinate is measured with the centre of gravity of the charge clouds on cathode and anode. The z component is determined from the drift time compared with the trig-

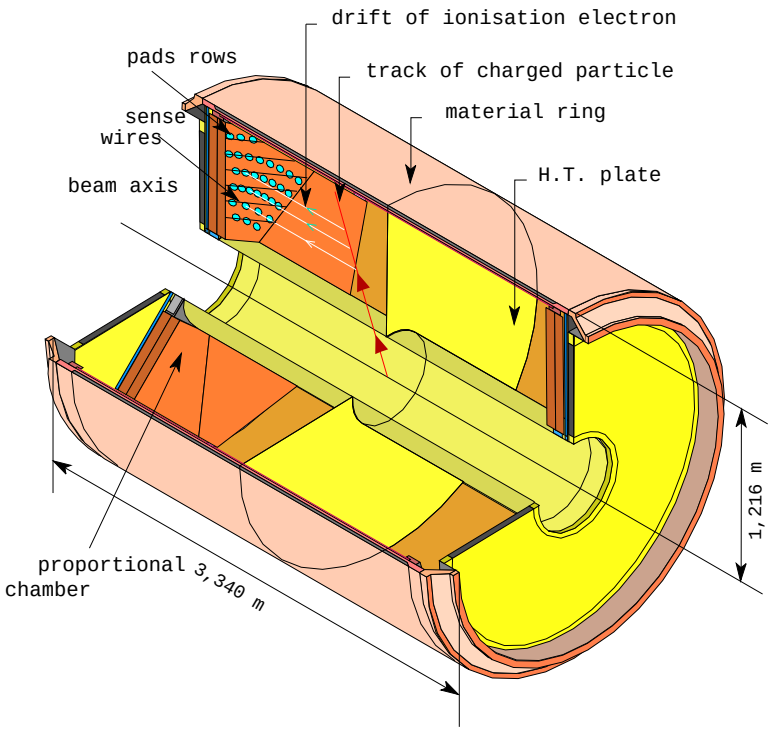

Figure 3.6: *The TPC geometry together with charged track passing. The pad rows are indicated as circles the sense wires cross them as lines. A charge coming from the ionization of a track drifts toward the endcaps.*

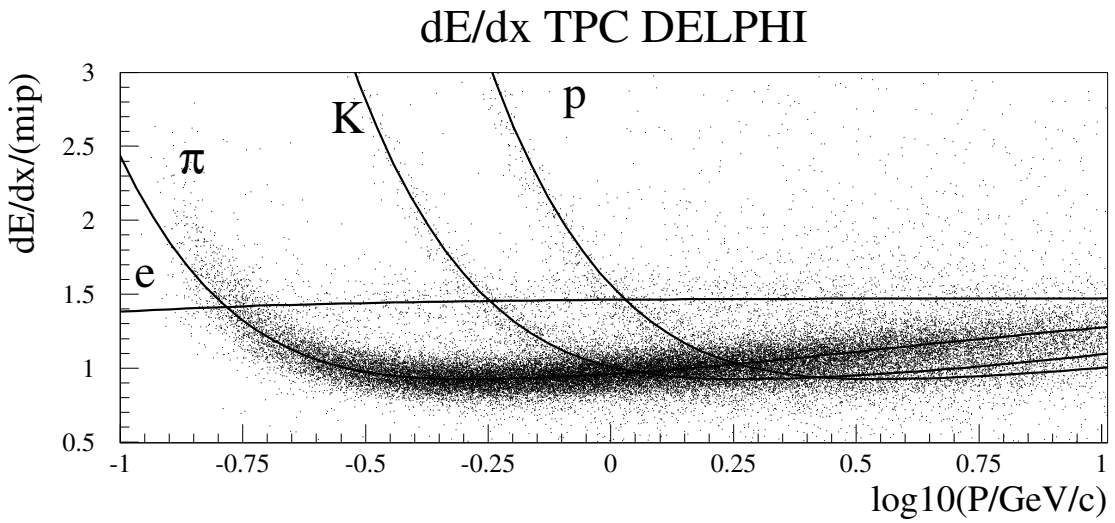

Figure 3.7: *Specific energy loss dE/dx in the TPC as a function of the momentum, the lines show the theoretical expectation. The difference for low momentum pions comes mainly from the uncertainty of the measured momentum. Tracks in this momentum region* $(-0.9 \leq \log 10(P/c \leq -0.75)$ *loose a lot of energy in front of the TPC.*

ger signal. For this purpose the drift velocity of the gas has to be calibrated during the whole data taking period. The spatial resolution in R-Φ of the TPC is about 180–280 μm, the resolution in z is 880μm. The separation of two tracks is possible if the tracks are more than 1cm apart.

Beside the spatial information from the pads the sense wires provide up to 192 ionization measurements per track, which are used to calculate the specific ionization of the tracks. Hits which are too close in time (equivalent to z) cannot be correctly separated and are dropped for the dE/dx calculation. This corresponds to a separation of at least 2 cm for tracks at 90° polar angle. As explained in section 4.3 a Landau distribution is expected for the signal distribution. To reduce the tails the highest 20% of the signals are removed. The dependence of dE/dx on the momentum of the particle is described by the Bethe-Bloch formula [39] and displayed in fig. 3.7. The energy loss coming from excitation and ionization of an incident particle which passes through matter is computed :

$$-\frac{dE}{dx} = 2\pi N_A r_e^2 m_e c^2 \rho \frac{Z}{A}\frac{z^2}{\beta^2}\left[\ln\left(\frac{2m_e v^2 W_{max}}{I^2}\right) - 2\beta^2 - \delta\right] \tag{3.8}$$

with:

r_e:	classical electron radius	A:	atomic weight of absorber
m_e:	electron mass	ρ:	density of absorbing material
c:	speed of light	z:	charge of incident particle
N_A:	Avogadro's number	v:	velocity of the particle
I:	mean excitation potential	β:	v/c of incident particle
Z:	atomic number of absorber	W_{max}:	max. Energy transfer

The maximum energy transfer W_{max} for a single collision of an incident particle with mass M is:

$$W_{max} = \frac{2m_e c^2 \beta^2 \gamma^2}{1 + 2m_e/M\sqrt{1+\beta^2\gamma^2} + (m_e/M)^2} \cdot \tag{3.9}$$

The term δ represents the density effect correction which becomes important for solids [20]:

$$\delta = \ln(\hbar\omega_p/I) + \ln\beta\gamma - 1, \tag{3.10}$$

with $\omega_p = \sqrt{Z\rho e^2/\epsilon_0 \epsilon m_e}$ being the plasma frequency.

The Bethe-Bloch formula shows a characteristic $1/\beta^2$ dependence for low momentum and a minimum at $\beta\gamma \approx 3.5$. Particles at this state are called minimal ionizing particles (mip). After the minimum the relativistic rise occurs due to the expansion of the transversal electrical field component of the passing particle. This rise goes logarithmically and the amount is different for gases and solids, according to the density effect. The electric field of a passing particle in matter polarises the surrounding atoms along the path. Electrons far away from the path will be shielded from the full electric field, making these electrons contribute less to the energy loss. After the rise the curve saturates.

Outer Detector (OD)

The Outer Detector lies between the barrel RICH and the electromagnetic calorimeter (HPC). It is the tracking detector with the largest distance to the interaction point (approx. 2 m). Thus the OD is able to improve the measurement of high energy tracks, which have a small curvature and completes the reconstruction of VD, ID and the TPC. The device consists of 24 modules, which overlap partly and allow a complete coverage of the azimuthal region. Each module is made of five layers of drift tubes, which are parallel to the beam pipe between radii of 198 and 206 cm. The drift tubes allow a good resolution in R-Φ of 110 μm and from the time differences of the signals at the end of the chambers the z coordinate can be obtained with $\sigma_z = 3.5$cm. The OD also contributes to the event trigger decision, as it has a fast readout of 3μs.

Tracking Performance

Results from several tracking components (VD, ID, TPC and OD) are combined to make more precise tracks. The alignment of the components and the disentangling of systematic effects (shifts, twists, etc.) are essential for good momentum resolution. Using $Z_0 \to \mu^+\mu^-$ events the momentum resolution in the barrel part of the detector is determined to be:

$$\sigma(1/p) = 0.57 \times 10^{-3}(GeV/c)^{-1} \ , \tag{3.11}$$

combining VD, ID, TPC and OD track elements [36]. The momentum resolution in the forward region ($20° \leq \theta \leq 35°$) is

$$\sigma(1/p) = 1.31 \times 10^{-3}(GeV/c)^{-1} \ , \tag{3.12}$$

using all available VD and FCB information.

3.4 Online System

The DELPHI online system has to guarantee the stability of the whole detector. Power and gas consumption are monitored and the security provided against fire and breaking of gas or water pipes. These are done by a General Safety System which controls the necessary flows of electricity, gas and water. Another important task is the slow-control of high voltages, technical condition of the detectors and working of the readout electronics. These things are monitored by the slow-control maestro. This person is needed 24 hours a day during data taking and in the periods when flammable gas is inside the detector.

Additionally a trigger and data acquisition system is needed to steer the data readout system. The trigger system is composed of four successive levels (T1, T2, T3 and T4) of increasing selectivity. The T1 acts as a loose pre-trigger while a positive T2 decision triggers the acquisition of the data collected by electronics. In T1 fast tracking detectors (ID, OD, FCA and FCB) and scintillator arrays in the barrel region and inside the calorimeters are used. In T2 this information is complemented by signals from the TPC, HPC and MUF together with combinations of signals from different subdetetectors. The T1 and T2 trigger decisions are taken 3.5 μs and 39 μs after the Beam Cross Over, which happens every 22 μs. This causes a dead time of T1 and T2 of about 3%. T3 and T4 are software filters performed asynchronously with respect to the BCO. T3 checks the T2 decision using the full granularity and resolution rejecting half of the T2 events. T4 suppresses background and classifies the events for physics analysis. The efficiency for multi-hadronic events is 99.9%. All T2 events are stored as raw data on tape cassettes. The run and event number identify the event.

3.5 Offline System

The offline chain is shown in fig. 3.8. The processing removes unnecessarily detailed information as more advanced informations become available from standard packages. This reduction of data is necessary for the effective handling of millions of multihadronic events.

Short DST Creation

The track segments of charged particles are mainly reconstructed from the raw detector data by the DELANA package. It contains alignment and calibration from each subdetector. The output is called a DST (Data Summary Tape), containing a tree structure of banks based on the reconstructed vertices and tracks. The size of a multihadronic Z^0 event is about 80 kbyte. At this stage all measured track elements are stored with errors and selected technical data.

To reduce the amount of data per event and yet have optimum particle identification the following packages are executed and the detector specific data are dropped.

- DSTFIX : Applies remaining alignment and calibration corrections together with improved track fits.
- AABTAG : Computes the primary vertex from tracks and calculates an effective variable to select $b\overline{b}$ events.
- ELEPHANT : Improves photon, electron and π^0 identification.
- MUFLAG : Identifies muons.
- RECV0 : Identifies Λs and K^0s.
- HADIDENT : Uses the Cherenkov detector and TPC dE/dx information to separate $K^{\pm}$, p and $\pi^{\pm}$.
- MAMMOTH : Finds hadronic interactions and reconstructs VD tracks.[2]

The Short DST contains all this information in a third of the initial DST size for one event. This can be reduced further to the Mini DST where nearly all detector information is removed.

Detector Simulation

The aim of the simulation is the measurements of detector effects and acceptances, to work out solutions for specific problems with a model near to the real world. For this

[2] Explained in chapter 4.

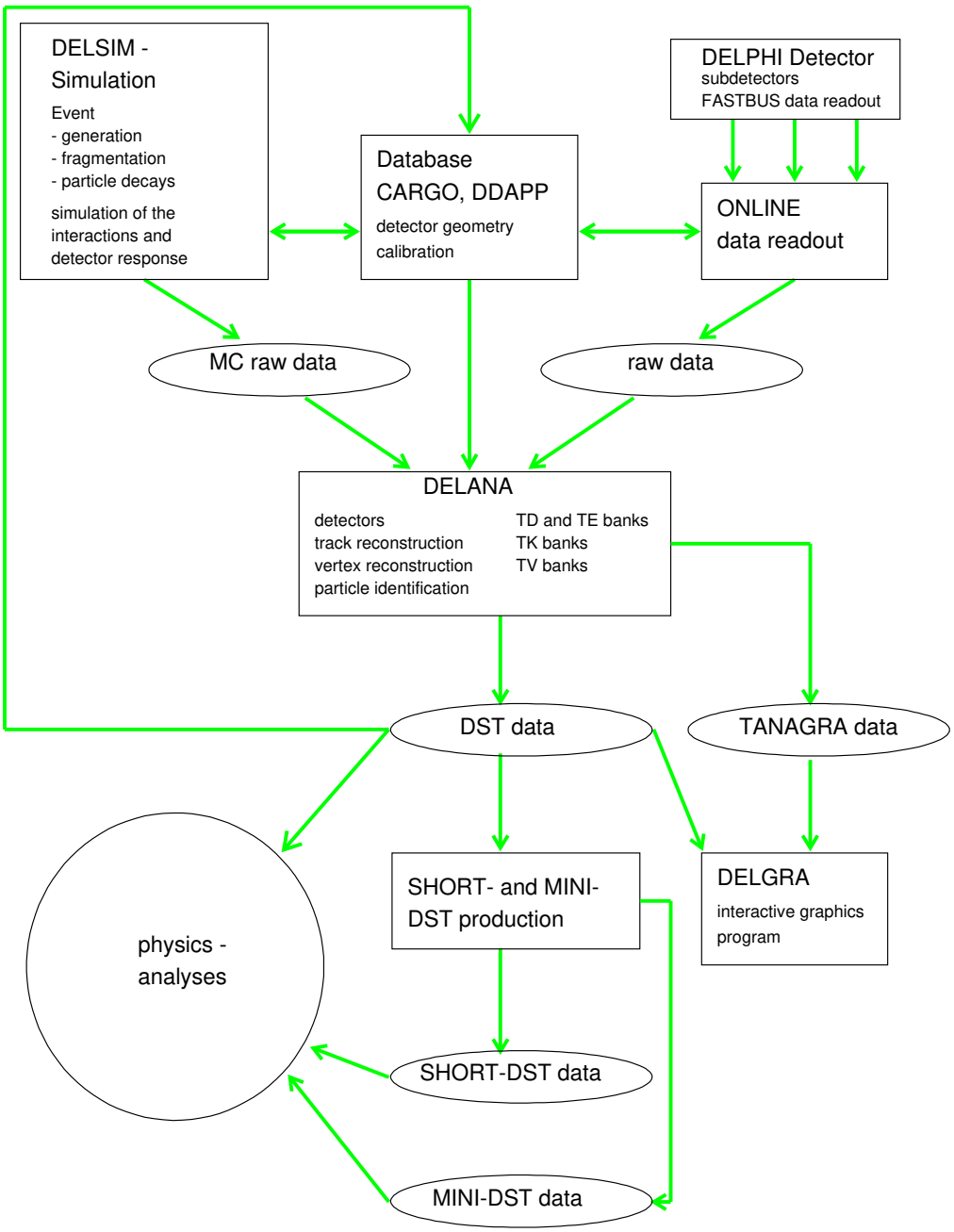

Figure 3.8: *Schematic view of the* DELPHI *offline reconstruction. Starting from the raw data the final data for the user are the Short and Mini DST.*

purpose the complete raw data has to be reproduced and the offline flow from raw data to Short DST is repeated for the simulated events as for the real data. This checks all of the whole offline chain, starting from DELANA. The DELPHI simulation program DELSIM consists of three parts:

1. Generation of elementary physical processes for production and decay of particles: JETSET[15] is used for multihadron events, BABAMC[40], DYMU3[41] and KORALZ[42] include the detailed models for e^+e^-, $\mu^+\mu^-$ and $\tau^+\tau^-$ events.

2. Detector simulation of secondary interactions, showers and ionization includes photoelectric effects, delta rays, bremsstrahlung, annihilation of positrons, pair production, Compton scattering, weak decays and nuclear interactions. The distributions of material are stored in a data base.

3. Simulation of response of the detectors as signal height, noise and thresholds: First the particles are followed inside the sensitive detector material then signals are simulated. The processing can then be done as for the real data. This is done for each subdetector.

The simulation gives 'MC raw data' which are processed like the real data, see fig. 3.8. The simulation of events is done by large computer clusters of several institutes and collected at CERN for further Short DST processing.

On the simulation sample three levels can be accessed. The generator level, the simulation level and the reconstruction level. The **generator level**/SH-bank contains basic physical processes according to a physical model. The four momentum of quarks and hadrons and decay are available. On the **simulation level**/(MC truth) all tracks from the previous level are simulated in the subdetectors knowing their source and origin. This level therefore contains only 'true' tracks, whereas on **reconstruction level** all tracks which have been reconstructed are stored. Where uniquely possible, a link to the simulation level exists. This allows one to follow the development of an event or decay from the physical source to the reconstructed tracks.

4

Vertex Detector Tracking

The content of this chapter deals with the so called 'VD tracks' and forth tracks measurements with the vertex detector. For the better understanding of the track reconstruction the track definition itself and the association of vertex detector hits are introduced. The VD tracks and the dE/dx measurement with the vertex detector are a part of the 'MAMMOTH' project, which was initiated to improve the track reconstruction of the DELPHI experiment [43].

4.1 Track Reconstruction in general

Track reconstruction relates measured points in the chambers to trajectories representing physical four momentum vectors for charged particles. In the ideal case this can be done both for the detector closest to the production point (e.g. vertex detector) and for the most distant calorimeters or the Outer Detector.

In the DELPHI coordinate system the $x-y$ plane is perpendicular to the magnetic field $\vec{B}$ which is parallel to the z-axis. The R-Φ plane is another expression for the $x-y$ plane with $(x,y) = (R\cos\Phi, R\sin\Phi)$.

4.1.1 Track Definition

The path of a charged particle in a magnetic field forms a helix. A helix is a circle in the R-Φ plane perpendicular to the magnetic field and a straight line in z versus the R-Φ tracklength S. The general definition of a track, independent of the measured points and detectors used, defines tracks at the point of closest approach to the origin in R-Φ (0,0), also called the **perigee**. From this position the closest distance ϵ_{xy} in the R-Φ plane to the origin and the curvature $\kappa = 1/R$ are taken, where R is the radius of

the circle through the track. The sign of ϵ_{xy} is defined by :

$$\epsilon_{xy} = sign(R) \cdot (|R| - R_V), \tag{4.1}$$

where R_V is the distance from the centre of the circle to the origin and the sign of $\kappa = 1/R$ coming from the charge of the particle. The track is fully described in the R-Φ plane by $\epsilon, \varphi, \kappa$. Where the angle φ gives the R-Φ direction of the track. A drawing in fig.(4.1) illustrates this geometry.

Only the direction and a position in z are needed for the third dimension, since the z-component of the momentum does not change in the magnetic field which is parallel to the z-axis. Z_P is the z coordinate of the extrapolation of the track at the closest distance approach or perigee, see fig.4.1. The angle Θ can be taken from

$$\tan\Theta = \frac{\Delta S_{xy}}{\Delta z} \ , \tag{4.2}$$

with ΔS_{xy} the track length for a corresponding change Δz. This can be derived from $\tan\Theta = \frac{P_T}{P_Z}$ with $P_T^2 = \sqrt{(P_x^2 + P_x^2)}$ and $P = \Delta S/\Delta t$. Finally the helix is defined by the five parameters:

$$\epsilon_{xy}, Z_P, \Theta, \varphi, \kappa(= 1/R) \ . \tag{4.3}$$

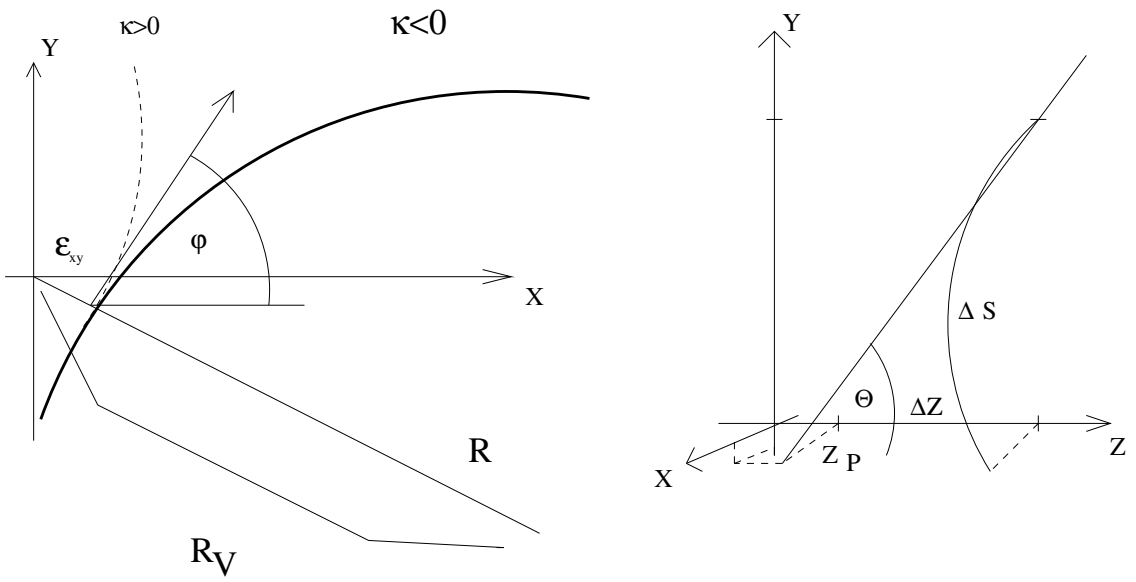

Figure 4.1: *Left: the definition of the perigee parameters in the x-y plane. A track with negative curvature $\kappa < 0$ and positive impact parameter ϵ is drawn. R_V is the distance from the circle centre to the origin. The centre of the circle lies outside the drawing. A track with positive curvature is also shown. On the right the definition of Z_P and Θ is shown.*

There are other definitions, especially when the track passes a specific cylinder or a surface where the parametrisation at a given radius = R is needed. Often the value $R\Phi$ comes from a measured point $\vec{x} = (R\cos\Phi, R\sin\Phi)$ in the x-y or R-Φ plane. (Note Φ is used for a position in space, φ is used for the direction of the momentum.) If not mentioned otherwise in the text, definition (4.3) is used. The primary vertex can be used instead of the origin. This depends on the stage of the analysis: at the beginning of the reconstruction the primary vertex is not or badly defined. For this reason it is a safe and unambiguous convention to keep this parameter set (4.3) related to the origin and transform it later in the analysis when the physical information is needed and the primary vertex is available.

4.1.2 Usual Tracking Procedure

The reconstruction of tracks in an event (program DELANA [44]) from the raw data uses the following algorithm:

(1) Analysis of the raw data in the subdetectors and formation from the measured track points (TD) to track elements (TE)

(2) Combination of track elements to track candidates or strings (TS)

(3) A fit of the track (TK) parameters through the chain of TS is done which gives a first track. Ambiguities in this stage of the process have to be resolved.

(4) Final fit of the track parameters after a global alignment correcting the spatial resolution is available.

(5) Extrapolation to the Vertex Detector and association of VD hits to the tracks and a final estimation of errors is made.

The most interesting steps are (2) and (5). In step (2) mostly TPC TEs are used. Outward and inward extrapolations to the Outer Detector and Inner Detector form most of the tracks in the barrel region. This implies that only tracks with a reasonable TE in the TPC are fully reconstructed and get Vertex Detector hits by the extrapolations in step (5). Because of this procedure the Vertex Detector hit association strongly depends on the extrapolation of the TPC tracks, and might suffer large failures due to misalignment, errors in the material description or a wrong extrapolation modelling of energy loss and multiple scattering. In practice it has been observed that a lot of tracks cannot be reconstructed, because they end in TPC cracks or boundary regions of the TPC sectors. Other reasons might be the association of a wrong Inner Detector (e.g. mirror image) TE or a secondary interaction happened in the detector material, which spoiled the reconstruction.

4.1.3 Offline Treatment of the Vertex Detector

Beside the geometrical and technical description in chapter two, some more information about the vertex detector and track reconstruction are given here.

Cluster Reconstruction

A cluster representing the point of a passed track has to be defined for the strips on the silicon detectors. A channel is included in a cluster if its pulse height, i.e. signal (S) to noise (N), is greater than 2.5 on the p-side (R-Φ hits) and 1.4 on the n-side (z-hits). This allows a larger spread of the n-side clusters at larger incidence angles. The position where the particle traversed the silicon is calculated from the charge distribution between neighbouring channels. On the p-side the position is reconstructed by interpolation of the two highest consecutive signals of the cluster; P_R and P_L, the centre of the cluster is estimated as:

$$\eta = \frac{P_R}{P_R + P_L}, \tag{4.4}$$

where $\eta = 0$ implies the hit was exactly on the left-hand strip, and $\eta = 1$ implies the hit was exactly on the right-hand strip. The situation is more difficult for z-hits, since the clusters can be significantly larger along the z axis in the case of forward tracks. Starting with the midpoint of the cluster between the first(head) and the last (tail) channels, an advanced algorithm is used, assuming a model for the pulse shape on the edges of the cluster [45].

Association of Hits to Tracks

For the association of the R-Φ hits the algorithm looks for combinations of two vertex detector points in different layers that satisfy certain track hit residual cuts. A track is forced through each set of two points, keeping the curvature fixed, and additional points are associated in the third layer and in the sector overlaps. The cuts depend on the track errors, including the contribution from multiple Coulomb scattering. The most common result is three hits in R-Φ and two in z, but there is also a useful number of overlaps that can be used for alignment and efficiency studies, leading to a maximum number of six hits per track in R-Φ and four in z. Tracks with a single solution are associated first. All solutions with three layers are associated before any with two, all with two are associated before any with one. The R-Φ association runs first, then the tracks are refitted and the z association begins. Multiplexing of the n-side strips does not spoil the pattern recognition, since the possible z positions of each hit are separated by at least 1.9 cm. Possible ambiguities are reduced by the simultaneous association in two layers.

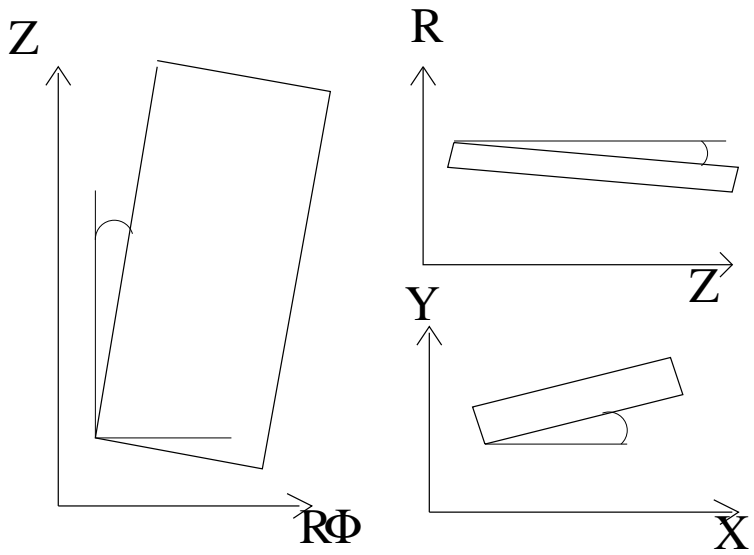

Figure 4.2: *The $R\Phi$-z corrections for the vertex detector modules. The modules are twisted and tilted, as shown on the right side, causing a transformation in $R\Phi$-z space as illustrated on the left side.*

Alignment of the Vertex Detector

In order to measure spatial information to better than 10μm implies to know where the detector is installed in space with the same precision. This introduces a complicated but necessary procedure which shows the sensitivity of high precision spatial measurements in a High Energy Physics detector; see [46] for more details. By making optical measurements the position of the strips on each module is known with a precision of 2 μm. After installing the module on the half shell, the position of the module is also measured with an optical instrument. This gives a total precision on the strip position of 25 μm. The DELPHI-vertex detector is installed after the mechanical work on the detector. Before closing the endcaps, the vertex detector is pushed inside the barrel region surrounding the beampipe. At this stage the position is only known with a precision of a few mm. Z^0 decays into dimuons ($\mu^+\mu^-$) are most used to improve the alignment. The spatial position may differ from the one known from the optical survey made before installation. As shown in figure 4.2 the modules can vary their position from the ideal frame, causing extreme misalignments. This makes a large difference from the local to the general coordinate system. Every position in R-Φ needs to be corrected as a function of the corresponding z position, by doing a transformation in $R\Phi$-z space as indicated on the left drawing in fig. 4.2. A shift of 30 μm in R-Φ or a shift in z of 10 mm are possible. Using loose criteria for the association of hits to external tracks, the first $\mu^+\mu^-$ tracks are used to realign this positioning to better than 100μm. In the internal alignment procedure the three layers are treated differently. The Outer layer is treated as the 'master layer' and aligned using all possible R-Φ and z constraints from overlap tracks. Next the Closer layer modules are aligned individually with respect to the corresponding modules of the Outer layer. Finally the Inner layer

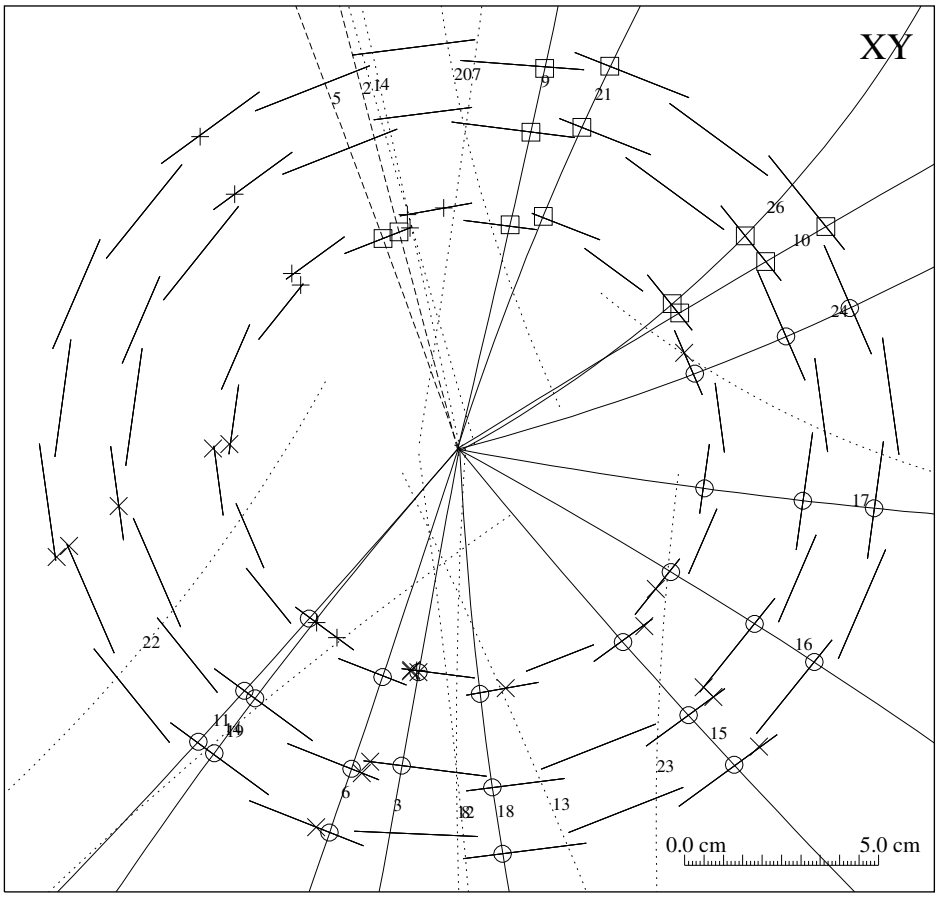

Figure 4.3: *Event with obvious missing tracks which could be determined with VD tracks. Two of the missing tracks are visible in the upper left quadrant, another one in the lower right quadrant.*

modules are aligned individually with respect to the corresponding modules of Outer and Closer layer in the same sector. The overlap tracks allow the determination of relative translation and rotations, resulting in the final transformation matrix. Finally the rigid body obtained from the previous steps is aligned externally. The alignment constants are determined using muon pair tracks reconstructed in the other tracking detectors of DELPHI. The R-Φ hits are afterwards known with a precision better than 8 μm, the precision in z at 90° is 12.5 μm.

4.2 Vertex Detector Tracks

An approach for tracks which have not been measured in the TPC was done by the ID-VD-project [47]. TEs of the Inner Detector where extrapolated to the Vertex Detector to associate reliable hits. At least two hits in the vertex detector were required for an

IDVD-track together with a track string in the Inner Detector. No TPC information was needed, since the Vertex Detector of the years 1994-95 could also measure z. This procedure was able to recover tracks which crossed TPC cracks or have been too low in energy. This method has failures due to the Inner Detector spatial resolution and inefficiency. Event displays like the one in fig.4.3 suggested building tracks from Vertex Detector hits only, so called '**VD tracks**'. Candidates giving hits in three layers together with measured z hits in the innermost and outermost layer could be completely determined. The measurement of the curvature is limited. As the tracks are short, the momentum resolution for high momentum is not expected to be good. The opposite case of extremely low momentum tracks should be measured best with this method. Moreover tracks that could not even reach the TPC, being too soft, should be seen as VD tracks for the first time. Other sources for such triplets would be tracks passing through the TPC Φ cracks, tracks interacting with the detector material outside the vertex detector and the decay of charged particles as: $X^{\pm} \rightarrow Y^{\pm}+$ neutral particles. An iterative procedure is used starting from free hits in the Outer layer and based on the mathematical rule that a track in R-Φ is fully defined by three points. This algorithm starts with the R-Φ association, following the scheme outlined below and does the z association in the last step. Detailes of the R-Φ and z associations are given in the next two sections.

(1) Free hits from the Outer layer are taken and a straight line to the primary vertex is used to choose a module from the Closer layer.

(2) Free hits in this Closer module are collected and a first track made from hits of the Outer layer, Closer layer and the Primary vertex.

(3) This track is extrapolated to all layers and hits closest to the extrapolation are selected.

(4) The track parameters from the selected hits are computed and required to be consistent with the z edges of the $R\Phi$ modules.

(5) Association of z-hits is done. Modules in the Outer and Closer layer which measured the $R\Phi$ hits are investigated for free z-hits.

(6) The final track fit is performed to calculate the track parameters (4.3) and the full covariance matrix.

This method produced two classes of tracks, which are flagged with a `PXPHOT`[1]-code to see later in the analysis which kind of track was reconstructed :

1. Tracks with full information, i.e. at least three hits in R-Φ and 2 z-hits: Θ and Z_P can be calculated; (Code=75).

[1]The `PXPHOT`-code can be received by calling `CALL PXGECO(LPA,ICODE)`.

2. Tracks only measured in $R\Phi$, which do not have associated z-hits, either the association was not unique or no z-hits could be found.
   These tracks get a Θ calculated from the primary vertex and the middle of the $R\Phi$ module and a large Θ error; (Code=77).

The details of the R-Φ- and z-hit association are described in the next two sections, the results and the characteristics of these tracks are discussed section 4.2.3.

4.2.1 Association of R-Φ Hits

The algorithm was invented to reconstruct additional tracks from remaining unassociated vertex detector points, after the normal track finding was run.

Since the z edges of the $R\Phi$ modules are known the module centre in z can be computed and serves sometimes for orientation or error calculation. The Θ_M is computed from a z in the middle of the $R\Phi$ module in z and the z coordinate of the primary vertex. The VD track reconstruction follows these steps:

Step 1: A loop is started over all free R-Φ hits in the Outer layer. For a free R-Φ hit the Θ_M from the module centre in z is computed. Then the corresponding z value of the track in all three layers is calculated to apply the twist and tilt corrections of the R-Φ coordinates. Given the R-Φ coordinates the φ and $R\Phi$ can be estimated. These, together with the Θ_M of the module centre and $Z_P = 0.01$ cm are a good first estimate of the track parameters used to make an extrapolation to the Closer layer. This is equivalent to a straight line to the origin. The Closer module is selected in a straight forward way; from this module further free R-Φ hits can be taken.

Step 2: A sample of free hits can be selected from the extrapolation in the Closer module using loose cuts on the residuals of the hits to the extrapolation. The sample of hits is tested looping over the hits inside the loop started in Step 1. This ends in a number of candidates, which are tested afterwards and are dropped if they fail the requirements. From the Θ_M of Step 1 the z corrections are done for the R-Φ hits. By forming a triangle with the coordinates of {Outer hit; Closer hit; Primary Vertex} the curvature and the track direction at the first and last point can be computed. From the R-Φ coordinates of the hit in the Closer layer an estimate is made for φ and a first track model is formed.

   At this stage the P_T is tested. Requiring a minimal P_T, two passes for this routine are performed. The first reconstructs harder tracks with $P_T > 500$ MeV/c and the second pass soft ones down to $P_T > 30$ MeV/c. A simple intersection of the Inner layer circle with the line connecting Outer and Closer gives a probable point on the Inner layer.

Step 3: This geometrical input defines all track parameters $\epsilon_{xy}, Z_P, \Theta, \varphi, \kappa(= 1/R)$ and the $R\Phi$ values in the layer cylinders which are used to make a new extrapolation

through all layers. This gives a list of hits with residuals of the track to the hit. Depending on the actual P_T a residual cut for the hits is calculated and the hits with the smallest residuals are selected, storing the sum of residuals for a later decision. The track is now tested if it still has a hit in each layer and the hits are checked if they are used twice. In the case of double usage the track with more associated hits or the smaller residual sum survives and the other candidate is killed by getting a bad quality flag. This can happen since the steps 1-3 are in a loop structure.

Step 4: From now on the track candidates are reconstructed and some last cuts and checks are done together with geometrical tunings. Again the Θ from the module centre of the Outer layer is used to make a z correction to the R-Φ hits. As no further z information is available yet, this is the best approach. From these corrected R-Φ coordinates the curvature and track directions are calculated, again using a triangle from Outer, Inner and Closer layer. The R-Φ hits are checked to be consistent with the z position. Since the z edges are known one can test, if all R-Φ modules are on the same z side or in a physically possible position, for a track from the primary vertex passing through all three modules: E.g. a track could not pass the very forward module in the Closer layer and come from the primary vertex simultaneously, see fig.4.4.

Step 5: The z-hit association is done (see next section), and the Θ and Z_P for the track parameters (4.3) can be computed.

Step 6: Using the associated z-hits the final z corrections to the R-Φ hits can be done and vice versa. A track fit gives the final track parameters and covariance matrix.

In Steps 1-4 the R-Φ association is performed, which defines the most important part of the procedure. The details of z-hit association are explained in the next section.

4.2.2 Association of z-Hits

All unassociated hits which come from the same module as the R-Φ hits in the corresponding Outer or Closer layer are collected for the association of z-hits. Most of the z-hits are not unique, because of the limitation of the readout electronics, where several z strips are related to one electronic channel. This means a hit corresponds to three, two or one z positions for the particle crossing the silicon wafer. All these z positions are treated as independent hits with different z values. The multiplexing in the Closer layer counts one or three hits, in the outer layer one or two hits are grouped together. The distance in z varies due to the changing pitch structure (see chapter 2) and is about 1.9-3.7 cm in the Closer and 2.7 cm in the Outer layer.

Two major possibilities after searching free z-hits can occur:

1. (a) one hit in one layer (Outer or Closer) or

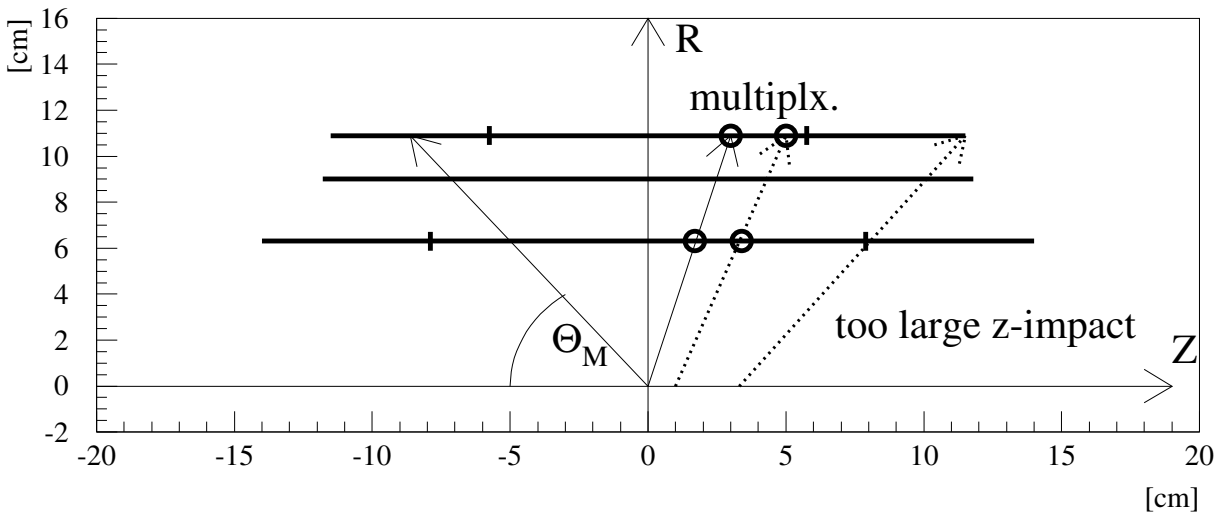

Figure 4.4: *The vertex detector in the R-z plane. On the left side the estimation of* Θ *by taking the module centre in z,* Θ_M *is shown. On the right side a case of multiplexing and a track with too large impact parameter in z are demonstrated. The last case can be avoided by checking for the module edges in z.*

(b) more than one hit in only one layer (Outer or Closer) was found

2. One or more hits in both Outer and Closer layer were found

The R-z situation of the vertex detector is illustrated in fig.4.4, showing the p-n flip boundaries of the Outer and Closer layer.

Case 1

If only one sensitive layer has free z-hits, then no hit association to the track is done. The Θ is computed from the primary vertex z-coordinate and the chosen z-hit but the error for the estimated Θ is taken from the $\Delta\Theta$ of the module z-edges; $\sigma(\Theta) = 10.5° - 13°$. For the case **1.a** the z-hit is unique but the full association as explained above is not reliable. If more than one hit in one layer is found (case**1.b**) the solution giving the Θ closest to the Θ_M of the module centre is taken. By selecting this solution it is required that not more than five free hits exist and the difference to Θ_M is $\Delta\Theta < 10°$.

Case 2

Finding hits in Outer and Closer layer allows an independent Θ determination. The distance of multiplexing for the Outer layer is larger than 2.6 cm and for the Closer layer larger than 1.9 cm. The Outer layer gives a multiplexing of 1 or 2, the Closer layer of 1 or 3. By running over all possible combinations these ambiguities should be

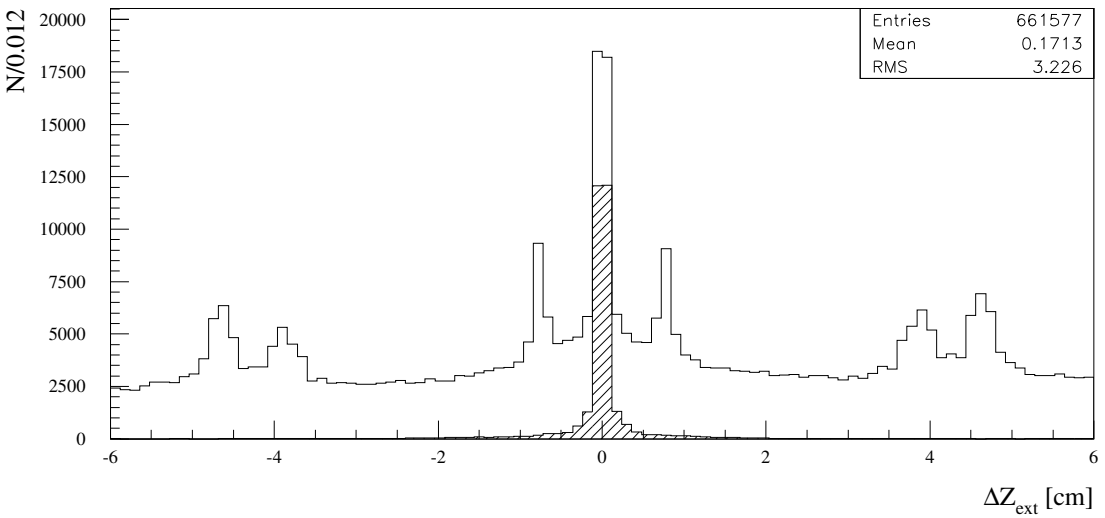

Figure 4.5: *The difference of the extrapolated z_{ext} to the primary vertex, when looping over all possible two z-hits solutions. The double peak structure caused by the multiplexing is visible. The filled histogram shows the selected solutions with the minimal z difference.*

solved, by requiring a minimal distance of the track to the primary vertex $\vec{P}_V$ in z:

$$z_P = -\frac{z_O - z_C}{\Delta S(O-C)} \cdot \Delta S(O - P_V) + z_O \ , \tag{4.5}$$

$$\Delta Z_{ext} = z_P - z_{PV} \ , \tag{4.6}$$

The variable (4.6) is shown in fig.4.5 where the effect of multiplexing is visible in the neighbouring peaks left and right of the peak at zero. For example, taking roughly $z(O)$=z_a=2.7 cm and z_b=1.9 cm for the multiplexing in the Outer and Closer layer together with ΔR=4.6cm and calculating in the R-z plane :

$$\Delta z = -R(O)/\Delta R/(z_a - z_b) + z(O) \approx 0.8\text{cm} \ , \tag{4.7}$$

with $R(Outer) = 10.9$ cm, explains the peaks at ± 0.8 cm, which repeat at larger values of ΔZ_{ext}. When choosing the combination with the minimal ΔZ_{ext} the neighbour peaks disappear. To get a trustworthy association the minimal solutions with $\Delta Z_{ext} < 0.2$ cm are taken. The track length between Outer and Closer $\Delta S(O-C)$ can be calculated from the x,y positions of the R-Φ hits and the track curvature $\kappa = 1/R$:

$$\sin(\alpha/2) = \frac{\sqrt{\Delta x^2 + \Delta y^2}}{2R} \ , \tag{4.8}$$
$$\Delta S(O-C) = R \cdot \alpha \cdot$$

Together with the z-hits the Θ value is given by:

$$\tan\Theta = \frac{\Delta S(O-C)}{z_O - z_C} \cdot \tag{4.9}$$

The z-hit association for VD tracks is summarised in table 4.1. The difference in data and Monte Carlo simulation for the B1 and B2 processing disappears in the B3 processing. Improved efficiency tables provide agreement between data and simulation concerning the z-hit association.

Table 4.1: *Summary statistics about z-hit association of VD tracks per event for several* DELPHI *processings of data and simulation.*

Sample	2 z-hits case 2	2 z-hits after cut	1 z-hit per lay.	>1 z-hit per lay.	No z-hits found	no z-hits assoc. to track
94B1 MC	0.88	0.75	0.01	0.06	0.05	0.25
94B3 MC	0.72	0.60	0.05	0.16	0.07	0.40
94C2 MC	0.77	0.60	0.06	0.13	0.03	0.40
94B2 data	0.76	0.60	0.03	0.14	0.07	0.40
94B3 data	0.75	0.60	0.03	0.14	0.08	0.40
94C1 data	0.80	0.60	0.03	0.11	0.05	0.40

4.2.3 Properties of the VD tracks

The Θ distribution of VD tracks with two z-hits in fig.4.6 shows the sensitive vertex detector z range and the blind TPC region at $\Theta = 90°$. This value is slightly shifted due to the displaced primary vertex in the DELPHI frame (z =-0.5 cm). The lack of tracking in this region is regained by the VD tracks. The corresponding distribution for VD tracks without z-hit association shows the four module structure, which comes from the p-n flipped module technique. From the φ distribution of the VD tracks in fig.4.6 it is clear that for high momentum many tracks going through TPC cracks are seen; (for high momentum tracks $\varphi \approx \Phi$). The periodic repetition of the Φ cracks every 60°=1.049 radians is visible. Monte Carlo simulation and measured data are presented in the same histograms and show slight differences in the geometrical efficiency and acceptance. The histograms have been normalised to the number of entries, therefor only differences in differential distributions are visible. The total efficiency differences between data and simulation are presented in table 4.2. Comparing the track parameters of the VD tracks after reconstruction and at simulation level in simulation samples checks the purity and resolution of the tracks. This was done with the TKREAS routine [48] which tests the tracks by comparing the track parameter using a χ^2. If a simulated track matches

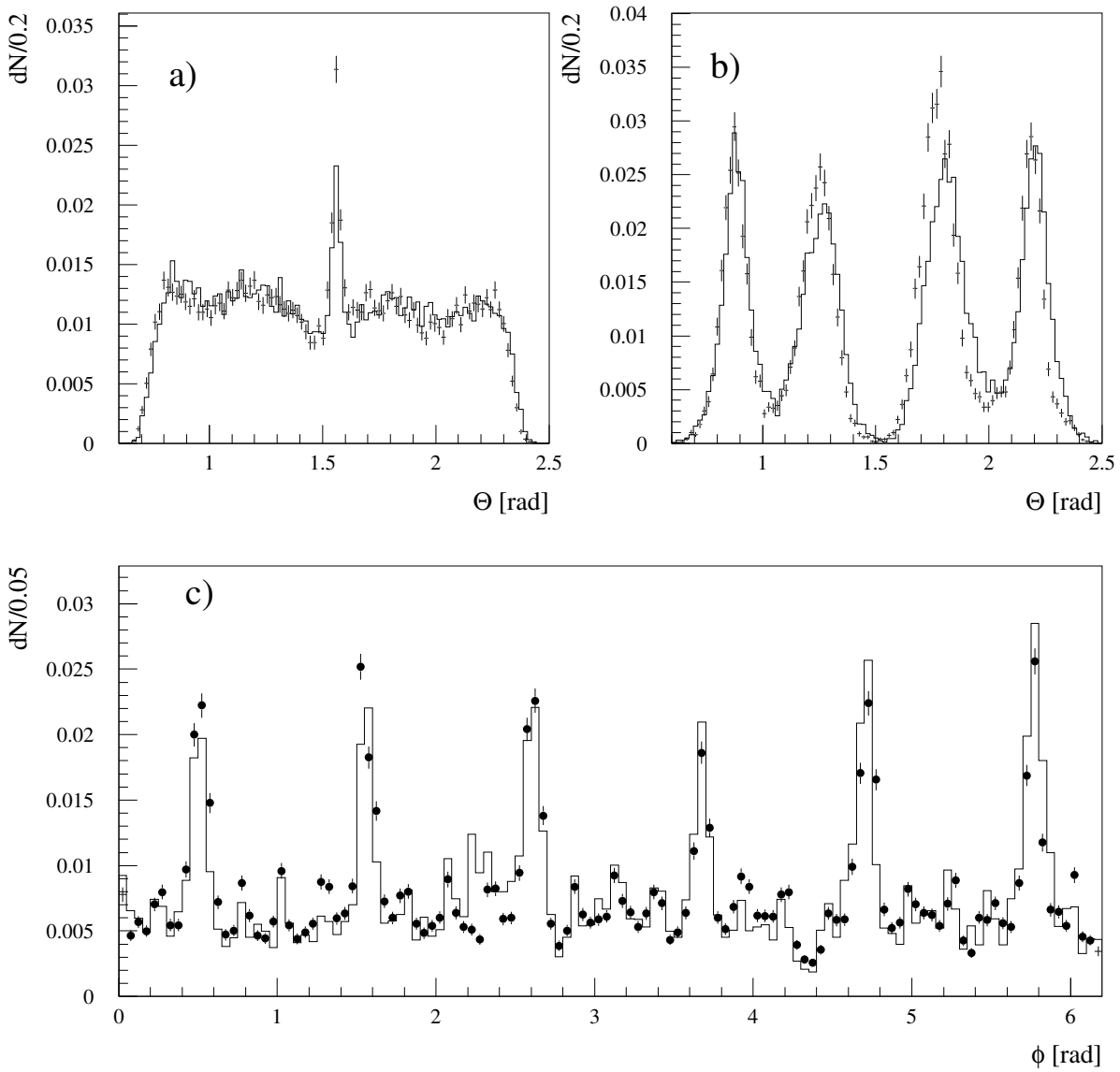

Figure 4.6: *The Θ and ϕ distributions of the VD tracks. Data are indicated by crosses and filled circles, histograms represent the Monte Carlo simulation. Part a) shows the Θ for VD tracks with two z-hits, part b) the distribution for tracks without z-hits, getting the Θ from the module middle in z. The ϕ distribution is given part c) for tracks with more than 1 GeV/c transverse momentum.*

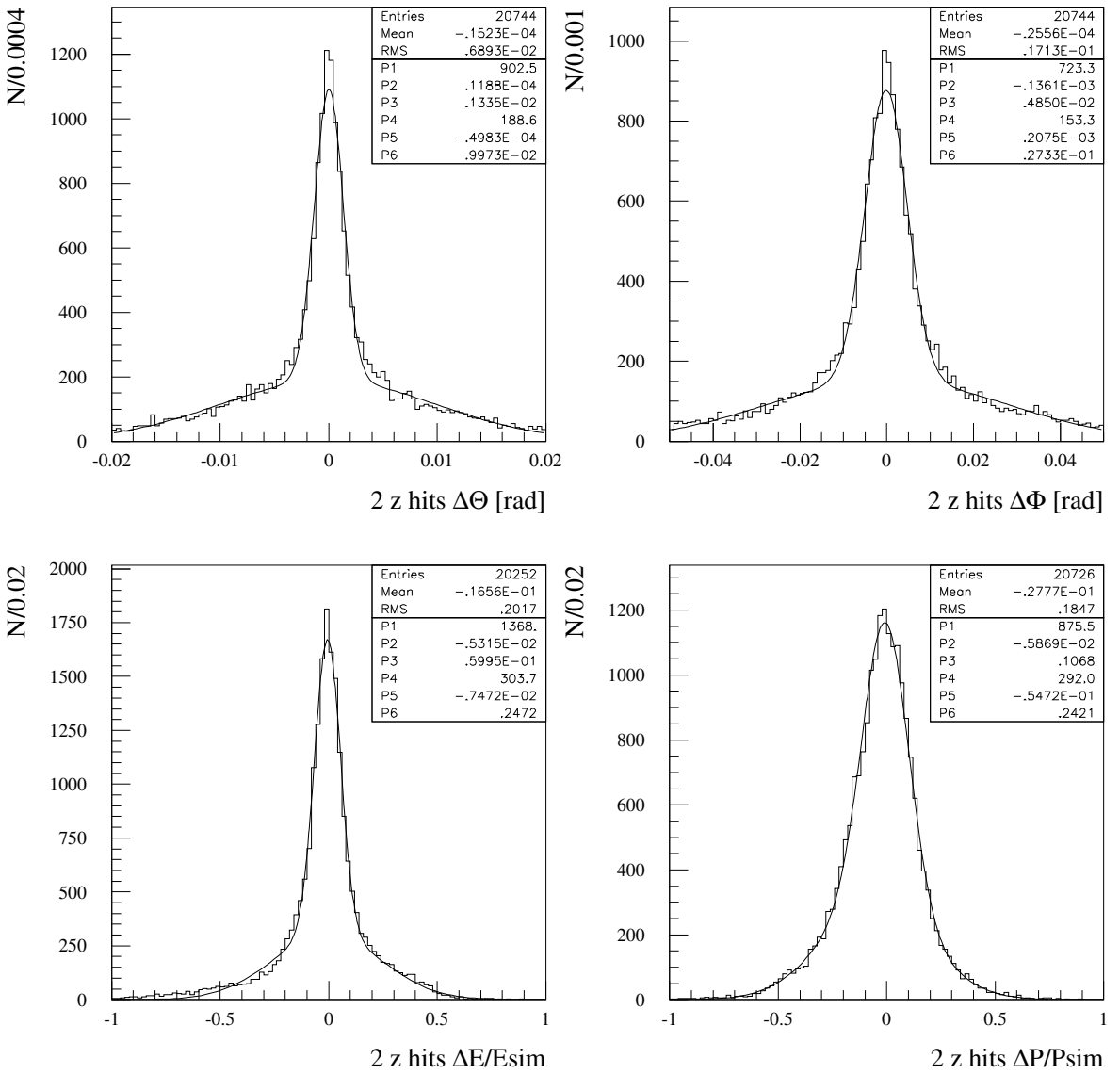

Figure 4.7: *The resolution of the VD tracks with two z hits for* Θ, ϕ, *energy and momentum compared to the simulation. The resolutions for VD tracks without z hits are similar.*

the reconstructed VD track in direction and momentum a link between simulation and reconstruction level is get. Due to the fine spatial resolution of the vertex detector a false hit destroys the whole comparison and the χ^2 value will blow up for the curvature or the Θ value. The tracks are found to get links for 80% of the two z hit tracks and 40% of the tracks without z hits. These numbers can also be interpreted as a purity for the reliability of the tracks. The resolutions in Θ, ϕ ,energy and momentum are shown in fig.4.7. The angular resolution is better than 10 mrad and the momentum resolution is about 10 to 25%. Both lead in an energy resolution of 6 to 20%. Looking at the transverse momentum $P_T^2 = p_x^2 + p_y^2$ of the VD tracks (fig. 4.8), it can be seen, that

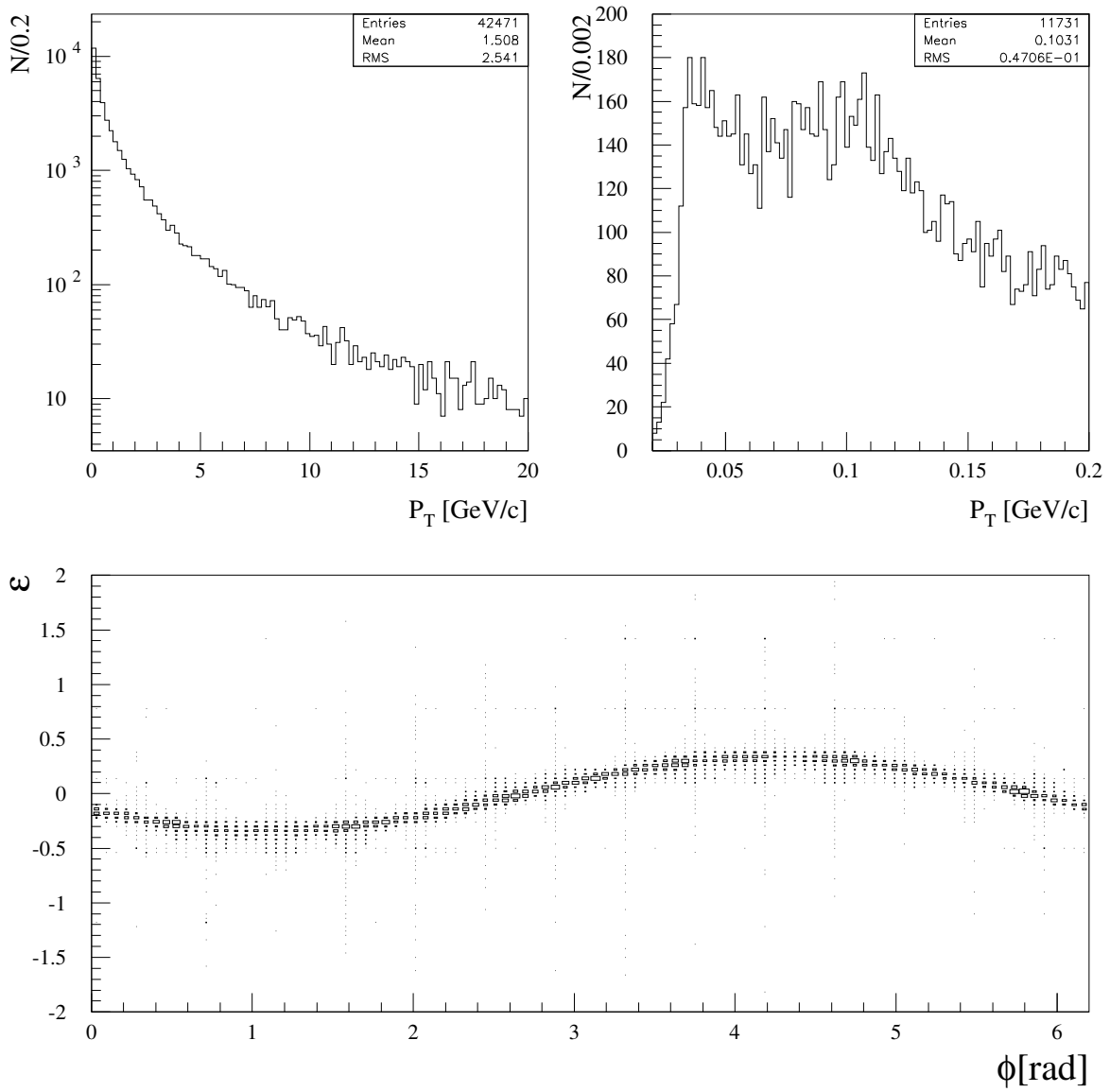

Figure 4.8: *Upper two histograms: Transversal momentum $P_T < 20 GeV/c$ and the low momentum range for $P_T < 200\ MeV/c$. The lower plot shows the impact parameter versus the track direction, which follows a sine curve.*

mostly low momentum tracks have been reconstructed besides doubtful high momentum tracks.

It is reasonable from the poor geometrical facilities of the small vertex detector diameter that tracks with large momentum have the biggest error on the momentum. The real possibility to reconstruct tracks down to 30 MeV/c is remarkable, this will be necessary for the analysis presented later. To check the reconstructed impact parameter distribution the correlation of φ to ϵ is tested. Taking the origin (0,0,0) as a reference point the φ vs ϵ should show the displaced primary vertex in the x-y plane by a sine-like behaviour. This is confirmed in fig.4.8. The distribution of track parameters in Monte Carlo simulation show the same behaviour but with a different efficiency.

As summarised in table 4.2, more tracks per event have been found in the data than in the Monte Carlo simulation. This shows that the vertex detector efficiency and other tracking simulations are not in perfect agreement. Processings agree better and better, since much work was invested in efficiency tables and alignment. In the new processing 94C1 much less VD tracks have been found than before. This is due to an improved track extrapolation for vertex detector hit association, better alignment and an improved track finding from Inner Detector and vertex detector TEs (IDVD tracking). This partly solves the TPC crack and low energy efficiency problem and could profit from the algorithms developed here.

Table 4.2: *Average number of VD tracks and the resulting track type, per event for different processings, simulation (MC) and data.*

processing	VD tracks / event	2 z-hits assoc.	no z-hit assoc.
MC 94 B1	1.53	75%	25%
MC 94 B3	1.13	60%	40%
MC 94 C2	0.45	58%	32%
data 94 B2	1.83	60%	40%
data 94 B3	1.63	60%	40%
data 94 C1	0.60	51%	49%

4.2.4 Applications of VD Tracks

Another goal of the event reconstruction is the identification of secondary hadronic interactions. A hadronic vertex at the Inner Detector or the TPC wall will end with one charged track stopping in the wall and a bunch of other tracks starting from the wall. Some energy loss due to inelastic interactions is expected, that the energy sum does not need to balance. After the identification of the intersection point from the

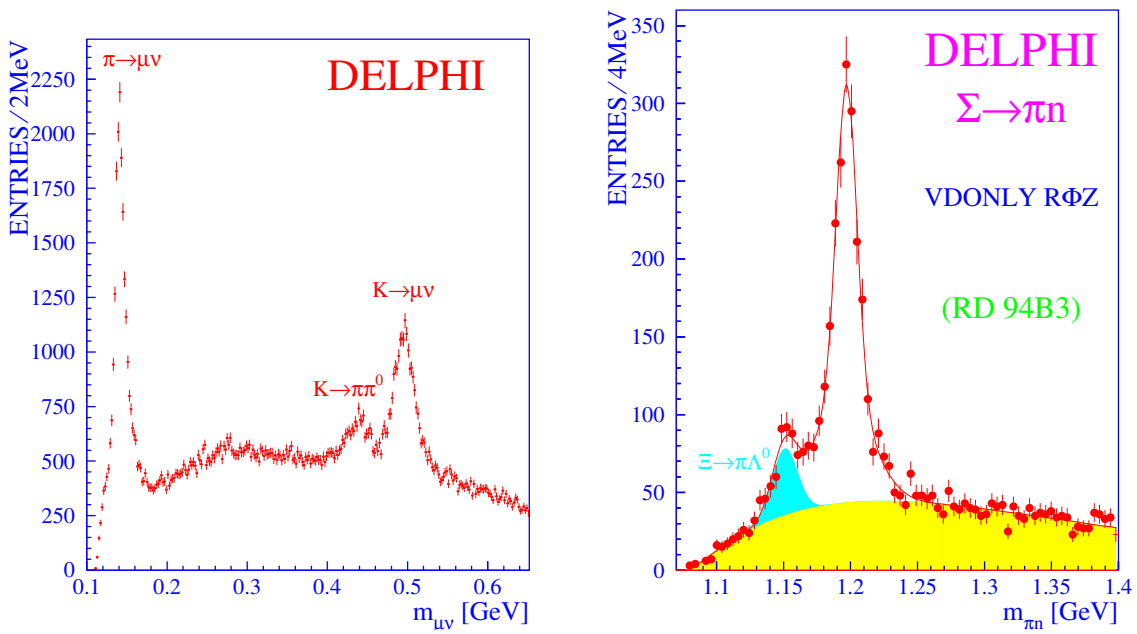

Figure 4.9: *The invariant masses of kink candidates. On the left side shown for VD tracks measured with z and Θ. The mass peaks from $\pi^{\pm}$ and $K^{\pm} \to \pi\pi^0$ are reflections from the assumed decay hypothesis. Right side shows the Σ signal measured with this technique, with a reflection from $\Xi \to \pi^- \lambda^0$ decays at 1.15 GeV. Pictures by courtesy of C. Weiser.*

outgoing particles, a loop over all other tracks with a small tracklength is done to check whether they match to the hadronic vertex in R-Φ and z. From their small tracklength VD tracks of higher energies are ideal candidates for incoming tracks of these hadronic interactions. A lot of VD tracks match to hadronic vertices and in the short DST production section (3.5) these matches are identified. The identification of hadronic vertices allows a more complete energy reconstruction. Another source of incomplete tracks are the so called kinked tracks. One charged track loses energy due to interaction with detector material or a decay into one charged and one neutral particle:

$$X^{\pm} \to Y^{\pm} + \text{neutrals} \ .$$

This can lead to the identification of decaying particles with a decay length of more than 11 cm (e.g. $\Sigma^{\pm} \to \mathrm{n}\pi^{\pm}, \Xi^- \to \Lambda\pi^-, \mathrm{K}^{\pm}/\pi^{\pm} \to \mu^{\pm}\nu_{\mu}$). To reconstruct decays from this configuration, an intersection point outside any detector material is required. By computing the invariant mass from this object several candidates can be seen [49]. In this approach the four momenta of one incoming and one outgoing track are measured and hence the missing momentum of the neutral particle for a decay hypothesis. In fig. 4.9 the $K^{\pm}$ decay into $\mu\nu$ was assumed, the other peak structures fit to the indicated decays and are slightly shifted, because of the mass assumption. Using this technique a nice $\Sigma^- \to \pi n$ signal can be achieved (fig.4.9), see [49] for further information.

4.3 dE/dx Measurement with the Vertex Detector

As in the Time Projection Chamber, a charged particle has a typical ionization energy loss $dE/dx \cdot \Delta x$ in the vertex detector. Normally the Vertex Detector is used for spatial measurements only, but the deposited signal in the silicon tracker also gives signal height information. The characteristic coefficient for a particle passing through matter is:

$$\kappa = \frac{\overline{\Delta}}{W_{max}}, \tag{4.10}$$

where $\overline{\Delta}$ is the mean energy loss and W_{max} stands for the maximal possible energy transfer (i.e. the total possible deposit of the particle's energy; see [39] for further details). For the case $\kappa < 10$ the material is called a thin absorber; for $\kappa > 1$ the ionization signal distribution is still close to a Gaussian distribution. A Landau distribution of the signal is expected taken $\kappa \to 0$ or $W_{max} \to \infty$, analogous to a negligible decrease of the velocity of the passing particle. This is indeed the case for high energy tracks passing through the silicon wafer of the Vertex Detector. Their energy loss is negligible low compared to their initial energy. A Landau function is mathematically defined as [39][50]:

$$\phi(x) = \frac{1}{2\pi i} \int_{C-i\infty}^{C+i\infty} \exp(xs + s\ln s)\mathrm{d}s \ ; \text{with C } \geq 0 \ . \tag{4.11}$$

The curve of this formula is plotted in fig.4.3. The function shows a large tail to higher values, which makes the estimation of the interesting peak position difficult. The maximum value for this function is at x = -0.222783.

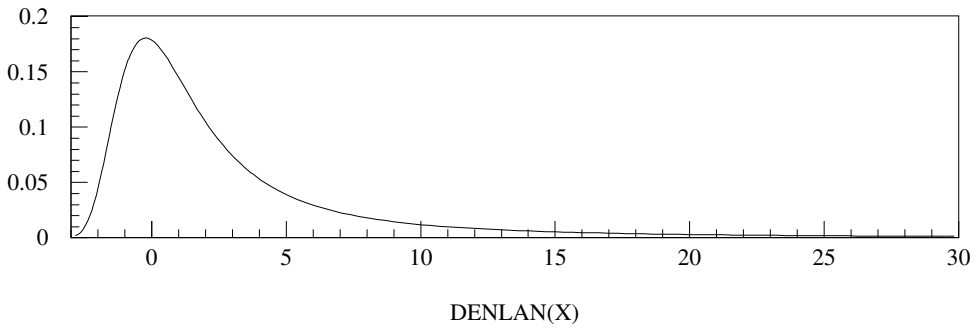

Figure 4.10: *A normalised Landau function, from [50]. In the practice a width and a shift of the peak position are needed to describe the data.*

For a track passing three layers in the vertex detector, this peak value can be estimated by a maximum likelihood fit from the signal values of the hits. In order to extract more information about the measured signal, the normal signal value of the two highest strips in a cluster (see section 4.1.3) is extended by summing up all strip signals in a cluster.

$$p = \sum_{\text{cluster}} p_j \tag{4.12}$$

Maximum Likelihood Fit

Taking the pulse height p_i from the total cluster (eq. (4.12)) and defining the variable

$$y_i = p_i - x - 0.222783 \ , \tag{4.13}$$

the likelihood for the wanted peak position would be :

$$\mathcal{L} = \prod_i \phi(y_i) \ . \tag{4.14}$$

This is maximal for a given set of $\{p_i\}$, when the argument is $y = -0.222783$, implying that the ideal value of x gives the peak position p_i of the hit. Continuing with the maximum (log) likelihood equation:

$$\frac{\partial \ln \mathcal{L}}{\partial x} = \frac{\partial \sum_i \ln \phi(y_i)}{\partial x} = 0 \ , \tag{4.15}$$

one deals with a sum of $\ln \phi(y_i)$. With the derivative of the logarithm and its argument $\partial\phi(x)/\partial x = \phi'$ the identity:

$$\sum_i \frac{\phi'(y_i)}{\phi(y_i)} = 0 \ . \tag{4.16}$$

can be used. By specifying the zero of expression (4.16) a sort of maximum likelihood fit is done, in the sense that the peak position for a given set of pulse values $\{p_i\}$ is found. The more hits are collected, the better the result will be, i.e. the resolution of this method will improve.

Path Length Correction

Other sources of biased values and smearing are different response and path length of the tracks when passing through the material. Tracks passing in the forward direction are depositing more charge in the material than tracks passing perpendicularly at $\Theta = 90°$.

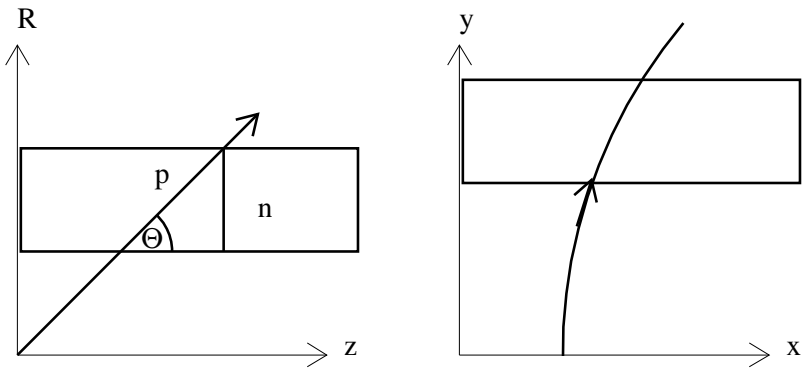

Figure 4.11: *Different path length of tracks depending on the position and curvature of the track. On the left the Θ dependence (in the R-z plane), on the right the influence of the curvature (in R-Φ) is shown.*

Assuming the signal to be proportional to the path length p a factor of $\sin\Theta$ illustrates this effect: $n = \sin\Theta p$ (see fig.4.11). Here n is the normalised path length and p is the physical value.

A second contribution comes from tracks with large curvature passing through the vertex detector modules at an angle in the R-Φ plane. The magnetic field $\vec{B_z}$ makes their path curved and the length in R-Φ is larger. By extrapolating the track from the perigee parameters (4.3) up to the radius of the module the exact track length in the silicon wafer can be computed and this longer path length for Θ and (κ, φ) can be corrected.

4.3.1 Module Calibration

The last source of broadening the signal are the different response values of different vertex detector modules. Because of individual differences in material and electronics this differs from module to module and a collection of pulse signal is needed in every module to correct this. For each module a sample of tracks is taken and the corresponding signal height is stored. This gives the different distributions in fig. 4.12. The collected distribution in a module is a Landau function shifted by the specific module response, folded with a Gaussian distribution due to a finite electronical resolution. To calibrate the modules a Landau function (with a parameter for the width folded with a Gaussian distribution) is fitted to the collected signal distribution. This function can be written as:

$$f(x; N, a, b, \sigma) = N \int_{x-5\sigma}^{x+5\sigma} \phi(\frac{x-a}{b^2}) \cdot e^{-\frac{\mu^2}{2\sigma^2}} \mathrm{d}\mu \ , \tag{4.17}$$

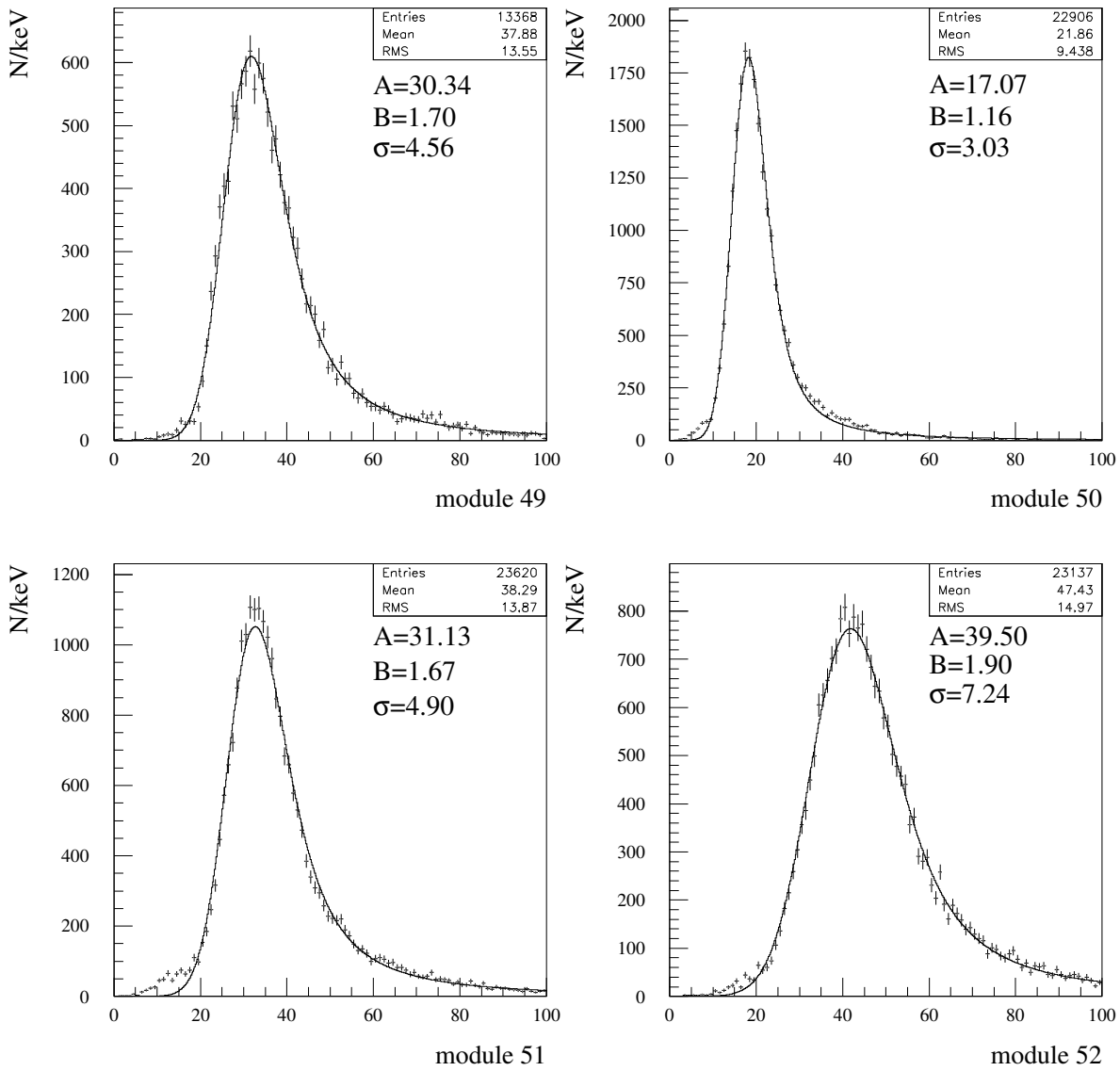

Figure 4.12: *Pulse height distributions of different modules (crosses) , shown together with the fitted curve of formula (4.17) (solid line); peak position (A), widths (B) and Gaussian smearing (σ) are also presented. The signal value is given in keV. Most interesting for the purpose of calibration is a good fit in the peak region. This is satisfied by the theoretical fit compared to the measured distribution, also when the shapes might differ in the tails.*

with N a normalisation factor, a the wanted signal height, b the Landau width and σ for the Gaussian smearing. By fitting this function to the measured distributions the calibration of all 576 modules of the vertex detector 1994–95 is performed in an automatic procedure. The formula (4.17) does not give a perfect χ^2 for the fit but the main aim of this computation is to determine the module specific Landau peak position. The result is satisfactory even when the theoretical function is sometimes problematic in the tails.

4.3.2 dE/dx Resolution

To calculate the dE/dx of a track in the vertex detector the associated hits are taken and the signal values are kept. After the path length correction and signal calibration, the maximum likelihood fit of eq.(4.16) is applied and the Landau peak position can be calculated. In this computation the mean value of the $R\Phi$ and z-hits of the same module is taken, since for the vertex detector 1994–95 they use the same silicon wafer and show the same Landau fluctuations, the difference just being the different electronics. For tracks with more than two hits the resulting dE/dx is shown in fig. 4.13, for the whole possible momentum range of hadronic Z^0-decays.

In this distribution several bands are visible, which allow a separation or particle identification. For the high momentum range the method is not competitive with the dE/dx measurement of the Time Projection Chamber. This comes from the worse resolution and the low relativistic rise of the dE/dx in silicon after the minimum. The position of the saturation of this rise depends on the density like [38]:

$$\beta\gamma \sim 1/\sqrt{\rho}\ . \tag{4.18}$$

The density corrections, see formula (3.8) damping the relativistic rise [20]:

$$\delta = \ln \frac{\hbar\sqrt{Z\rho e^2/\epsilon_0 \epsilon m_e}}{I} + \ln\beta\gamma - 1, \tag{4.19}$$

go with the density and dielectric constant of the medium. For gases the excess of the relativistic rise compared with the minimum can be up to 50% while for solids only 10% are expected. This 10% difference is compared to the resolution of the measurement. In the vertex detector only up to 6 points can be used while in the TPC a maximum of 192 wires give a signal. This explains the difference in the dE/dx resolution.

For high momentum tracks $p > 1.3$ GeV/c all particles behave as a minimal ionising particle (**mip**) and the resolution of the dE/dx measurement can be estimated. The dE/dx resolution is shown in fig. 4.14 for the case of 1-6 $R\Phi$-hits. From a fit of a Gaussian distribution to these histograms the Gaussian sigma is taken for the dE/dx resolution. For an exact calibration and good Landau fit of the signals the mean values

should be at 1. The histograms with one and two hits per track show that the computation is biased to higher values. Here the max. likelihood fit is suffering from the Landau tails. When using three hits, the method works well and a resolution of 15% can be achieved. The number of entries in the histogram show that the big majority of tracks has more than two hits associated, therefore the procedure can be applied to most tracks and the efficiency of the method is the efficiency of vertex detector hit association. The resolution depending on the number of hits and the corresponding fraction of tracks which have these hits associated are given in table 4.3.

The VD tracks have by definition at least three hits in the vertex detector and this guarantees a reliable dE/dx measurement. They allow one to explore the low momentum part of fig.4.13 with a particle identification below 100 MeV/c.

Table 4.3: *Resolution and efficiencies for the dE/dx calculation with the vertex detector 94 for the 94C* DELPHI *processing, sorted by the number of associated vertex detector hits. 64% of all tracks have more than two hits and allow a good dE/dx measurement.*

VD hits	σ(dE/dx)	frac. of tracks
1	0.28	14%
2	0.19	24%
3	0.15	46 %
4	0.13	8%
5	0.12	4%
6	0.11	4%
>2	$\leq$0.15	62%

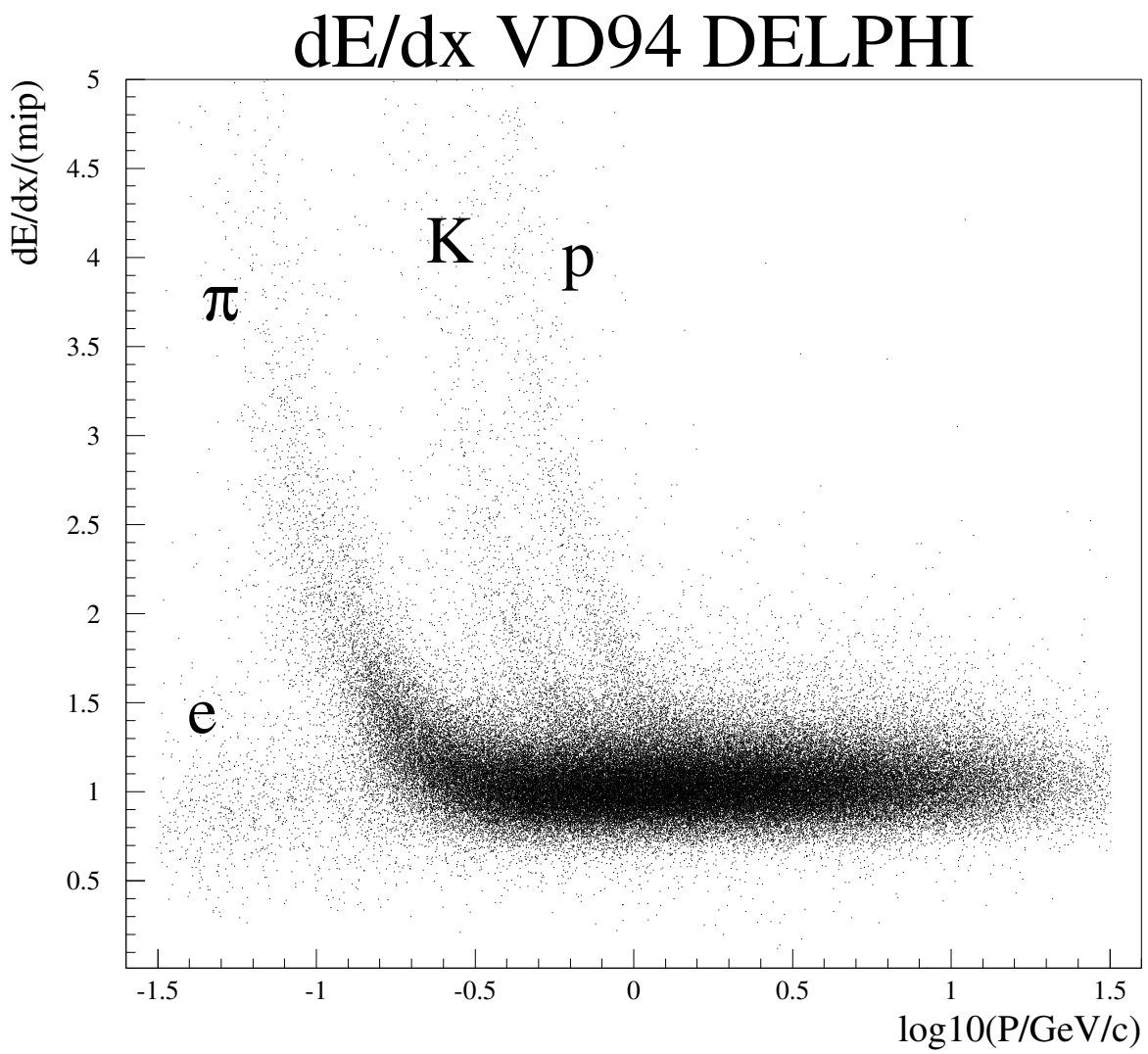

Figure 4.13: *The vertex detector detector dE/dx with three hits and more for the whole momentum range, measured with the 94 vertex detector. Clearly visible are the $e^{\pm}$,$\pi^{\pm}$,Kaon and proton bands. The VD tracks cover the momentum range below 100 MeV/c and show a nice electron/π separation.*

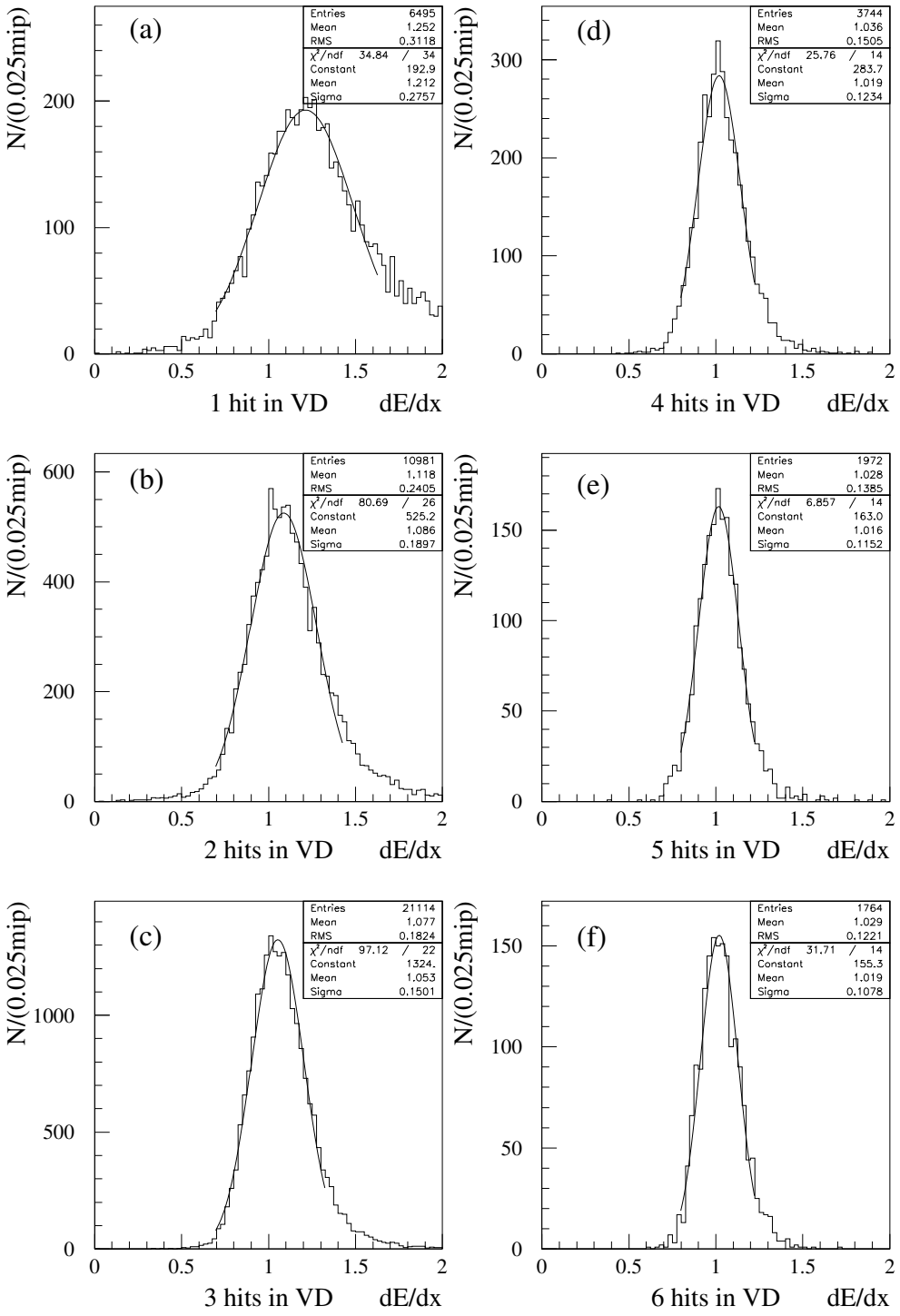

Figure 4.14: *Vertex Detector dE/dx resolution for minimal ionising particles. a) 1 hit b) 2 hits up to f) 6 hits, fitted with a Gaussian distribution. If the calibration and Landau max. likelihood fit work well, the mean should be 1 , the Gaussian sigmas give an estimate for the resolution of the method.*

5

Reconstruction Tools

To reconstruct the B* Dalitz decay final state B e^+e^-one B meson and one electron positron (Dalitz) pair are needed. A pure reconstruction of these two components is fundamental for the analysis in the last chapter. In the following the Dalitz pair identification is shown. Next a technique to enrich a sample out of $q\overline{q}$ events with $b\overline{b}$ events is introduced. Finally the B meson reconstruction in an inclusive fashion is presented. This method yields in an enrichment of B decay particles.

5.1 Reconstruction of Dalitz Pairs

A loop over pairs of two opposite charged tracks reconstructs the electron positron pairs with small invariant masses. Coming from the internal conversion of the photon at the primary vertex, the pairs are expected to have the following characteristics:

- The tracks are electrons.
- Both tracks come from the primary vertex.
- The tracks have a small opening angle.

If there is a dE/dx measurement from the TPC, it must be consistent with the electron hypothesis. This can be evaluated by comparing the expectation of the dE/dx for an electron and the measured value together with the error of the measurement in a χ^2 calculation :

$$\chi^2 = \frac{(dE/dx_{th} - dE/dx_{meas})^2}{\sigma^2_{dE/dx}} \tag{5.1}$$

and computing a probability from this: $Pr(e^{\pm})$. To enhance electrons, this probability is required to be greater than 1%. If two tracks in the TPC are very close in the z

component ($\leq$ 2cm), their signals at the sense wires cannot be separated well. This is the case for Dalitz pairs. They have an opening angle of nearly zero and are only separated in the R-Φ plane by the magnetic field. If both tracks differ in the track length ΔS the resulting Θ is different again, according to $\tan\Theta = \Delta S/\Delta z$. This separation is only possible after some cm of common track length, therefore at the beginning the tracks are not separated. For this reason tracks with no uniquely measurable TPC dE/dx are taken as well. Additionally the measured dE/dx of the vertex detector for VD tracks is required to be less than 1.5, this is a loose cut for electrons, as can be seen in fig.4.13, it separates pions and electrons in the low momentum region.

For the VD tracks a track fit is applied using the electron mass for the dE/dx correction, which is very different in the low momentum region for pions and electrons, as can be seen fig.4.13. This is necessary since the VD tracks go down to this momentum region of interest where the energy loss corrections become large.

To select tracks from the primary vertex, only candidates are accepted which have at least one measured point in the vertex detector. Additionally the impact parameter to the primary vertex in R-Φ has to be less than 0.3 cm. To have the best possible computed invariant mass and a final test on the primary vertex hypothesis the pair is required to form a vertex compatible with the event primary vertex by using a fit procedure [51]. The pair is accepted as a candidate when the resulting χ^2 is less than 40. The opening angle is required to be $|\cos\alpha| > 0.95$. If several combinations are still left after these cuts, the combination with the smallest invariant mass:

$$q^2 = (E_{e^+} + E_{e^-})^2 - (\vec{p}_{e^+} + \vec{p}_{e^-})^2 \tag{5.2}$$

is taken and each track can only be used for one combination.

From the used tracks for these combination the type of Dalitz photon can be classified. Three classes of Dalitz pairs are used for further investigations and marked with a so called `PXPHOT` code [52], specifying the nature of the tracks used:

- A conventional/TPC track together with a conventional/TPC track (code=–27)
- A combination of a TPC track together with a VD track (code=–26)
- VD track together with a VD track (code=–25)

The three classes are discussed in the following. The by far most important source of 'Dalitz pairs' is the π_0 Dalitz decay. Taking the π_0 production cross section [53] together with the ratio $BR(\pi^0 \to \gamma e^+ e^-) \approx 1\%$ one expects about 0.1 Dalitz decays per event. These pairs serve to judge the quality of the Dalitz pair reconstruction.

Class: Code=–27

The dE/dx measured in the TPC should agree with an electron hypothesis for the tracks measured in the TPC. The measured ionization and the computed probability

are shown in fig.5.1. It is clearly visible that still some background is left, because the electron and pion band overlap at $p \approx 150$ MeV/c. Additionally the errors are large for tracks measured with only a few wires, this is easily possible for low momentum tracks since they do not cross the complete TPC. A small rise in the probability distribution is caused by this, although a spike at low probabilities was cut out. Thus a small pion background is left, which cannot be reduced because the low momentum region is the most interesting for the present analysis.

The q^2 spectrum of the code=–27 pairs are shown in fig.5.2 together with the momentum distribution of the reconstructed photon and the momentum of the used tracks. The hatched histogram refers to pairs where none of the tracks has a measured TPC dE/dx. The q^2 spectrum expected is the curve in fig.2.8, peaking at low q^2 values. The q^2 distribution for pairs with no measured TPC dE/dx show a high amount of background in the full q^2 region. Depending on the analysis the purity of the photons can be increased if the q^2 value is cut or the TPC dE/dx measurement is required.

The momentum distributions of these –27 photons go only down to nearly 300 MeV in the momentum region, according to the momentum of the tracks they are made from, which end at 150 MeV/c. Any further cuts on the vertex detector dE/dx will not help to improve the electron purity since the momentum of the –27 pairs lie in the saturation

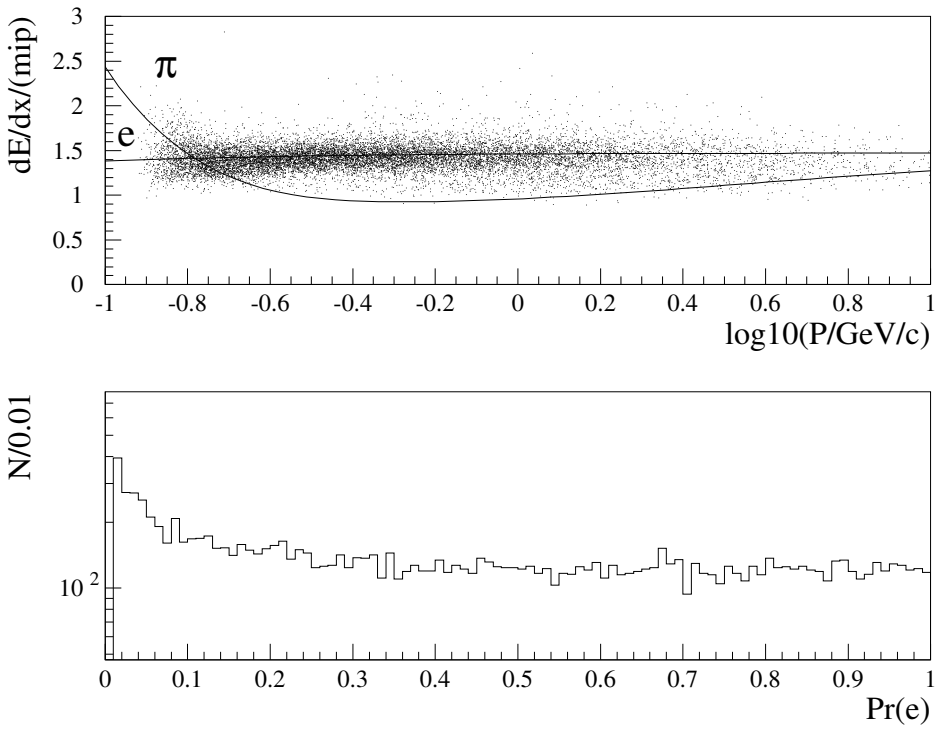

Figure 5.1: *The measured dE/dx of the tracks forming the Dalitz pairs, together with $e^{\pm}$ and $\pi^{\pm}$ expectation (upper plot). The corresponding probability distribution for the electron hypothesis is shown in the lower plot.*

region of the vertex detector dE/dx bands and cannot be separated, i.e. all particles have a dE/dx$\approx$ 1.

Class: Code=–26

These pairs contain one conventional track and one VD track. The electron probability of the TPC track shows the same distribution as in fig.5.1. The q^2 spectrum and the momentum of the photon and the tracks are shown in fig.5.3. Again a conventional track without measured TPC dE/dx is a source of background. If the TPC dE/dx is not measured the track is mostly an IDVD track, which means it has no reconstructed TPC TEs and is only built in the vertex detector and the Inner Detector. In contrast to the Dalitz pairs of type –27 which contain mostly TPC measured tracks, even when the TPC dE/dx is not measured. For IDVD tracks only the vertex detector dE/dx gives a separation in the low momentum region. Above 100 MeV/c one cannot distinguish between electron and pions. Again the purity of these tracks can be altered by requiring small q^2 values or a measured TPC dE/dx. As can be seen in the momentum spectrum in fig.5.3 the vertex detector dE/dx requirement of 1.5 is useful since the tracks are enhanced in the low momentum ($-1.5 < \log_{10}(p) < -1.$) region. Applying a harder cut on the VD dE/dx is senseless, according to the resolution of 15% this will not improve the separation.

Class: Code=–25

These pairs contain two VD tracks. Since the VD dE/dx can only give a veto against low energy pion background, the facilities for improving the electron purity are limited due to the broad vertex detector dE/dx resolution. The resulting q^2 spectrum and the energy distribution of the photons and the used tracks, show that these type of Dalitz pairs lie mostly in the low energy region. The resulting photon energy is low since both tracks are made of VD tracks which are mostly low momentum tracks.

Together with the code=–26 pairs they allow one to measure the low momentum region of Dalitz pairs, although they are numerically the minor class of the Dalitz pairs.

5.1.1 Simulation Test

The large amount of available π^0 decays in multihadronic events is a good test ground for efficiency and purity of the Dalitz photon reconstructions. The four momentum vectors of tracks can be compared after reconstruction with Monte Carlo simulation level. Picking up the final electron positron pair on generator level and the corresponding tracks on the Monte Carlo simulation gives the momentum vector of the Dalitz photon.

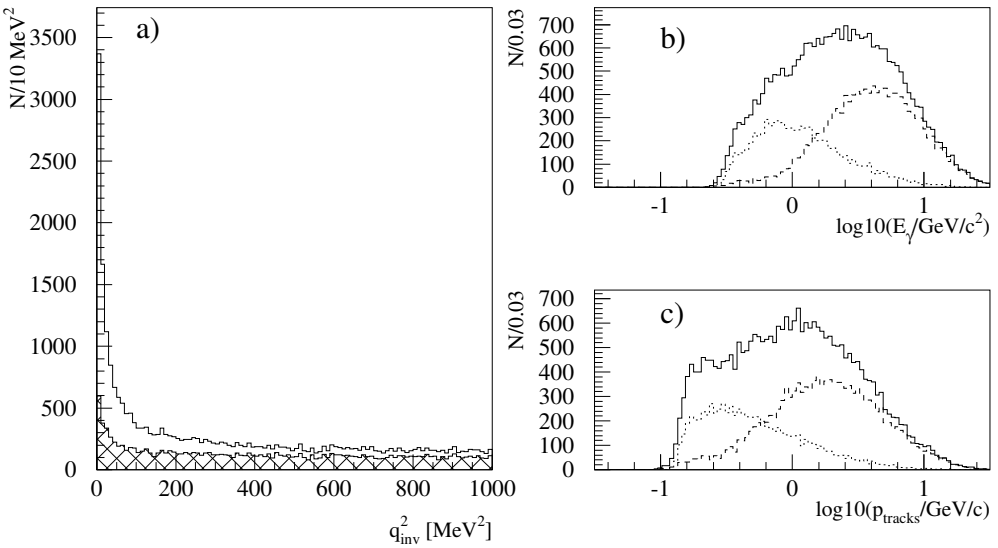

Figure 5.2: *a) The q^2 spectrum for Dalitz pairs of code=–27 (two TPC tracks); solid histogram : all pairs , hatched histogram : pairs of this class with no measured TPC dE/dx. b) The photon energies of –27 photons; solid line : all pairs, broken line : both tracks without TPC dE/dx measured, dotted line : both tracks with measured TPC dE/dx. c) The track's momentum; solid line : all tracks, broken line : no TPC dE/dx measured, dotted line : both TPC dE/dx measured.*

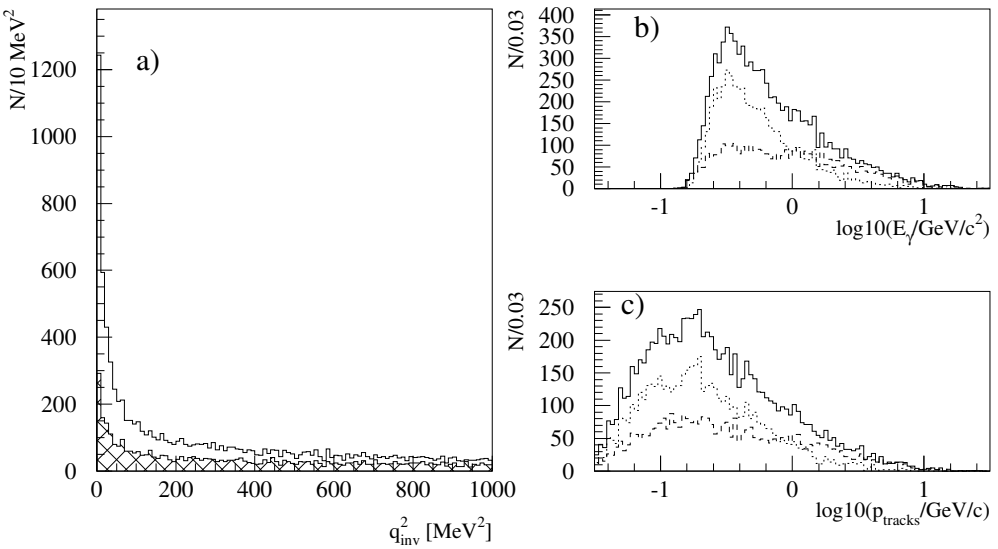

Figure 5.3: *a) The q^2 spectrum for Dalitz pairs of code=–26 (TPC track + VD track); solid histogram : all pairs , hatched histogram : pairs where the TPC track has no measured TPC dE/dx. b) The energies of –26 photons; solid line : all pairs, broken line : the TPC track without TPC dE/dx measured, dotted line : TPC track with measured TPC dE/dx. c) The track's momentum; solid : all tracks, broken line : TPC track without TPC dE/dx measured, dotted line : TPC track with TPC dE/dx measured.*

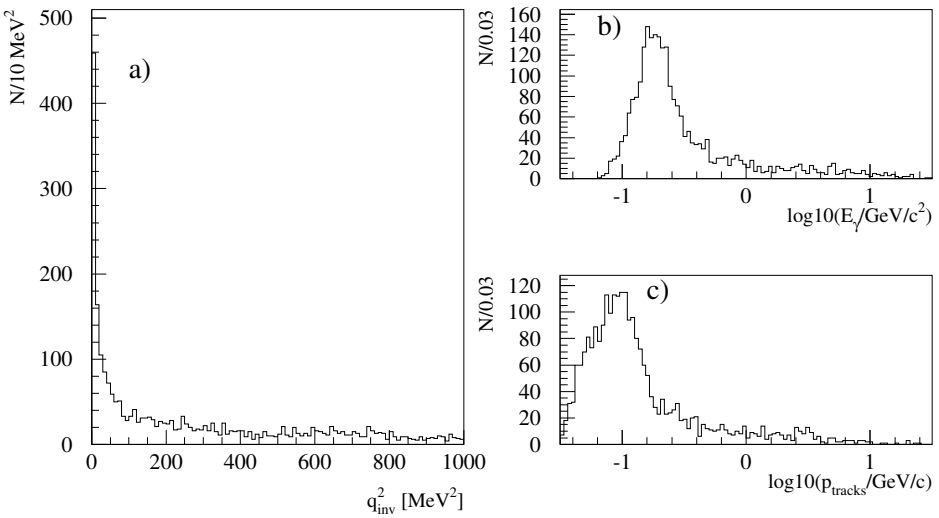

Figure 5.4: *a) The q^2 spectrum for code=–25 pairs (two VD tracks). b) The energy spectrum of the photon. c) The momentum spectrum of the tracks.*

The vector of the reconstructed Dalitz pairs can now be compared using a χ^2:

$$\chi^2 = \frac{(E_g - E_r)^2}{\sigma_E^2 E_g^2} + \frac{(\theta_g - \theta_r)^2}{\sigma_\theta^2} + \frac{(\phi_g - \phi_r)^2}{\sigma_\phi^2}, \tag{5.3}$$

by comparing the measured angles and energies of the simulation (g) and reconstruction (r). The aim is to match reconstruction and simulation level from the used errors and determine finally an efficiency and a purity. By assuming big errors (σ) all vectors can be matched and the errors can be estimated from a Gaussian fit to the distributions of $\Delta E, \Delta\theta, \Delta\phi$, after an iteration. The parameters in (5.3) are chosen to form a quality estimation for the whole Dalitz pair. The two tracks can differ very much in momentum and therefore the energy or momentum error of the single track might be dominated by multiple scattering for low momentum or geometry for a high momentum track. The three parameters are shown in fig.5.5. The background and efficiency of the Dalitz pair selection can be calculated from comparison with simulation. Different requirements on small q^2 values and measured dE/dx allow one to optimise the purity of the photons for the specific analysis, depending on the strength of the signal. The action of the cuts is documented in table 5.1. Taking the initial numbers of 48739 generated and 19550 measured Dalitz pairs together with 9551 true Dalitz pairs would give an overall efficiency of 0.196 and a purity of 0.488. The energy dependence of the efficiency is in fact much more important for the specific process which is analysed. For three choices of cuts (i-iii) the efficiency and purity energy dependence is shown in fig.5.6 The cuts have been:

i) $q^2 < 2 \cdot 10^{-4}(\mathrm{GeV})^2$ for all types, $|\cos\theta_T| < 0.7$

Table 5.1: *Cuts on Dalitz pairs: The decrease of signal and background applying cuts on the q^2 value and dE/dx are demonstrated. The column 'frac.' gives the fraction of the initial number of signal or background photons. Hard cuts ($\star$) can reduce the background to a few percent, but also the remaining signal rate is reduced to 30% or lower compared to the incident sample.*

	type	sig.	frac.	backg.	frac.	$q^2/(\mathrm{GeV})^2 <$	TPC dE/dx
	–27	6570	1	8171	1	10^{-3}	none
	–27	5936	0.90	4413	0.54	$5 \cdot 10^{-4}$	none
(i)	–27	5018	0.76	1969	0.24	$2 \cdot 10^{-4}$	none
	–27	4326	0.66	1102	0.13	$1 \cdot 10^{-4}$	none
	–27	5609	0.85	3375	0.41	10^{-3}	one good
	–27	5069	0.77	1856	0.23	$5 \cdot 10^{-4}$	one good
(ii)	–27	4316	0.65	909	0.11	$2 \cdot 10^{-4}$	one good
	–27	3747	0.57	551	0.07	$1 \cdot 10^{-4}$	one good
(iii)	–27	3534	0.54	1000	0.12	10^{-3}	two good
	–27	3204	0.49	607	0.07	$5 \cdot 10^{-4}$	two good
	–27	2743	0.41	351	0.04	$2 \cdot 10^{-4}$	two good
$\star$	–27	2401	0.36	239	0.03	$1 \cdot 10^{-4}$	two good
	–26	2582	1	1425	1	10^{-3}	none
	–26	2308	0.89	851	0.60	$5 \cdot 10^{-4}$	none
(i)	–26	1918	0.74	428	0.30	$2 \cdot 10^{-4}$	none
	–26	1587	0.61	256	0.18	$1 \cdot 10^{-4}$	none
(iii)	–26	1987	0.77	600	0.42	10^{-3}	conv. good
	–26	1780	0.69	354	0.25	$5 \cdot 10^{-4}$	conv. good
(ii)	–26	1479	0.57	180	0.13	$2 \cdot 10^{-4}$	conv. good
$\star$	–26	1219	0.18	114	0.08	$1 \cdot 10^{-4}$	conv. good
(iii)	–25	399	1	403	1	10^{-3}	none
	–25	377	0.94	241	0.60	$5 \cdot 10^{-4}$	none
(i,ii)	–25	324	0.81	147	0.37	$2 \cdot 10^{-4}$	none
$\star$	–25	290	0.73	94	0.23	$1 \cdot 10^{-4}$	none

generated Dalitz pairs : 48739

measured : 19550

signal : 9551

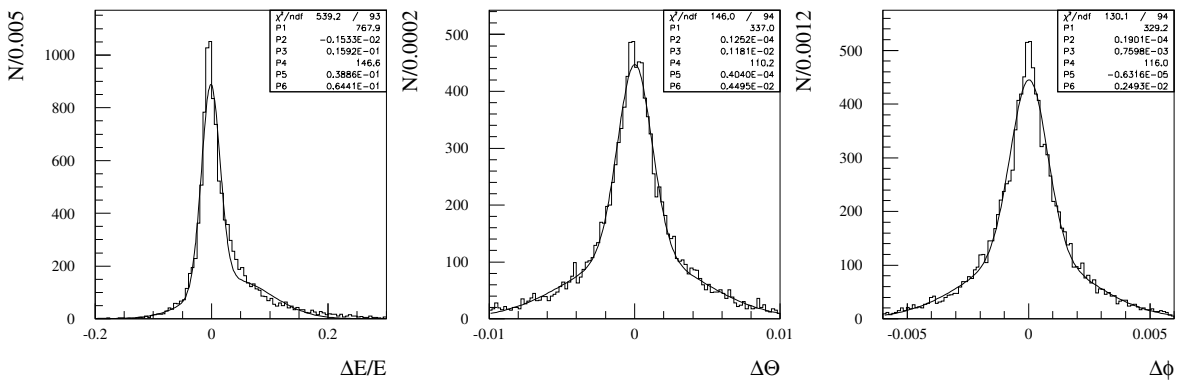

Figure 5.5: *Distributions of the values which form the χ^2 of the matching procedure. A double Gaussian is fitted to the distributions to estimate the errors.*

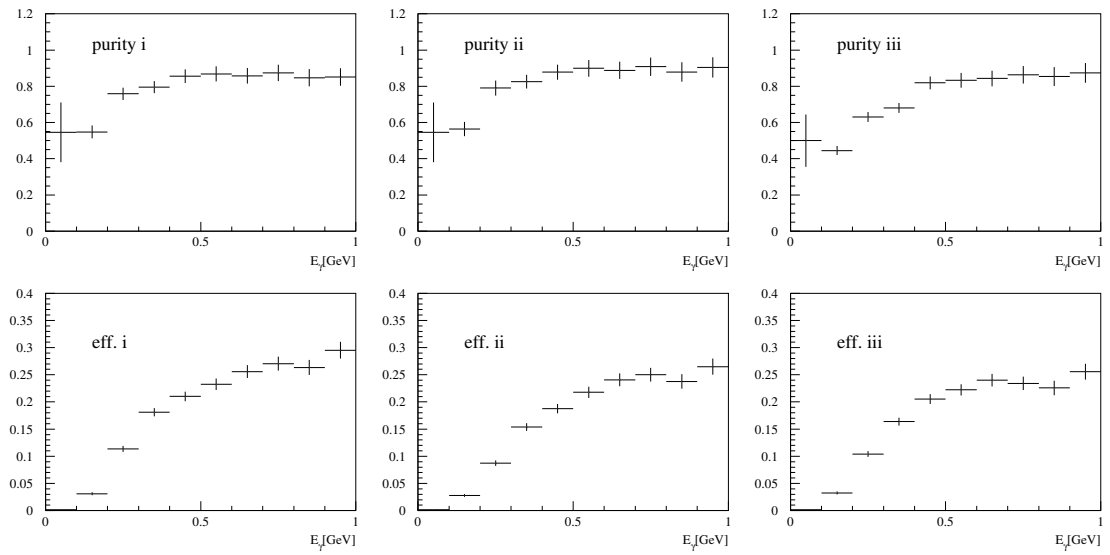

Figure 5.6: *The energy dependence of purities and efficiencies using the cuts i)-iii) is shown for Dalitz pairs below 1 GeV.*

ii) $q^2 < 2 \cdot 10^{-4}(\mathrm{GeV})^2$ and one good TPC dE/dx measured for –26 and –27 pairs, $|\cos\theta_T| < 0.7$

iii) $q^2 < \cdot 10^{-3}(\mathrm{GeV})^2$ and two good TPC dE/dx measured for –27, one good for –26 pairs, $|\cos\theta_T| < 0.7$

Additionally to the photon requirements the θ-value of the event thrust axis has to be inside the barrel region. The corresponding efficiencies and purities for photon energies below 1 GeV are shown in fig.5.6. The three efficiencies differ only a little in shape.

All cuts allow the same amount of background suppression and show a similar energy dependence. For the total efficiencies one gets (incl. statistical errors): Background of

cut	ϵ_{γ^*}	P_{γ^*}
(i)	0.150 ± 0.016	0.740 ± 0.010
(ii)	0.125 ± 0.015	0.831 ± 0.011
(iii)	0.121 ± 0.015	0.747 ± 0.012

real photons converted at the beam pipe is heavily suppressed, by the hard requirements on the impact parameter an the primary vertex fit. Especially low energy converted photons will fail these requirements. Only a fraction of 0.6% was found after the cuts (iii) and a fraction of 1.17 % in the whole sample of Dalitz pairs. For a specific analysis apart from the π^0 decay the efficiency has to be calculated by integrating the expected photon spectrum multiplied with the efficiency curves described above.

The π^0 Dalitz Decay

To test this method for collecting internally converted photons, the π^0 Dalitz decay is used as a cross check. To observe this decay the Dalitz pair is combined with a conventional photon. Since the main interest for the later analysis is in the low energy range, the other photon is taken to be a converted photon from the detector material. These have their highest detection efficiency in the low energy range as shown in [53]. Furthermore their energy resolution is much better than that of low energy calorimeter (HPC) photons. For a Dalitz decay both photons should come from the primary vertex and their invariant mass is computed. In fig.5.7, a π^0 signal obtained by combining converted photons with Dalitz pairs selected with the cuts (iii) are shown.

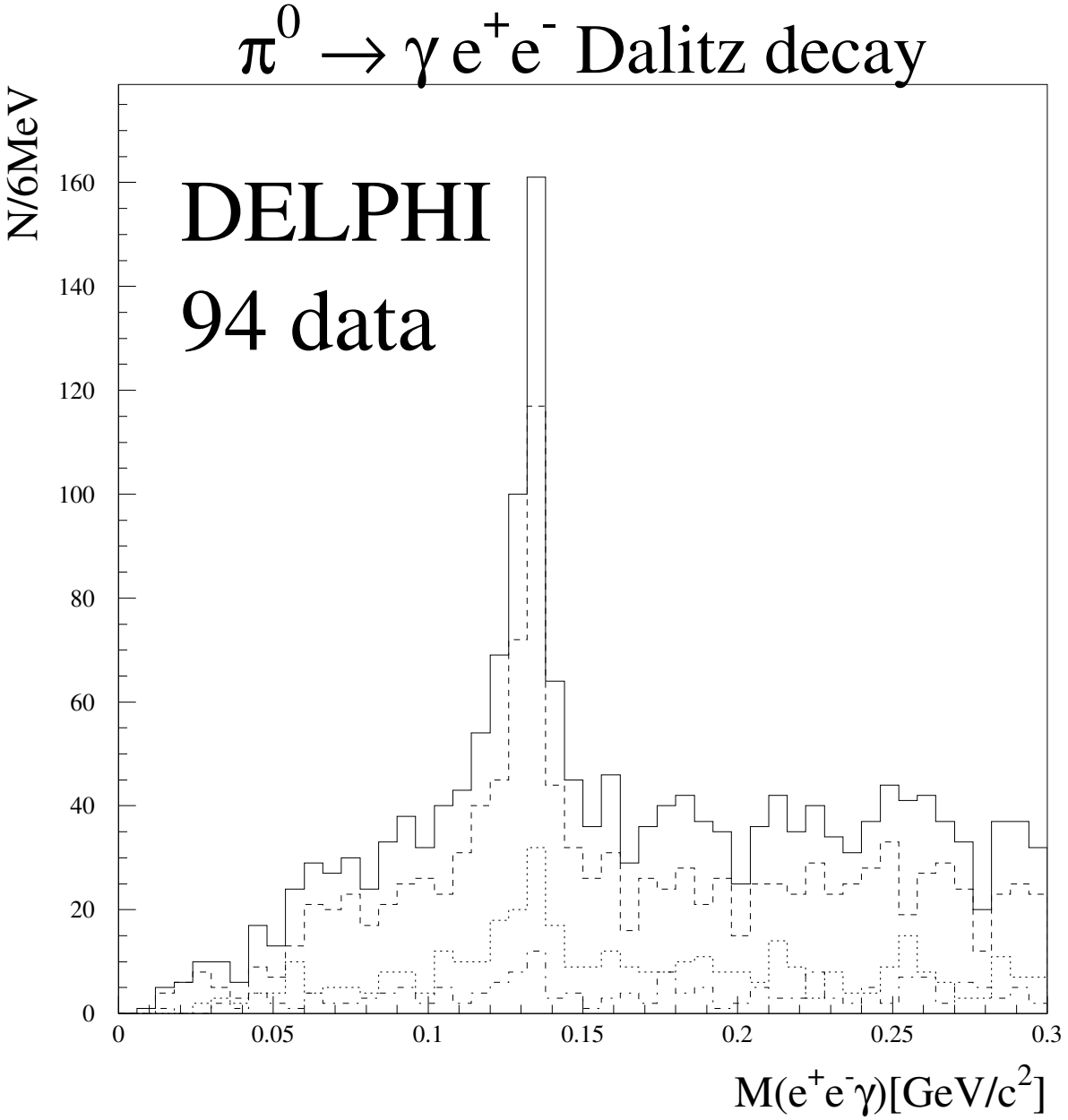

Figure 5.7: *Observation of π^0 Dalitz decay: The invariant mass of one converted photon and one Dalitz photon is shown. The solid line contains all classes of photons, the broken line represents the type –27, the dotted line the type –26, the broken dotted line type –25.*

5.2 Inclusive Reconstruction of B Mesons

To analyse the decays of B mesons the first aim is to enrich the sample of $q\overline{q}$-events with $b\overline{b}$ events. The next step is the inclusive reconstruction of the B meson four momentum and last to correct for missing particles.

5.2.1 b-Quark Tagging

The standard method of impact parameter tagging is used to distinguish b-events from udsc-events (a detailed description is given in [54]). Here only tracks with at least two vertex detector hits are used, since this method requires a fine resolution near the primary vertex. Because the B mesons are expected to decay after some flight distance their decay particles should give a B-vertex off the **primary vertex** where primary particles are assumed to come from. In order to be able to qualify tracks in this manner a clear determination of the primary vertex is needed. For its reconstruction the position of the beam spot is used, which is redefined every 200 hadronic events and is formed by taking all tracks with at least two vertex detector hits. To avoid a wrong biased determination of the primary vertex from badly measured tracks their confidence coefficient, computed by the distance to the beamspot and the corresponding error, should be greater than 5%. Also for the associated hits of the tracks a quality cut depending on the vertex detector resolution and the hit-track distance is applied. An initial vertex is reconstructed. Then on track is excluded if the reduction in χ^2 is maximised. The track is left and the primary vertex is computed without this track. By repeating this procedure and requiring a minimal $\Delta\chi^2$ a group of tracks is excluded and tracks most probably coming from the primary vertex are left.

The **impact parameter** in the R-Φ-plane is defined as the distance from the perigee point $\vec{P}$, the point of closest approach, to the primary vertex $\vec{V}$. A simple drawing in fig.5.8 illustrates the definition of positive and negative impact parameters. The sign of the impact parameter d_a is defined from the jet direction. If the vector from the primary vertex $\vec{V}$ to the perigee $\vec{P}_a$ points in the same direction as the jet, the sign is positive, if the direction $\vec{V} \rightarrow \vec{P}_a$ is opposite to the jet direction the sign is negative (see fig. 5.8). Apart from the value of the impact parameter of a specific track a the error of this parameter is needed. It depends on the errors of the perigee point, the error of the primary vertex and the size of the beam spot. The **significance** is defined as the ratio of the impact parameter value to its error:

$$S_a = \frac{d_a}{\sigma(d_a)} \ . \tag{5.4}$$

The distribution of the significance, see fig. 5.9, should be of Gaussian form, when all tracks come from the primary vertex, except for particles with long lifetimes which cause an excess for high values of S. The resolution can be studied for the distribution of negative significances where no long living particles are expected. In reality to the

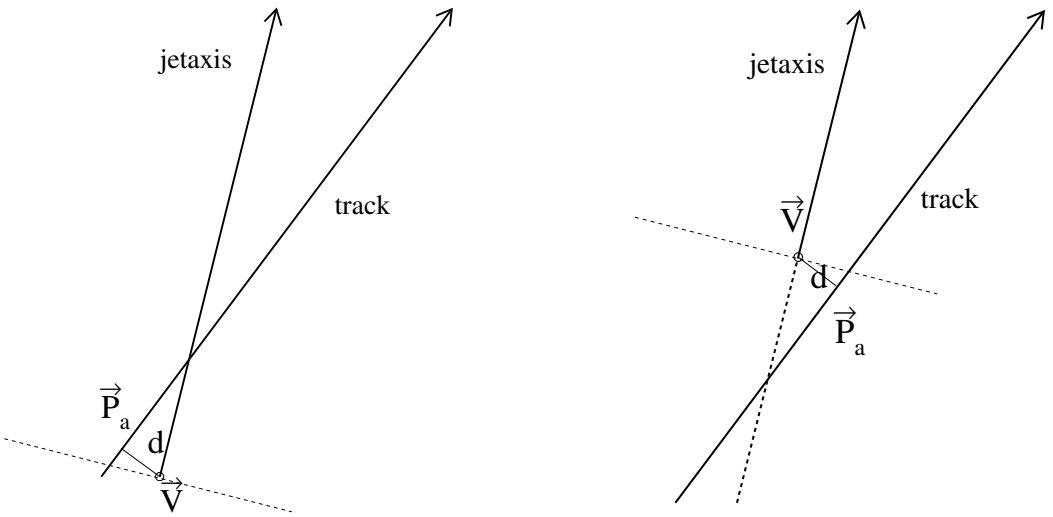

Figure 5.8: *The impact parameter 'd' is shown for the positive and negative case. It stands for the the smallest distance 'd' of the primary vertex perpendicular to the track direction. The direction of 'd' compared with the jet direction of the hemisphere gives the sign of the impact parameter. The broken thin line indicates the two hemispheres.*

resolution includes a non–Gaussian shape, which comes from wrongly reconstructed tracks. Assuming the negative significance distribution to be symmetric for the case of primary vertex tracks, the **probability** for a measured significance S_0 can be derived:

$$P(S_0) = \begin{cases} \int\limits_{S<S_0} f(S)dS & \text{if } S_0 < 0 \\ P(-S_0) & \text{if } S_0 > 0 \ . \end{cases} \tag{5.5}$$

The assumed probability density function $f(S)$ of the significance distribution is also called the resolution function. For any group of N tracks the N-track probability is defined as:

$$P_N \equiv \Pi \sum_{j=0}^{N-1} (-\ln \Pi)^j / j! \quad \text{with } \Pi \equiv \prod_{i=1}^{N} P(S_i) \ . \tag{5.6}$$

This gives the probability for a group of N tracks to satisfy the primary vertex hypothesis. Thus the resulting distribution for this probability should be flat for light quark events and for heavy quarks an excess at small values is expected. Since the group (N) can be a sample of selected tracks up to all tracks of the event, this parameter can be interpreted as a track, hemisphere or event probability depending on the selected sample of tracks. The probability distributions for u-d-s, c and b flavours are shown in fig.5.10. Requiring now very small probabilities for the whole event gives an enrichment of $b\bar{b}$-events in the selected sample. Table 5.2 shows the resulting efficiency and probability of b-quark tagging with the impact parameter method in DELPHI.

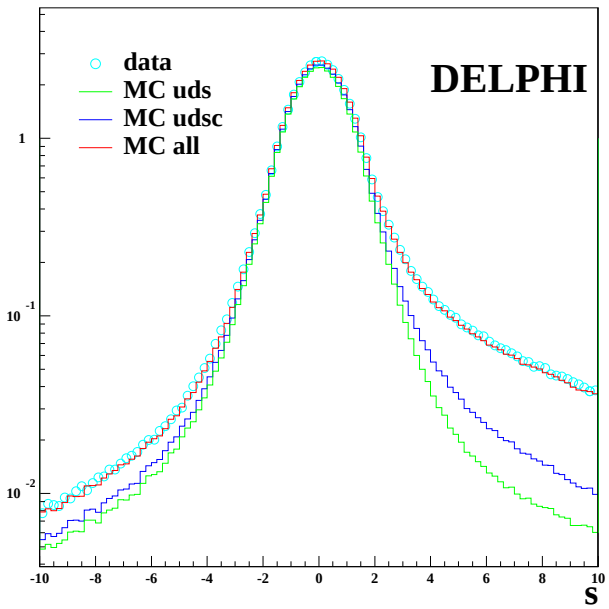

Figure 5.9: *Track significances shown for all types of events. The distribution has a tail for positive values of S coming from long living particles in c- and b-quark events. The negative distribution serves for the probability definition.*

Table 5.2: *B-tagging efficiency for several cuts on the event probability together with the charm efficiency and the b purity. All numbers correspond to the 94C processing. For b analysis the 'standard cut' is* $P_H^+ < 0.01$.

$log10(P_H^+) <$	ϵ_c	ϵ_b	b purity
-1.0	0.438	0.848	0.545
-1.5	0.301	0.779	0.666
-2.0	0.213	0.720	0.753
-2.5	0.154	0.670	0.812
-3.0	0.114	0.621	0.851
-3.5	0.083	0.580	0.885
-4.0	0.062	0.536	0.910

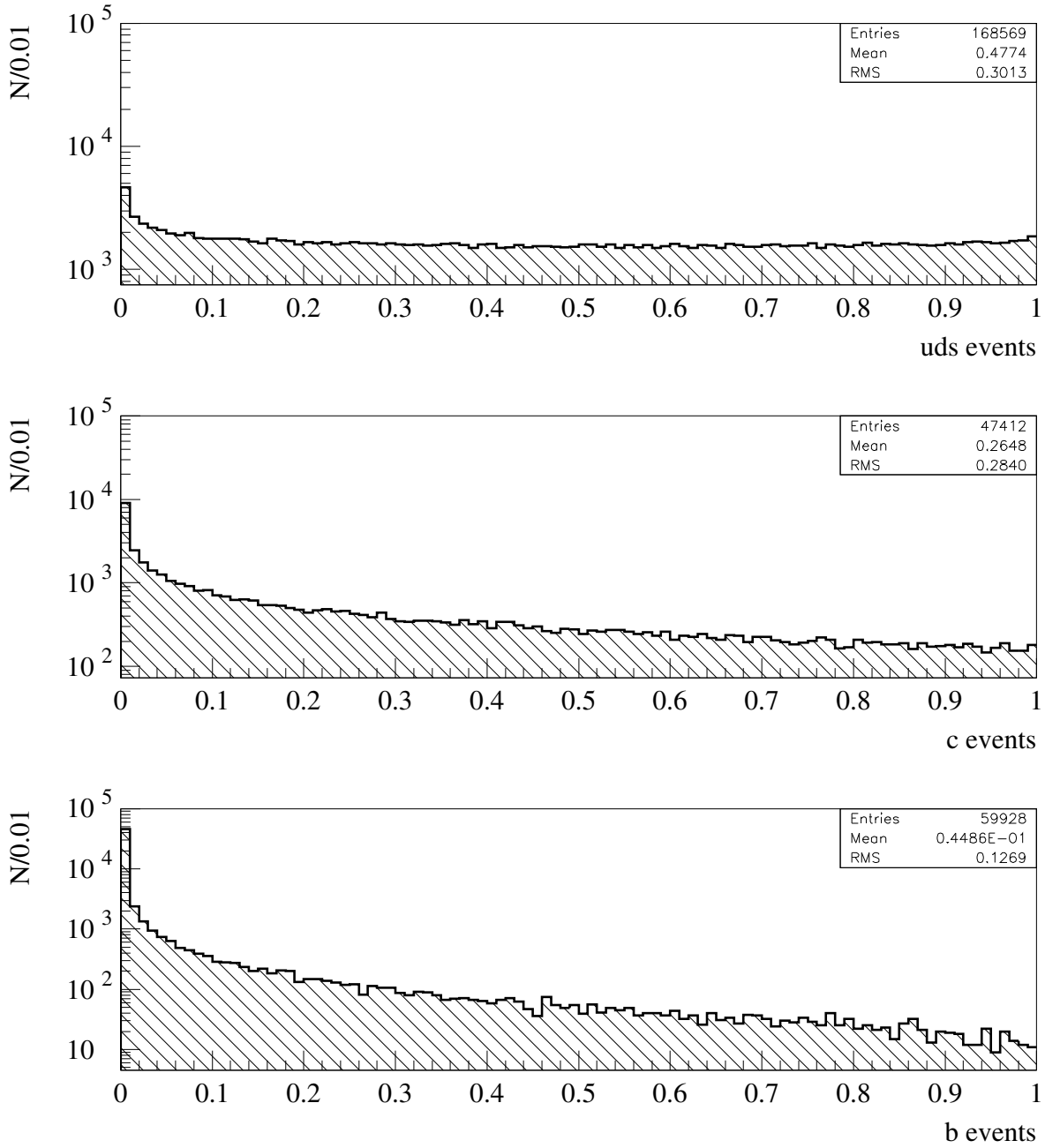

Figure 5.10: *Event probabilities for tracks with positive impact parameters, divided in light, c- and b-quark events. For light quarks the distribution is nearly flat with a small excess coming from K^0 and Λ decays at low probabilities. The hypothesis is not satisfied for heavy flavours, giving an excess of small probability values.*

5.2.2 Rapidity Algorithm

Inclusive reconstruction means the non–identification of all final state B decay products. All possible decay channels are collected. No charge information about the B^* or B meson is available. Due to the small exclusive branching ratios and small identification efficiency an exclusive analysis would suffer from small statistics. The following algorithm has been developed and successfully applied in the DELPHI $B^* \to B\gamma$ analysis [25]. To collect the decay products the rapidity:

$$y = \frac{1}{2} \log \frac{E + p_z}{E - p_z} \tag{5.7}$$

of charged and neutral particles is used, allowing one to separate the B products from particles coming from fragmentation. In this formula E is the energy of the particle and p_z is the momentum along the thrust axis. This method works due to the hard fragmentation function of B mesons, and their large mass. Simulation studies show that the rapidity of B mesons along the event axis is strongly peaked at $y = \pm 2.4$, with some spread towards lower $|y|$ due to hard gluon radiation (see fig.5.11). B meson decay products have a Gaussian distribution in rapidity space with a width of about 0.8 units. In b-events the fragmentation process mainly generates particles at lower rapidities, and their distribution can be described by two Gaussians of width 1.05 units, with a mean of ± 1.03. The model dependence of these distributions has been analysed by comparing the prediction of JETSET 7.4 [15] and HERWIG 5.8[55] (with JETSET decays), both with default parameters. In general these two predictions differ by less than 10% at any y in the inclusive y distribution from fragmentation, and by less than 4% in the distribution from B decays. Detector acceptance and resolution effects have only a small influence on these distributions, the most important being that the loss of low energy particles leads to a suppression of the population at low $|y|$. The inclusive rapidity distributions for DELPHI data and simulation are shown in fig.5.11.

To make a vector representing the B meson the events are divided into two hemispheres defined on the thrust axis, see fig. 5.12. The rapidity of each reconstructed charged particle with respect to the thrust axis is calculated. Particles outside a central rapidity window of ± 1.5 units are considered to be B meson decay products. The four-momenta of these particles are added together in each hemisphere, leading to an energy measurement E_y for the B meson on each side of the event. From the nature of this reconstruction there are events not well reconstructed, most of these can be removed by requiring:

1. a minimum energy of $E_y > 20$ GeV for the B meson reconstructed from rapidity
2. the reconstructed mass within the range of ± 2.5 GeV/c^2 of the rapidity B meson
3. the fraction of hemisphere energy to beam energy $x_h = E_{hem}/E_{beam}$ in a reasonable range of $0.6 < x_h < 1.1$

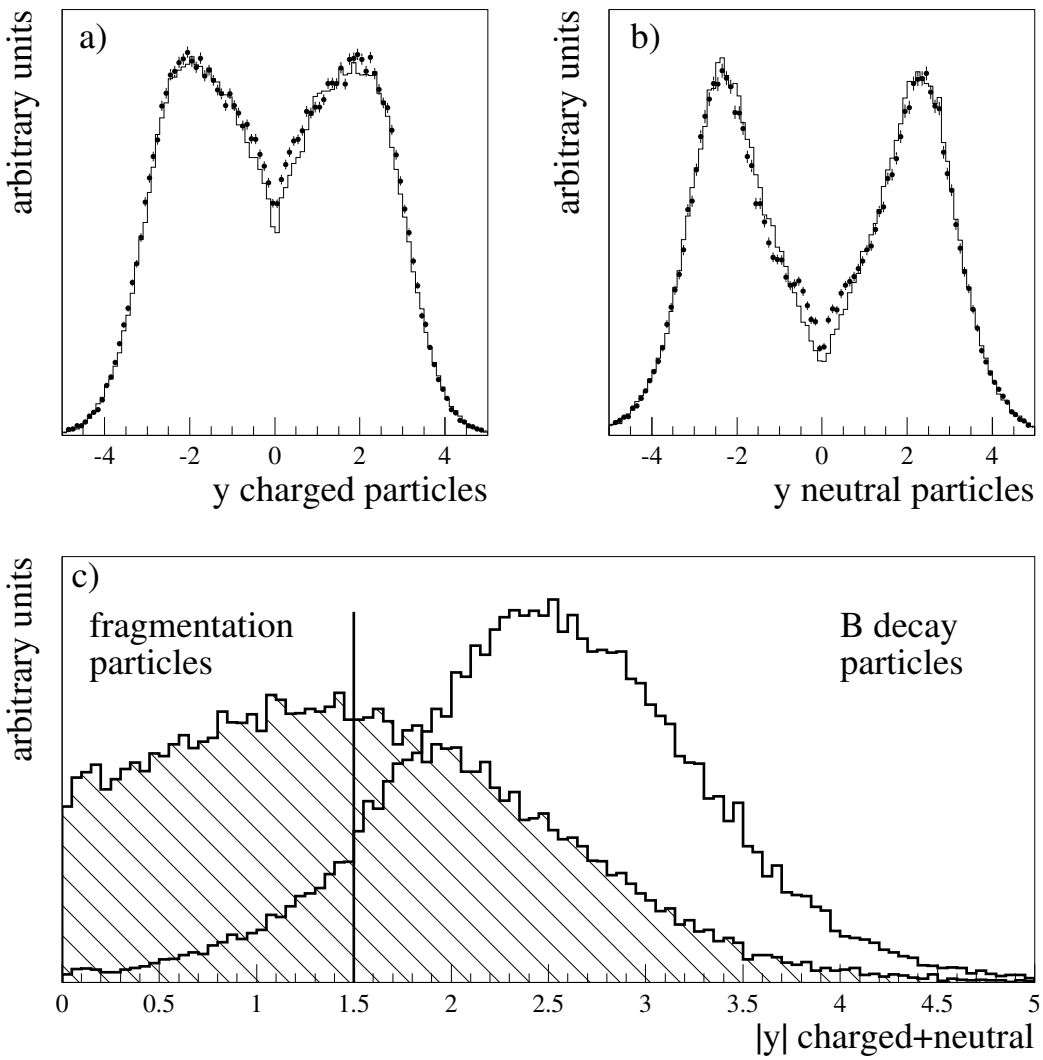

Figure 5.11: *The upper part shows the rapidity distribution for charged a) and neutral b) particles. The histogram represents the simulation distribution, the dots with error bars the data. Both samples are taken with a standard btag of* ($P_H^+ < 0.01$) *from the 94B3* DELPHI *data and simulation. In part c) the hatched histogram shows the fragmentation and the empty histogram the B particles in* $b\overline{b}$ *events, the line indicates the used cut.*

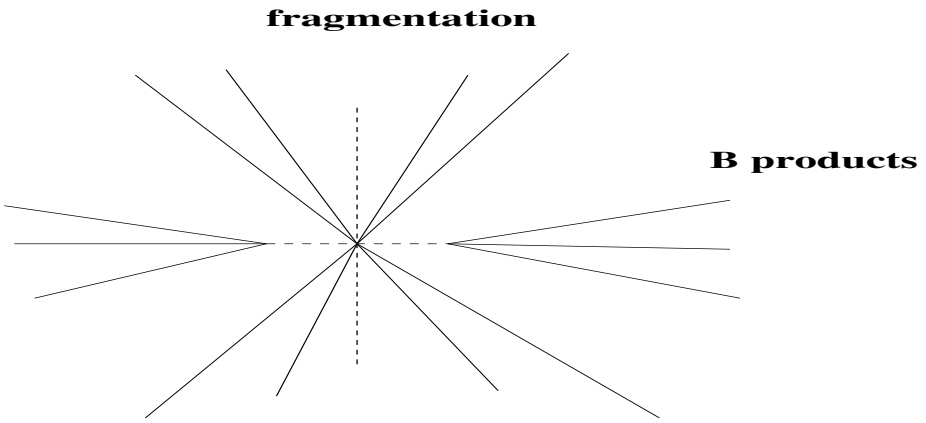

Figure 5.12: *The event is divided by the thrust axis into two hemispheres. On both sides the B decay and fragmentation particles are shown.*

Enforcing these requirement results in a loss of 26% of B decays. Applying this method yields a B meson energy and a reconstructed mass m_y distribution, which are shown in the next chapter.

5.2.3 Energy Correction of the B Mesons

For two reasons the reconstructed energy is generally less than the expected. First the rapidity algorithm loses some B decay particles from the cut on $|y|$, and the second reason are the losses of particles in the detector. The mass of the reconstructed B meson (m_y) is useful to control the first effect and the energy reconstructed in the whole hemisphere is an indicator for the quality of the total hemisphere reconstruction. By applying this method hemisphere by hemisphere, it is possible to use events which contain one bad hemisphere, where particles are lost, e.g. in detector cracks. A correction function is determined using simulated events. After applying all cuts, the simulated data are divided into several samples according to the measured ratio $x_h = E_{hem}/E_{beam}$. For each of these classes the energy loss $\Delta E = E_y - E_{Btrue}$ is plotted as a function of the reconstructed mass m_y. The median values of ΔE in each bin of m_y are calculated, and their m_y dependence is fitted by a second order polynomial:

$$\Delta E(m_y; x_h) = a + b \cdot (m_y - \langle m_y \rangle) + c \cdot (m_y - \langle m_y \rangle)^2 \ , \tag{5.8}$$

with $\langle m_y \rangle$ the expected reconstructed mass for the rapidity B meson from simulation studies. The three coefficients a, b and c for this fit in each x_h slice are plotted as function of x_h and their dependence is fitted using second order polynomials:

$$a(x_h) \ = \ a_1 + a_2 x_h + a_3 x_h^2 \tag{5.9}$$

$$b(x_h) = b_1 + b_2 x_h + b_3 x_h^2$$
$$c(x_h) = c_1 + c_2 x_h + c_3 x_h^2$$

giving nine parameters to be determined. This procedure gives a smooth correction function describing the dependence on m_y and the hemisphere energy. Finally, a small bias correction is applied for the mean remaining energy difference as a function of the corrected energy:

$$E_{corr} = (1 + f_b) E_y \ , \tag{5.10}$$

determined from the simulation, which lies within a few percent. The precision of this inclusive technique depends on the cuts on the b-tagging probability, event shape variables (e.g. thrust, number of jets) and B quality cuts. For the standard cuts (section 5.2.2) the energy precision is 7% for 75% of the B mesons, the remainder constituting a non Gaussian tail towards higher energies. The angular resolution of Θ and Φ are shown in fig. 5.14. Fitting the distribution with a double Gaussian function yields in a resolution of 20 mrad for the major part and 60 mrad for the minor part.

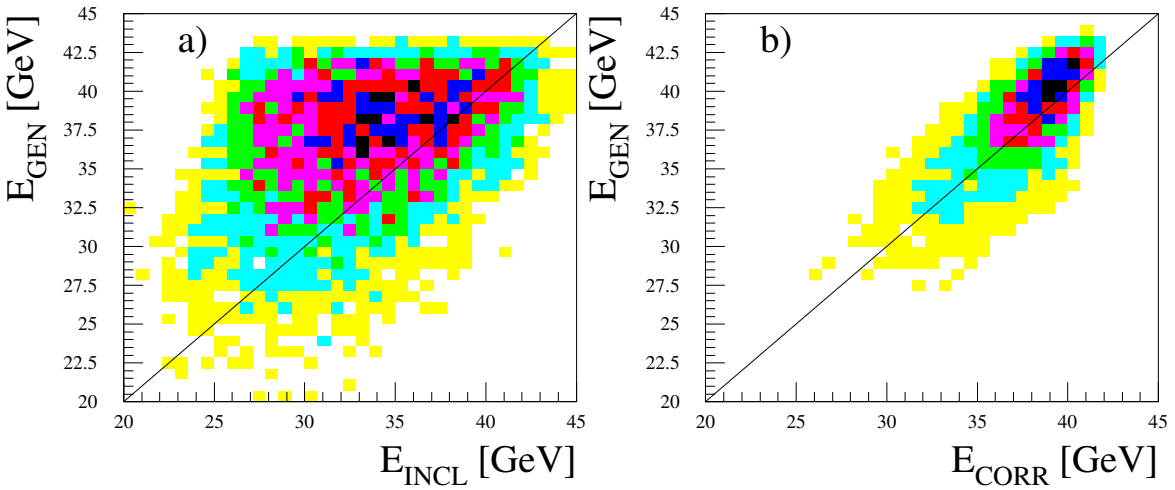

Figure 5.13: *Part a) : the true energy of the B meson versus the energy of inclusive reconstruction. Part b) : true energy of the B meson versus the energy after the correction procedure. Both distributions have been done with a 94B2 simulation sample.*

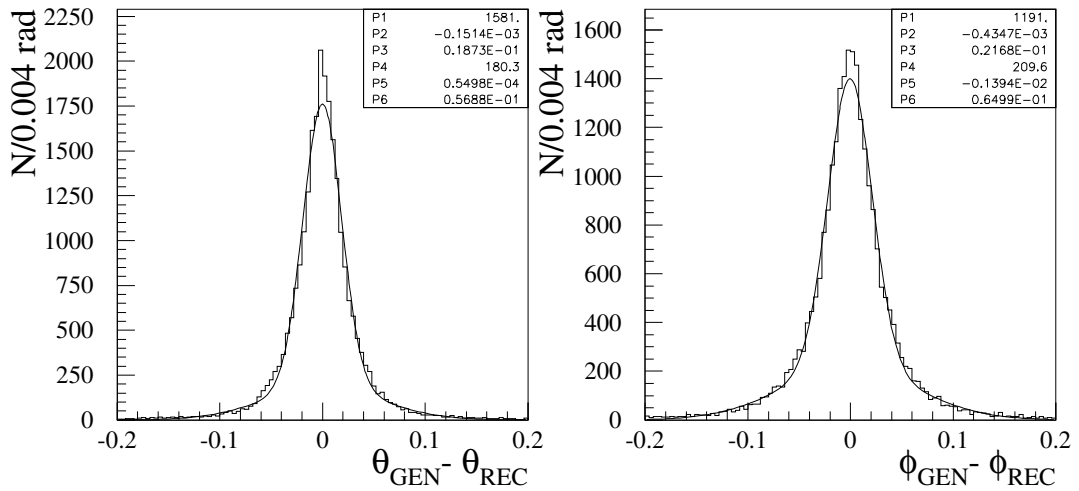

Figure 5.14: *The angular resolution of the azimuth and polar angle. The major part comes out with a resolution of about 20 mrad.*

6

Analysis of the Decay $B^* \to Be^+e^-$

Using the Dalitz photon reconstruction as introduced in section 5.1 the electron positron from the internal conversion can be seen. This photon will be added to an inclusively reconstructed B meson. From the mass difference of M(B e^+e^-)-M(B) the excited B meson can be seen decaying at the primary vertex. Simulation samples of the B^* Dalitz decay and simulated background events are used to determine the cross section of the B^* Dalitz production from the measured mass difference distribution.

6.1 Event and Track Selection

Multihadronic events were selected for the 94C2 data, see [56] for further details. Asking for tracks with:

- track length$>$ 50 cm
- $\epsilon_{xy} < 5$ cm
- $Z_P < 10$ cm
- $25° < \theta < 155°$,

the number of charged tracks is required to be larger than five and the reconstructed charged energy to be larger than 12 GeV. These cuts reduce the background of $\tau^+\tau^-$ events to 0.25% and other background sources to 0.1%. Any backgrounds from beam gas, beam wall and cosmics are heavily suppressed. Using these requirements 1.400k events are left for the 94C2 Short DST processing.

The track selection applies different cuts on the tracks used in the analysis. The tracks must fulfil:

- $\epsilon_{xy} < 4$ cm

- $Z_P < 6$ cm
- $\cos\theta < 0.94$
- $\Delta E/E < 1$

The cuts guarantee the tracks to be inside sensitive tracking regions, to come from the interaction region and not be background from cosmic events, beam gas or beam wall events. The track length and momentum is not restricted to allow the reconstruction of low momentum particles necessary for the Dalitz pair reconstruction.

6.2 B* Reconstruction

The rapidity algorithm (see section 5.2.2) is applied with the cuts:
$0.6 < x_h < 1.1$, $E_y > 20$GeV, $|4.8 - m_y| < 2.5$; for the 94C1 data. The thrust axis of the event is required in the barrel region; $|\cos\Theta_{Thrust}| < 0.7$. This achieves a nearly complete vertex detector coverage of the event necessary for the b quark tagging. The event probability of the b quark tagging is required to be $P_E^{\pm} < 0.05$. After these requirements a sample of 1385 hemispheres is left, giving good inclusive B meson four momenta and at least one Dalitz pair in the event. The energy distribution of the inclusively reconstructed B meson from the rapidity method and at least one Dalitz pair in the hemisphere is illustrated in fig. 6.1. These B meson four momenta are combined with the Dalitz pair requiring the cuts (iii) (see table 5.1), i.e.: two good

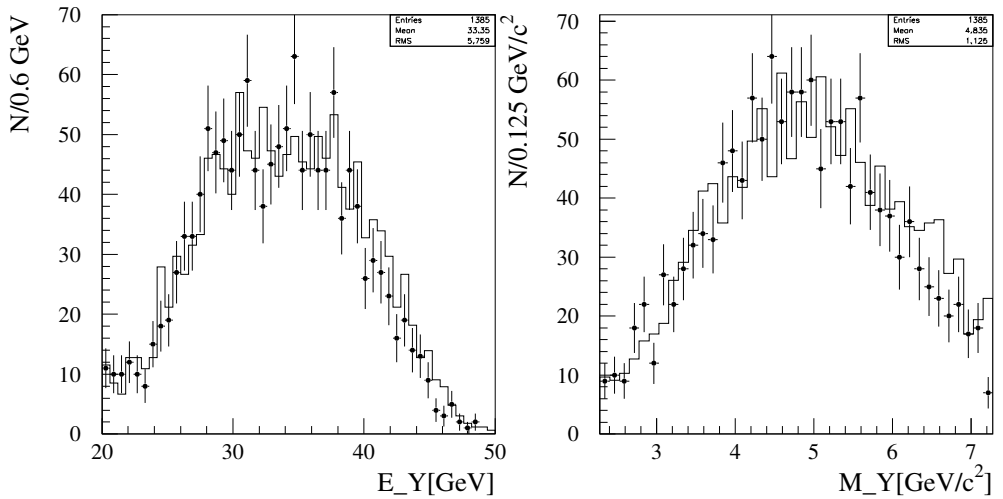

Figure 6.1: *The measured distributions of inclusive B meson a) energy and b) mass with one Dalitz pair after the cuts (iii). Solid histogram shows the simulation events and the dots with error bars the distribution for the data. The simulation distribution was normalised to the selected number of data events.*

TPC dE/dx measurements for class 27, one good TPC dE/dx measurement for class 26 and $q^2 < 10^{-3}(\mathrm{GeV})^2$ for all classes. The mass difference $\Delta M = M(\mathrm{B}e^+e^-) - M(\mathrm{B})$ on the sample of selected hemispheres after the energy correction of the inclusive B meson is shown in fig. 6.2. The mass difference distribution shows a peak near the expected Q value of 46 MeV.

The mass difference is made from the variables:

$$\Delta M(\mathrm{B}^* - \mathrm{B}) = E_\gamma \gamma (1 - \beta \cos\Theta),$$

where E_γ is the photon energy in the laboratory frame, $\gamma = E_\gamma / E_B$, the B meson Lorentz boost, $\beta = \sqrt{1 - 1/\gamma^2}$ and Θ the angle between the B meson and the B^* photon. From these variables the B meson's angular resolution of 20 mrad dominates the mass difference resolution.

6.3 Signal Determination

To determine the amount of signal entries a simulation sample processed with the same reconstruction software as the 94C data sample and without the Dalitz decay of the B^* meson was used. The sample of 2.3 M $q\overline{q}$ simulated events leads to a mass difference distribution containing 1888 entries, still suffering from fluctuations. The mass difference distribution was found to be smooth in the mass region of interest, i.e.: (0.02–0.07) GeV/c^2. This mass distribution can be described with a third order polynomial (P3):

$$P(x) = a_0 + a_1 x + a_2 x^2 + a_3 x^3 \tag{6.1}$$

or the function:

$$B(x) = a_1[(x - 0.01)(a_4 - x)]^{a_2} \exp[-a_3(x - \frac{1}{2}(0.01 + a_4))] \ . \tag{6.2}$$

Both fits come out with a similar χ^2 value. Sources of background are wrongly reconstructed Dalitz pairs coming from combinations of other charged tracks. As can be seen in fig. 5.6 on page 75 the sample of Dalitz pairs is rather pure in the energy range below 1 GeV. Another source of background are π^0 Dalitz decays, which happen in $b\overline{b}$ events and fall into the ΔM region of interest. This contribution should lead to the same amount of background as in the B^* analysis of the usual decay $B^* \to B\gamma$, where the photons have been reconstructed after conversions in the detector material [25]. Two photons per one π^0 can make a conversion, while the rate for the π^0 Dalitz decay is twice the expected B^* Dalitz decay rate. (See equations (2.38) and (2.45) page 23 ff.) From the electromagnetic decay of the B^* and π^0 no differences in the energy distribution of the photons in simulation and data are expected.
Corrections coming from the energy distribution of the B meson are not expected since

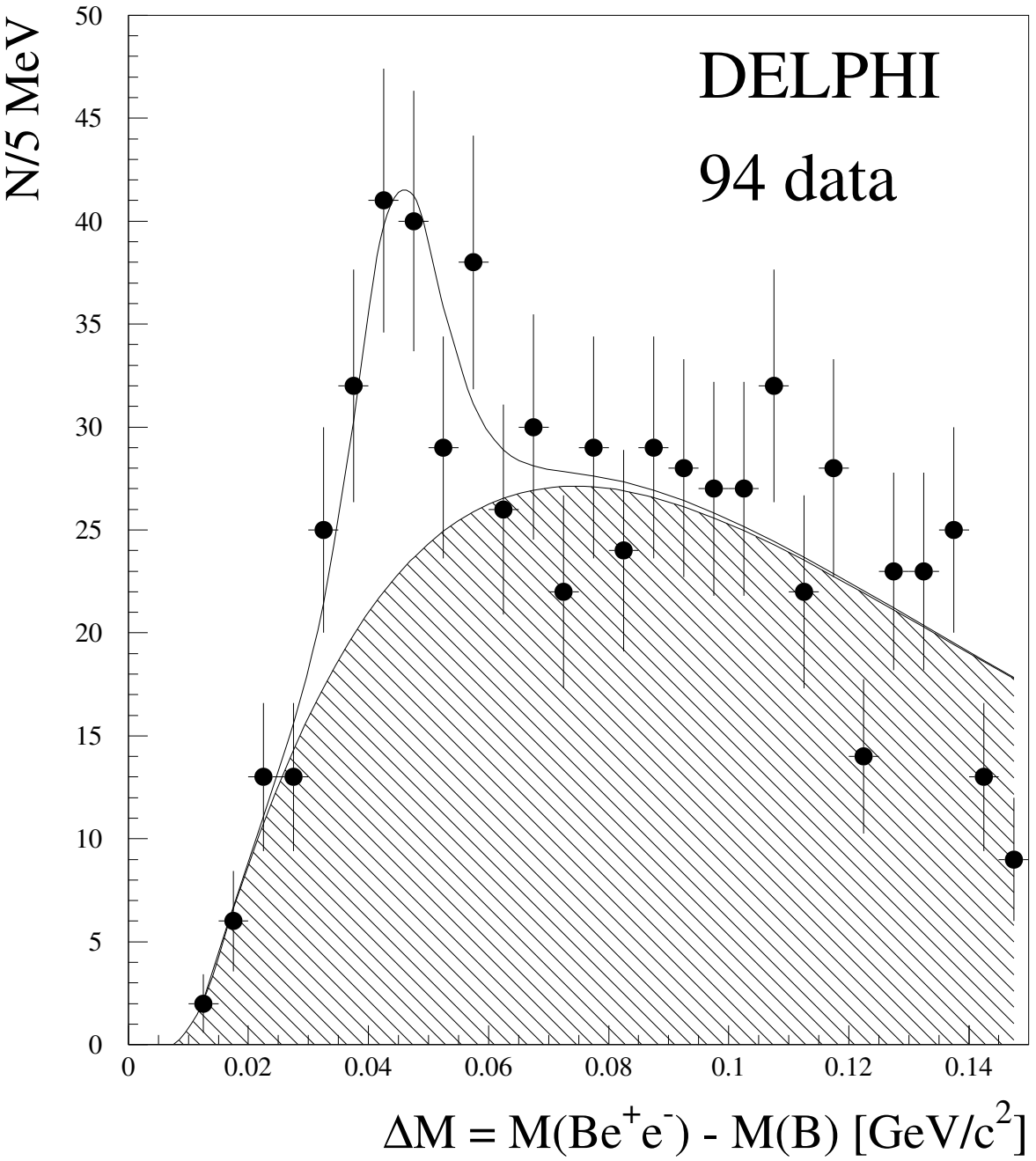

Figure 6.2: *The mass difference of B^*–B in data with a fit of the B^* simulation signal and the background shape from simulation.*

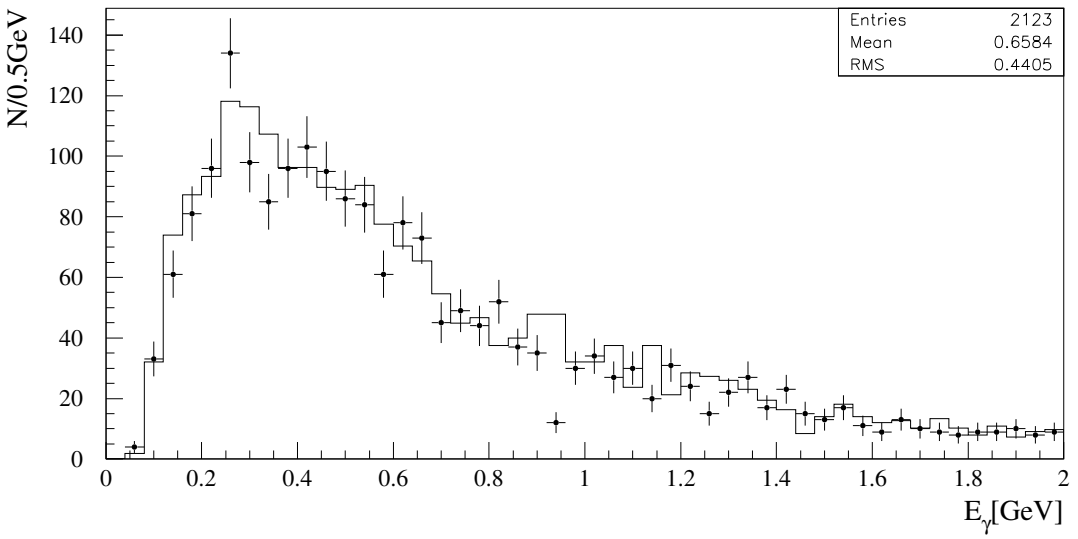

Figure 6.3: *The Dalitz pair energy spectrum, for data (dots with error bars) and simulation (solid histogram) after the cuts (iii), for events with a b-quark tagging hemisphere probability of* $\mathcal{P}^+ < 0.05$. *The simulation distribution was normalised to the number of selected data events.*

the simulation prediction of JETSET agrees well with the measured energy distribution of the B^* mesons [25].

The energy distribution of the B-meson E_y fig. 6.1 and the energy distribution of the Dalitz pairs are described well by the simulation sample as can be seen in fig. 6.3. For the signal determination the mass distributions from the fit of the formulas (6.1) and (6.2) to the background have been used. The background distribution together with a signal model were fitted to the measured mass difference distribution. The number of entries after background subtraction was taken for the signal. The signal model was varied using one Gaussian, two Gaussian and the signal shape from a simulation sample (see section 6.4). The results for the number of signal entries is shown in table 6.1. Leaving the background free from any assumption and fitting the measured distribution with the simulation signal shape and the formula (6.2) for the background results in 66 signal entries. The mean value of this series is 74. The largest difference in this series is 8. This difference of 8 entries to the mean value of table 6.1 shows the uncertainty from the low statistic in the sample. A smooth distribution with less fluctuation, would allow a more precise determination of the signal. Thus the maximum variation of 8 entries of table 6.1 is taken. The final choice for the background model from the simulation is reasonable, since the background is expected to come from the well known process of π^0 Dalitz decay.

The widths of the Gaussians shown in table 6.1 agrees with the simulation expectation, shown later.

Table 6.1: *The signal entries after background subtraction fitting the background with a polynomial and the TFIT function. For the signal model two Gaussian, one Gaussian and the simulation shape have been used. The mass region was 0.02–0.07 GeV/c^2*

signal model	formula (6.1): $P(x)$	formula (6.2): $B(x)$	means and widths [MeV]
2 Gauss	77	73	$\mu_1 = 43$, $\sigma_1 = 8$ $\mu_2 = 52$, $\sigma_2 = 12$
1 Gauss	77	73	$\mu_2 = 44$, $\sigma_2 = 11$
MC signal	79	75	
MC signal bkg free formula (6.2)		66	

6.4 Calculation of Efficiency

Taking 9194 simulated $B^* \to Be^+e^-$ decays in a sample of 7377 $b\bar{b}$ events allows a calculation of the efficiency after event selection, b-quark tagging and Dalitz pair requirements. This simulation sample was processed with the same tracking software as the data. At least 477 B^* mesons can be selected leading to the mass difference distribution in fig. 6.4. The measured mass difference distribution in the simulation was fitted with a double Gaussian, giving a resolution of 7.0 MeV/c^2 for 90% and 14.0 MeV/c for 10% of the signal remainder. The resolution is dominated by the angular resolution of the inclusive B reconstruction. The selected number of entries in the mass region of 0.02–0.07 GeV/c^2 gives a total efficiency of:

$$\epsilon = 0.0471 \pm 0.0022(\text{stat.}) \pm 0.0026(\text{syst.}). \tag{6.3}$$

The acceptance is influenced by the dE/dx determination, the choice of signal region and Dalitz efficiency. The b-quark tagging efficiency uncertainty is assumed to have a minor effect. A variation of +4% in the probability cut of the TPC dE/dx measurement shows the dependence of the exact dE/dx error computation and motivates a contribution of 0.0025. A different choice of the signal region results in an uncertainty of 0.0006 in the efficiency. Adding these contributions quadratically results in an error of 0.0026 for the total reconstruction efficiency.

The dominant influence in the efficiency is the Dalitz pair efficiency itself. The number of Dalitz pairs decreases with increasing energy while the efficiency of the Dalitz pair reconstruction increases, see fig. 5.6. A difference in the efficiency is expected as the vertex detector efficiency has to be corrected by tables, tuned with tracks higher in momentum than the Dalitz pairs. Also the average number of VD tracks in data and simulation samples is different. To check whether the efficiency is different in the simulation sample, the total number of Dalitz photons per event in the energy region less than 2 GeV in simulation and data can be taken. This approach is reasonable

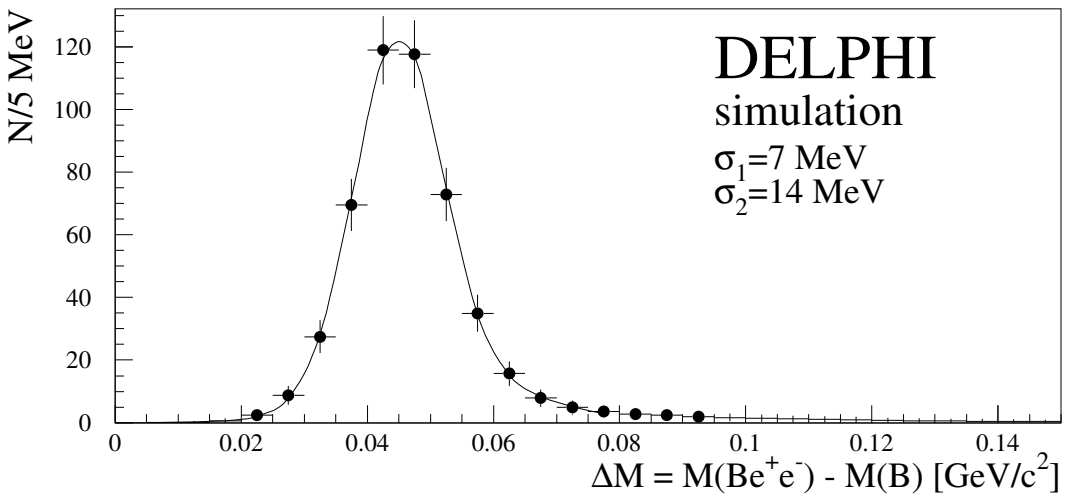

Figure 6.4: *The signal distribution of the simulation sample from 9294 $B^* \to Be^+e^-$ decays after all selection cuts. A fit with a double Gaussian gives the shown resolutions.*

since the total number of π^0, giving the main source of internal converting photons in a hadronic Z^0 decay is known better than 10%, see[53],[57]. Counting the average number of Dalitz pairs per event in data and simulation sample gives the ratio of :

$$\frac{[N(\gamma^*)/n(events)]^{data}}{[N(\gamma^*)/n(events)]^{simulation}} = \frac{0.0147}{0.0169} = \mathcal{C} = 0.871 \pm 0.087, \tag{6.4}$$

with an systematic uncertainty of 10% on this ratio. The statistical error can be neglected. When testing the number of π^0 Dalitz decays a similar correction is seen. This motivates a correction to the prior efficiency of expression (6.3):

$$\epsilon(\mathrm{B}e^+e^-) = \epsilon \cdot \mathcal{C} \ .$$

Including the uncertainty of the π^0 production this ends in the total efficiency for the B* Dalitz decay of:

$$\epsilon(\mathrm{B}e^+e^-) = 0.0410 \pm 0.0051(\mathrm{syst.}) \ . \tag{6.5}$$

The systematic error is dominated by the efficiency correction, all contributions have been added in quadrature.

6.4.1 Calculation of the Cross Section

The Observation of the B* Dalitz decay allows the measurement of the inclusive cross section, which can be calculated from the number of measured decays per b quark

hemisphere:

$$\frac{\sigma(\mathrm{B}^* \to \mathrm{B}e^+e^-)}{\sigma_{b-quark}} = \frac{N(\mathrm{B}^*)/\epsilon(\mathrm{B}e^+e^-)}{2 \cdot N(b\overline{b})/\epsilon_{b\overline{b}} \cdot P_{b\overline{b}}} \cdot \tag{6.6}$$

The impact parameter tagging using an event probability cut of $\mathcal{P}_E^+ < 0.01$ gives a sample of 276800 $\mathrm{b\overline{b}}$ events. The efficiency and purity of this selection cut are taken from the table 5.2, i.e. $\epsilon_{b\overline{b}} = 0.72$ and $P_{b\overline{b}} = 0.75$. Together with 74 signal entries and the total efficiency $\epsilon(\mathrm{B}e^+e^-)$=0.041 one gets:

$$\frac{\sigma(\mathrm{B}^* \to \mathrm{B}e^+e^-)}{\sigma_{b-quark}} = (3.21 \pm 0.62(\mathrm{stat.})) \times 10^{-3} \ , \tag{6.7}$$

for the inclusive cross section.

The ratio of the decay widths as predicted in chapter 1 can be evaluated by dividing this result with the production cross section of the usual B^* decay in b-quark events, as given in table 2.6 (LEP average) $\sigma(\mathrm{B}^*)/\sigma_{b-quark} = 0.67 \pm 0.03$,

$$\frac{\Gamma(\mathrm{B}^* \to \mathrm{B}e^+e^-)}{\Gamma(\mathrm{B}^* \to \mathrm{B}\gamma)} = (4.79 \pm 0.95(\mathrm{stat.}) \pm 0.21(\mathrm{B}\gamma\text{-rate})) \times 10^{-3} \ . \tag{6.8}$$

Systematic Uncertainties

The systematic influences on the measured cross section (see eq.(6.7)) are expected to come mostly from the efficiency calculation and the signal determination. The sources for these uncertainties have been discussed above. Other sources are the b-quark tagging purity and efficiency errors, taken from [54]. Additionally the cuts on $|\cos\Theta_{Thrust}|$, the B meson energy E_y, and the rapidity mass $|4.8 - m_y|$ and the b-quark tagging probability have been varied in a reasonable range. The variation was found to be below 6% of the final result. The contributions to the uncertainty are listed below: For the total efficiency $\epsilon(\mathrm{B}e^+e^-)$ statistical and systematic errors have been added in quadrature. The relative uncertainty on the number of signal entries is expected to be reduced when a smooth mass difference distribution with enough statistics in data and simulation is available.

Adding up all these contribution in quadrature gives the total systematic error on the production cross section : 0.59×10^{-3} of $\mathrm{B}^* \to \mathrm{B}e^+e^-$ in b-quark events.

6.5 Results

Using the 1994 data collected with the DELPHI detector at LEP, a sample of 1.4 million multi–hadronic events was collected. With the impact parameter tagging and the inclu-

Table 6.2: *The systematic contribution to the relative cross section.*

variable	value ± error	error in cross section $\sigma(Be^+e^-)/\sigma(b-quarks)$
$\epsilon(Be^+e^-)$	0.0410 ± 0.0051	0.394×10^{-3}
N_{B^*}	74 ± 8	0.347×10^{-3}
$\epsilon_{b\bar{b}}$	0.72 ± 0.03	0.132×10^{-3}
$P_{b\bar{b}}$	0.75 ± 0.04	0.169×10^{-3}
cuts		0.156×10^{-3}
total		0.588×10^{-3}

sive B meson reconstruction shown in chapter 5 four vectors of B mesons can be reconstructed. The combination of these B mesons with the Dalitz pairs explained in the previous chapter show a peak in the mass difference distribution $\Delta M = M(Be^+e^-) - M(B)$. Using simulation samples for signal and background shape, 74 signal entries can be extracted and the total efficiency to reconstruct B^* Dalitz decays is computed to be 4%. The background from simulation is found to be smooth and agrees well with the data. Taking the uncertainties from table 6.2 into account and adding the contributions in quadrature one gets for the inclusive cross section:

$$\frac{\sigma(B^* \to Be^+e^-)}{\sigma_{b-quark}} = (3.21 \pm 0.62(\text{stat.}) \pm 0.59(\text{syst.})) \times 10^{-3} \ . \tag{6.9}$$

This corresponds to a decay width ratio of:

$$\frac{\Gamma(B^* \to Be^+e^-)}{\Gamma(B^* \to B\gamma)} = (4.79 \pm 0.93(\text{stat.}) \pm 0.91(\text{syst.})) \times 10^{-3} \ . \tag{6.10}$$

The measured ratio agrees with the expected rate of 4.7×10^{-3} from Quantum Electrodynamics and confirms the observation of the second order M1 electromagnetic decay of the vector meson B^* into a pseudoscalar B meson.

The statistical error could be reduced with more collected data. Also the systematic error would decrease, when more statistics in data and simulation sample give a smooth mass difference distribution with less fluctuations.

The dominant contribution to the systematic error comes from the uncertainty of the Dalitz pair efficiency. The efficiency is found to be different in the simulation sample.

7

Summary

This thesis describes the first observation of the second order electromagnetic decay of the B^* meson $B^* \to Be^+e^-$, which is called B^* Dalitz decay in analogy to the decay of the π^0 meson into $\pi^0 \to e^+e^-\gamma$. The B^* meson is the hyperfine excitation of the B meson, made up of a b-quark and a light $\bar{u}$–, $\bar{d}$– or $\bar{s}$-quark in a vector ($J^P = 1^-$) state, i.e. parallel quark spins. The mass splitting is predicted from several models to be about 50 MeV. This value was confirmed by experimental observations. The small splitting allows a precise prediction of Quantum Electrodynamics for the ratio of the decay widths of $B^* \to Be^+e^-$ and the usual decay into one photon $B^* \to B\gamma$:

$$\frac{\Gamma(B^* \to Be^+e^-)}{\Gamma(B^* \to B\gamma)} = (4.7 \pm 0.013) \times 10^{-3} \quad . \tag{7.1}$$

The B^* mesons are produced from the decay of the Z^0 boson into a $b\bar{b}$ pair, followed by fragmentation into hadrons. The data samples have been collected with the DELPHI experiment at the LEP collider in the year 1994. They contain about 1.4 million hadronic Z^0 decays. From the mentioned splitting a small average energy of the electron positron pair of about 170 MeV in the lab frame is expected. Due to their curvature in the strong magnetic field, tracks of such low momentum do not reach the main tracking detectors of the DELPHI apparatus.

Using a new trackfinding algorithm for the three layer vertex detector of the DELPHI experiment, directly surrounding the beampipe, it was possible to reconstruct low momentum tracks of $30 \leq p \leq 100$ MeV/c in multi hadronic Z^0 decays. The tracks have been measured by requiring at least one hit in the innermost, middle, and outermost layer. The method yields about 0.6 additional tracks per event. From the possible z measurement in the outermost and innermost layer, it is possible to reconstruct 50% of these tracks in all dimensions. The comparison to simulated tracks shows an angular resolution of 1.4 mrad and a momentum resolution of 10%. The tracks from the high momentum region $0.1 \leq p \leq 20$ GeV/c can be used for the complete reconstruction of a multihadronic event. They allow the reconstruction of hadronic vertices, stemming

from secondary interactions with detector material and the identification of long living particles, decaying after the vertex detector.

A measurement of the specific ionization loss of tracks with associated vertex detector hits is possible from the integrated charge collected on the readout strips. For this purpose the vertex detector modules have to be calibrated and the signal height has to be corrected with the path length of the track through the silicon wafer. The resolution of the dE/dx measurement is less than 15% for more than 60% of the tracks with associated vertex detector hits.

A separation of electron and positrons in the low momentum region $p < 100\mathrm{MeV}/c$, normally not covered by measurements of the gas drift chamber, is possible with the dE/dx measurement of the vertex detector. Using this separation and the combination of opposite charged tracks coming from the primary vertex, it was possible to reconstruct internal converted photons from the π^0 Dalitz decay. The identified Dalitz photons could be checked with a simulation sample. From the applied cuts an efficiency of 12% and a purity of 74% was reached. The four momentum of B mesons is reconstructed inclusively by selecting all tracks with a high rapidity in b-tagged events. From this method the B meson is measured with an angular resolution of 20 mrad and 1.3 GeV width in the mass. The mass difference of the B meson combined with the Dalitz photon and the B meson itself, i.e. $\Delta M = M(\mathrm{B}e^+e^-) - M(\mathrm{B})$, shows a peak in the expected region of the B*–B mass splitting. From a simulation the efficiency for the reconstruction of the B* Dalitz decay is computed to be 4%.

After background subtraction a signal of 74 ± 17(stat.) B* Dalitz decays can be extracted from the 1994 data, which corresponds to an inclusive cross section of:

$$\frac{\sigma(\mathrm{B}^* \to \mathrm{B}e^+e^-)}{\sigma_{b-quark}} = (3.21 \pm 0.62(\mathrm{stat.}) \pm 0.59(\mathrm{syst.})) \times 10^{-3}. \quad (7.2)$$

The ratio of this production rate to the usual B* decay $\mathrm{B}^* \to \mathrm{B}\gamma$ results in the following ratio of the decay widths:

$$\frac{\Gamma(\mathrm{B}^* \to \mathrm{B}e^+e^-)}{\Gamma(\mathrm{B}^* \to \mathrm{B}\gamma)} = (4.79 \pm 0.93(\mathrm{stat.}) \pm 0.91(\mathrm{syst.})) \times 10^{-3}. \quad (7.3)$$

This ratio agrees with the prediction of Quantum Electrodynamics. The measurement is dominated by the statistical error, the systematic uncertainty results mainly from the efficiency determination.

Bibliography

[1] S. L. Glashow, *Nucl. Phys.* **22** *(1967) 579;*
S. Weinberg, *Phys. Rev. Lett.* **19** *(1967) 1264;*
A. Salam, *Phys. Rev.* **127** *(1962) 331.*

[2] R. H. Dalitz. *Proc. Phys. Doc.(London)* **A 64** *(1951) 667.*

[3] M. Gell-Mann and Y. Ne'eman. *'The Eightfold Way', W.A.Benjamin Inc., New York 11 (1964).*

[4] M. Gell-Mann, *Phys. Lett.* **8**, *(1964) 214;*
M. Zweig, *CERN-TH-401 (1964), CERN-TH-412 (1964), 'Development in the Quark Theory of Hadrons, A Preprint Collection', Vol 1., Ed. D. B. Lichtenberg, S. P. Rosen (Hadronic Press. Inc. Nonamten Mass. 1980).*

[5] I. Friedman, H. W. Kendall, R. E. Taylor et. al., Phys. Rev. Lett. **23** (1969) 930;
R. N. C. and G. Goldhaber, *'The experimental foundations of particle physics', p. 240-260.*

[6] W. Lucha and F. F. Schöberl. *'Die starke Wechselwirkung', BI-Wiss.-Verl.1989 Mannheim.*

[7] F. Abe et al., CDF Collaboration, *Phys. Rev. Lett.* **74** *(1995) 2626;*
S. Abachi et al., D0 Collaboration, *Phys. Rev. Lett.* **74** *(1995) 2632.*

[8] N. Isgur and M. B. Wise, *Phys. Lett.* **B 232** *(1989) 113;*
M. B. Wise, *Procs. XVI Int. Symp. on Lepton and Photon Interaction, Ithaca N.Y.1993, Ed. P. Drell, D. Rubin, p.253.*

[9] N. Isgur and M. B. Wise. *'Heavy Quark Symmetry' in Advanced series on directions in High Energy Physics Vol.10 'Heavy Flavours' World Scientific 1992, Ed. A. J. Buras, M. Lindner, p.253.*

[10] N. Isgur and M. B. Wise. *'Heavy Quark Symmetry', 'B Decays', World Scientific 1992 2nd Edition, Ed. S. Stone, p. 158.*

[11] A. F. Falk et. al. *Nucl. Phys.* **B 357** *(1991) 185.*

[12] J. H. Kühn, A. Reiter, and P. M. Zerwas. *Nucl. Phys.* **B 272** *(1986) 560.*

[13] G. Altarelli and G. Parisi. *Nucl. Phys.* **B 126** *(1977) 298.*

[14] B. Anderson, G. Gustafson, G. Ingelman, and T. Sjöstrand, *Phys. Rep.* **97** *(1983) 33;*
B. Anderson, G. Gustafson, and B. Söderberg, *Z. Phys.* **C 20** *(1983) 317.*

[15] T. Sjöstrand. *Comp. Phys. Comm.* **82** *(1994) 74.*

[16] C. Peterson, D. Schlatter, I. Schmitt, and P. M. Zerwas. *Phys. Rev.* **D 27** *(1983) 105.*

[17] Y. L. Dokshitzer, V. A. Khoze, A. H. Mueller, and S. I. Troyan, *'Basics of pertubative QCD', chap. 4, 9, Edition Frontieres (1991);*
DELPHI Coll., P. Abreu et. al., *Z. Phys.* **C 70** *(1996) 179;*
S. Bethke and J. E. Pilcher, *HD-PY 92/06 (1992), Annual Review of Nuclear and Particle Science, Vol. 42 (1992).*

[18] DELPHI Coll., P. Abreu et al., *Z. Phys.* **C 57** *(1993) 181;*
DELPHI Coll., P. Abreu et al., *Z. Phys.* **C 56** *(1992) 47;*
OPAL Coll., M. Z. Akrawy et al., *Phys. Lett.* **B 263** *(1991) 311.*

[19] DELPHI Coll., *contr. paper to EPS 1995 Bruxelles, EPS0560,* DELPHI-*Note 95-103 PHYS 538;*
ALEPH Coll., *CERN PPE/95-113 Phys. Lett.* **B 357** *(1995) 699.*

[20] Review of Particle Properties. *Phys. Rev.* **D 54** *(1996) 1.*

[21] K. Han et al CUSB Coll. *Phys. Rev. Lett.* **55** *(1985) 36.*

[22] CUSB 2 Coll., J. Lee-Franzini et al., *Phys. Rev. Lett* **65** *(1990) 2947;*
CSUB 2 Coll., Q. W. Wu et al., *Phys. Lett.* **B 273** *(1991) 177.*

[23] CLEO 2 Coll., D. S. Akerib et al., *Phys. Rev. Lett.* **67** *(1991) 1692.*

[24] L3 Coll., M. Acciarri et al., *Phys. Lett.* **B 345** *(1995) 589.*

[25] DELPHI Coll., P. Abreu et al., *Z. Phys.* **C 68** *(1995) 353.*

[26] ALEPH Coll., D. Busculic et al., *Z. Phys.* **C 69** *(1996) 393.*

[27] OPAL Coll. OPAL *physics note pn-231, contr. paper to ICHEP 1996 Warsaw pa05-037.*

[28] L3 Coll. L3 *unnumberd contr.paper to EPS 1995 Bruxelles.*

[29] J. J. Lord et al.,*Phys. Rev.* **87** *(1952) 538;*
R. A. Daniel et al., *Philos. Mag.* **43** *(1952) 753.*

[30] L. G. Landsberg. *Phys. Rep.* **128** *(1985) 301, page 336.*

[31] D. W. Joseph. *Nuovo Cimento* **16** *(1960) 997.*

[32] M. A. Schardt et al. *Phys. Rev.* **D 23** *(1981) 639.*

[33] CELLO Coll., H. J. Beherend et al., *Z. Phys.* **C 49** *(1991) 401.*

[34] K. Wille. 'Physik der Teilchenbeschleuniger und Synchrotronstrahlungsquellen' Teubner Studienbücher, Stuttgart 1996.

[35] DELPHI Coll., P. Aariano et al., *CERN-PPE/90-128, Nucl. Instr. Meth.* **A 303** *(1991) 233.*

[36] DELPHI Coll., P. Abreu et al., *CERN-PPE/95-194, Nucl. Instr. Meth.* **A 378** *(1996) 57.*

[37] DELPHI Coll., V. Chabaud et al., *CERN-PPE/95-86, Nucl. Instr. Meth.* **A 368** *(1996) 314.*

[38] K. Kleinknecht. *'Detektoren für Teilchenstrahlung' Teubner Studienbücher 1987.*

[39] W. Leo. *'Particle Detectors', Springer Verlag 1991, p. 46, 207.*

[40] F. A. Behrends, W. Hollik, and R. Kleiss. *Nucl. Phys.* **B 304** *(1988) 712.*

[41] J. E. Campagne and R. Zitoun. *Z. Phys.* **C 43** *(1989) 469.*

[42] S. Jadach et al. *Comp. Phys. Comm.* **79** *(1994) 503.*

[43] M. Feindt, W. Oberschulte gen. Beckmann, and C. Weiser. MAMMOTH Reference Manual, DELPHI note 95–52 PROG 216.

[44] M. Blume. *Ph.D. thesis Wuppertal University 1996 WUB-DIS 96-19.*

[45] P. Mattson. DELPHI *note 95-147 MVX 6.*

[46] A. Andreazza, V. Chabaud, H. Dijkstra, and P. Collins. DELPHI *note 95-177 MVX 10.*

[47] M. Blume, G. Sciolla, and M. Caccia. DELPHI *note 95-18 PROG 212.*

[48] I. Siccama. DELPHI *note 92-156 PHYS 245.*

[49] C. Weiser and M. Feindt. DELPHI *note 96-69 CONF 3, contr. paper to ICHEP 1996 Warsaw pa01-040.*

[50] K. S. Kölbig and B. Schnorr. *Comp. Phys. Comm.* **31** *(1984) 97; CERNLIB, DENLAN and DIFLAN functions, G110-1.*

[51] P. Billoir. PXFVTX, program for fitting vertices of two tracks, DSTANA library.

[52] M. Feindt, C. Kreuter, and O. Podobrin. *ELEPHANT Reference Manual,* DELPHI *note 96-82 PROG 217.*

[53] M. Wielers, *Ph.D. thesis 1995 University of Karlsruhe, IEKP-KA/95-9;*
DELPHI Coll.,W. Adam et al., *Z. Phys.* **C 69** *(1996) 561.*

[54] G. V. Borisov, DELPHI *note 94-125 PROG 208 ;*
G. V. Borisov and C. Mariotti, DELPHI *note 95-142 PHYS 567.*

[55] G. Marchesini et al. *Comp. Phys. Comm.* **67** *(1992) 465.*

[56] DELPHI Coll., P. Abreu et al., *Z. Phys.* **C 54** *(1992) 55.*

[57] ALEPH Coll., R. Barate et al., *CERN-PPE 96-168, Nov 1996.*

Acknowledgements

This thesis was worked out in the DELPHI group of the "Institut für experimentelle Kernphysik" of the University of Karlsruhe. Therefore I thank all people of the group for support and the good working atmosphere. Throughout my graduate study I was financially supported by the Land Baden Württenberg and the Graduiertenkolleg of the faculty of physics.

I would like to thank Prof. Dr. W. de Boer for the possibility to work in the field of B spectroscopy, his advise, reading the manuscript and the support for visiting meetings and conferences world wide plus the 22 months permanent stay in Geneva.

I am grateful to Prof. Dr. Th. Müller for being the "Korreferent".

Most of the thesis has been developed in the framework of the B inclusive physics team of the DELPHI collaboration. Therefore I thank Dr. Michael Feindt for continuous support, the nice atmosphere in the group and reading the manuscript. Further thanks go to Dr. Oliver Podobrin and Dr. Christof Kreuter. Dr. Andreas Seitz and Ulrich Schwickerath have been helpful concerning computer problems. Dr. Emile Schyns introduced me to the CERN enviroment. Together with Dr. Ralf Ehret and Christian Weiser it was a pleasure to work on tracking problems, resulting in the MAMMOTH project. The success of the MAMMOTH project was finally possible by the help of Dr. Tzanko Spassoff, Dr. Magnus Karlsson and Dr. Matthias Blume. Many thanks go to the vertex detector hardware group of DELPHI, namely Dr. Hans Dijkstra, Dr. Magnus Karlsson, Ken Osterbek and Dr. Agnieszka Zalewska plus many others. Dr. Pierre Antilogous has been very helpful whenever problems in the TPC dE/dx arrived. Thanks go to Dr. Jon Guy for 7377 simulation events and reading the manuscript.

It is a pleasure to thank Christian Weiser for the fruitful collaboration, sharing the office with me and reading the manuscript.

Finally I would like to thank Evelyn and my parents for the moral support during my graduate study.